Draft version February 2, 2008
Preprint typeset using LaTeX style emulateapj v. 11/12/01

arXiv:astro-ph/0310644v1 22 Oct 2003

LOW-SURFACE-BRIGHTNESS GALAXIES IN THE SLOAN DIGITAL SKY SURVEY. I. SEARCH METHOD AND TEST SAMPLE

Alexei Y. Kniazev[1,2,5], Eva K. Grebel[1], Simon A. Pustilnik[2,5], Alexander G. Pramskij[2,5],
Tamara F. Kniazeva[2], Francisco Prada[1, 3, 4], and Daniel Harbeck[1]
kniazev@mpia.de, grebel@mpia.de, sap@sao.ru, pramsky@sao.ru,
tkn@sao.ru, fprada@ing.iac.es, dharbeck@mpia.de

Draft version February 2, 2008

ABSTRACT

In this paper we present results of a pilot study to use imaging data from the Sloan Digital Sky Survey (SDSS) to search for low-surface-brightness (LSB) galaxies. For our pilot study we use a test sample of 92 galaxies from the catalog of Impey et al. (1996) distributed over 93 SDSS fields of the Early Data Release (EDR). Many galaxies from the test sample are either LSB or dwarf galaxies. To deal with the SDSS data most effectively a new photometry software was created, which is described in this paper. We present the results of the selection algorithms applied to these 93 EDR fields. Two galaxies from the Impey et al. test sample are very likely artifacts, as confirmed by follow-up imaging. With our algorithms, we were able to recover 87 of the 90 remaining test sample galaxies, implying a detection rate of ∼96.5%. The three missed galaxies fall too close to very bright stars or galaxies. In addition, 42 new galaxies with parameters similar to the test sample objects were found in these EDR fields (i.e., ∼47% additional galaxies). We present the main photometric parameters of all identified galaxies and carry out first statistical comparisons. We tested the quality of our photometry by comparing the magnitudes for our test sample galaxies and other bright galaxies with values from the literature. All these tests yielded consistent results. We briefly discuss a few unusual galaxies found in our pilot study, including an LSB galaxy with a two-component disk and ten new giant LSB galaxies.

Subject headings: galaxies: fundamental parameters — galaxies: irregular — galaxies: photometry — galaxies: spiral — galaxies: structure – methods: data analysis

1. INTRODUCTION

Low-surface-brightness (LSB) galaxies are one of the main constituents of the realm of galaxies. They are usually defined as objects with a blue central surface brightness $\mu_0(B)$ significantly fainter than the Freeman value of 21.65 mag arcsec^{-2} (Freeman 1970). However, the threshold value of $\mu_0(B)$ to classify galaxies as LSB galaxies varies in the literature from $\mu_0(B) \geq 23.0$ mag arcsec^{-2} (Impey & Bothun 1997) to $\mu_0(B) \geq 22.0$ mag arcsec^{-2} (Impey, Burkholder & Sprayberry 2001). The understanding of the important role of LSB galaxies for many issues of extragalactic research came during the last 10–15 years (see, e.g., reviews by Bothun, Impey & McGaugh 1997; Impey & Bothun 1997). There are many topics for which the knowledge of the properties of the LSB galaxy population is crucial. They include the following: a) the galaxy luminosity function, especially at its faint end, (e.g., Dalcanton 1998; Trentham & Tully 2002; Cross & Driver 2002), which in turn is related to the understanding of the primordial power spectrum of density fluctuations (e.g., Ostriker 1993); b) the spatial distribution of lower-mass galaxies, which allows us to check the predictions of cold dark matter cosmology for large-scale-structure formation (e.g., Peebles 2001); c) the physics of star formation at low gas surface densities (e.g., van Zee et al. 1997; Ferguson et al. 1998; Noguchi 2001); d) the role of interactions in galaxy evolution; and many others.

The detection of LSB galaxies is difficult owing to their intrinsically low global luminosities and their characteristic low surface brightness. Despite more than 20 years of LSB galaxy studies, their census remains incomplete. Even in the Local Group new, very faint dwarf galaxies are still being detected, including four new galaxies within 0.8 Mpc in the past four years (Armandroff, Davies & Jacoby 1998; Armandroff, Jacoby & Davies 1999; Karachentseva & Karachentsev 1998; Grebel & Guhathakurta 1999; Whiting, Hau & Irwin 1999). Several samples of LSB objects, identified with different criteria and on either photographic plates, or on CCD images, have been published during last 20 years (for a review see Impey & Bothun 1997; Dalcanton et al. 1997). They comprise hundreds of galaxies with a central blue surface brightness, (SB) $\mu_0(B)$, in the range of 22 to 26 mag arcsec^{-2}. The number of known galaxies with lower central SB drops quickly. In the range of $\mu_0(B) = 24$ to 26 mag arcsec^{-2} only about a hundred or so are currently known (e.g., Impey et al. 1996; Dalcanton et al. 1997; O'Neil, Bothun & Cornell 1997b). Very faint LSB galaxies can have large errors in their photometric parameters or may be artifacts, thus their real number is likely smaller.

Past LSB surveys were usually either large area photo-

---

[1] Max-Planck-Institut für Astronomie, Königstuhl 17, D-69117 Heidelberg, Germany
[2] Special Astrophysical Observatory, Nizhnij Arkhyz, Karachai-Circassia, 369167, Russia
[3] Centro Astronómico Hispano-Alemán, Apartado 511, E-04080 Almería, Spain
[4] Current address: Instituto de Astrofísica de Canarias, E-38200 Tenerife and The Isaac Newton Group of Telescopes, Apdo 321, E-38700 La Palma, Spain
[5] Isaac Newton Institute of Chile, SAO Branch

graphic surveys or deep CCD surveys with small area (for a nice review see Dalcanton et al. 1997). The Sloan Digital Sky Survey (SDSS; York et al. 2000) is well suited for searches for and studies of LSB galaxies due to its homogeneity, area coverage, and depth (see the SDSS Project Book[6]). The SDSS is an imaging and spectroscopic survey that will eventually cover about one quarter of the Celestial Sphere. The imaging data are collected in drift-scan mode in five bandpasses (u, g, r, i, and z; Fukugita et al. 1996) using a mosaic CCD camera (Gunn et al. 1998). The SDSS passbands were carefully chosen to provide a wide color baseline, to avoid night sky lines and atmospheric OH bands, to match passbands of photographic surveys, and to guarantee good transformability to existing extragalactic studies. The SDSS data have already been used in a number of galaxy studies, for instance in order to calculate the galaxy luminosity function (Blanton et al. 2001), to derive galaxy number counts (Yasuda et al. 2001), to measure the effect of galaxy-galaxy weak lensing (Fischer et al. 2000), to explore the depth of galaxy potential wells (e.g., McKay et al. 2002), to investigate statistical properties of bright galaxies (Shimasaku et al. 2001), and to study the color separation of galaxy types (Strateva et al. 2001).

In this paper we describe the first step of a new LSB survey which was started with data from the SDSS Early Data Release (EDR; Stoughton et al. 2002). To develop efficient methods and to understand possible limitations, in this pilot work we started with a test sample from the catalog by Impey et al. (1996), which includes among others a large fraction of LSB galaxies and luckily covers the equatorial region provided by the SDSS EDR data. In the current work we present results from a feasibility study of using the SDSS photometric database to search for LSB galaxies and to study their basic properties. Throughout the paper a Hubble constant $\mathrm{H}_0 = 75\ \mathrm{km\,s^{-1}\ Mpc^{-1}}$ is adopted. Furthermore, we investigated the possibility to use the reduced SDSS images themselves. We show the test sample in § 2. We describe our programs for the search for galaxies with an effective diameter larger than the predefined value and for the calculation of their photometry using SDSS data in § 3, present the results for our test sample and analyze its SDSS data properties in § 4, and discuss them in § 5. The conclusions drawn from this study are summarized in § 6.

2. THE NEED FOR AND CREATION OF THE TEST SAMPLE

In order to find the best method for identifying LSB galaxy candidates in SDSS data, it is helpful to use a test sample with known properties. Our test sample is a subsample from the Impey et al. (1996) (ISIB96 hereafter) catalog, which overlaps with the EDR. The ISIB96 catalog and hence our test sample includes disk galaxies of various types, namely both high-surface-brightness (HSB hereafter) and LSB galaxies. We tried to pick a sufficiently large test sample in order to be able to study the various factors affecting an effective automatic selection procedure. The resulting sample consists of 92 galaxies from ISIB96 that lie in 93 "fields"[7] of the EDR "runs"[8] 752 and 756. Most fields only contain one ISIB96 galaxy. Several of these galaxies fall into the regions near the boundary of 2 adjacent fields, and thus were detected on both of them. In a few of the fields several sample galaxies are located. The whole area of these 93 fields on the sky, accounting for partly common boundary regions, is about 3 square degrees. 11 objects from this test sample are classified by ISIB96 as dwarf ellipticals without (dE) or with nuclei (dEn), while the remaining galaxies comprise various types of disk galaxies ranging from different types of spirals to Magellanic irregulars (Im) and dwarf irregulars (dIrr). In accordance with our intention to use disk galaxies of various types as a training set, the test sample that we selected from ISIB96 covers a range of central surface brightnesses $\mu_0(B)$ from 18.2 to 26.4 mag arcsec^{-2}. As follows from our measurements (see Section 5 for details) the fraction of LSB galaxies is indeed rather high: ≈36% of the galaxies with $\mu_0(B) \geq 23\overset{\mathrm{m}}{.}0$ arcsec^{-2} or ≈70% of the galaxies with $\mu_0(B) \geq 22\overset{\mathrm{m}}{.}0$ arcsec^{-2}.

3. DETECTION ALGORITHM

LSB galaxies are a subgroup of the general galaxy population and comprise primarily extended, quiescently evolving disk galaxies, irregular galaxies, and dwarf galaxies lacking extended starbursts. The SDSS pipeline automatically detects point sources and extended sources. The latter are mainly galaxies and include many LSB galaxies. Therefore, we first tested whether it is possible to exploit the SDSS EDR image database for the efficient selection of extended LSB galaxies and for the derivation of their main photometric and structural parameters. We carried out these tests on SDSS fields that included galaxies from our test sample (using the `sdssQT` query tool (see Stoughton et al. 2002, for a description and details)) and tried to recover these known LSB galaxies. We found that the standard procedures employed for the creation of the EDR catalogs to classify and measure photometric characteristics of objects split many extended galaxies with sufficiently prominent knots (such as luminous H II regions) into several separate entities, each listed as a galaxy of its own. This problem with sufficiently bright and extended galaxies was pointed out by other authors in the course of their work with EDR catalog data as well (Shimasaku et al. 2001; Yasuda et al. 2001; Stoughton et al. 2002; Blanton et al. 2001)[9] and is known as "galaxy shredding". The latter problem revealed the need for own photometry software to recalculate the integrated photometric parameters for the affected galaxies. Furthermore, many tests with various photometric parameters from the EDR, in the attempt to figure out the most efficient means to recover the test sample galaxies, have shown that either a significant (up to 30%) fraction of galaxies were missed, or that with relaxed selection criteria (which improved the detection rate of the test sample) a large number of unwanted objects was found, which in no way are related to the galaxies we are looking for. These unwanted objects exceeded several times the number of galaxies from the test sample, rendering this search method highly inefficient. For these reasons, we decided to create our own detection software.

---

[6] http://www.astro.princeton.edu/PBOOK/science/galaxies/galaxies.htm

[7] A "field" is SDSS terminology for an SDSS image covering ≈12′×10′.

[8] A "run" is one continuous scan obtained with the SDSS imaging camera.

[9] The situation has improved with the latest version of the SDSS photometric pipeline, PHOTO version 5.4, which will be used for future data releases, but the shredding problems continue to persist.

ISIB96 selected galaxies with angular sizes $D \gtrsim 30''$, where D is the major-axis diameter at the limiting isophote of the APM scans ($\mu_{\rm lim}(B) = 24.5\pm0.5$ mag arcsec^{-2} (Sprayberry, Impey & Irwin 1996) or $\mu_{\rm lim}(B) \sim 26$ mag arcsec^{-2} (Impey et al. 1996)). Therefore we have also chosen angular size as the primary criterion to select candidate galaxies. We used a simple algorithm for the detection and subsequent photometry of galaxies with large angular sizes on the SDSS images. The new programs that we created for these purposes are based on the Kitt Peak International Spectral Survey (KISS; Salzer et al. 2000) reduction package (Kniazev et al. 1997, 1998) and some programs from the Astrophysical Institute of Potsdam (`AIP`) package in MIDAS[10] (Lorenz et al. 1993; Vennik et al. 1996, 2000) for adaptive filtering and topological operations with masks.

The input data for our programs consist of: (1) – SDSS direct images (`fpC` files) for each field in the u, g, r, i and z filters, (2) – SDSS tables (`fpObj` files), where all information about the objects found in the field with PHOTO (Stoughton et al. 2002) is stored, and (3) – tables with astrometric and photometric coefficients extracted from the SDSS database with the `sdssQT` query tool. We tried to use as much information as possible from the SDSS database to simplify our software: information about positions of all objects identified as stars in the SDSS fields, astrometric coefficients, and coefficients for recalculations of measured fluxes into the SDSS photometric system. Knowledge of the positions of stars is important, since these objects act as contaminants for galaxy flux determinations.

The processing steps of our programs can be conveniently described in terms of 8 discrete tasks or modules: (1) alignment and combining of *gri* images; (2) filtering of the combined image; (3) object detection; (4) integrated photometry; (5) creation of surface brightness profiles (SBP hereafter); (6) rejection of false detections; (7) fitting of SBPs; (8) calculations of total magnitudes. We briefly outline these tasks below:

3.1. *Alignment and combination of gri images*

The goal of this task is to create a single combined direct image with better *signal-to-noise ratio* (*SNR* hereafter) as compared to the separate g, r, and i images. We concentrate on images obtained in these three filters since here the greatest photometric depth is reached. The combined image is used in the following steps for the detection of galaxies with large angular sizes. To work in the astrometric system of the SDSS we selected r-frame coordinates as reference coordinate system. We produce a geometrical transformation of the u, g, i, and z frames to the coordinates of the r frame for each field. For this we use the coordinates of the 100 bright unsaturated stars from the SDSS field, which we extract from the `fpObj` table. Since g, r, and i images have different $SNR_k = S_k/\sigma_k$ (where $k = g, r, i$, and S_k is the background level), and in order to obtain an optimal *SNR* ratio (Richter 1978; Knox et al. 1998) we used the weighted factors

$$w_k = \frac{S_k \sigma_g^2}{S_g \sigma_k^2} \qquad (1)$$

for averaging. Here the index g denotes the g-image, for which we use a weighting factor $w_g = 1$. For the estimation of the background level and noise dispersion at this and all consequent steps we use an algorithm that was developed for KISS reductions (Kniazev 1997), which is similar to that of Patat (2003). This robust algorithm is based on the calculation of a histogram distribution for pixel values of the frame and on fitting a Gaussian function to that histogram distribution.

3.2. *Filtering of the combined image*

This task serves to filter the combined image in order to decrease the noise of the background and thus to facilitate the detection of galaxies with the sufficiently low central surface brightness. We consider the problem of filtering as a problem of robust estimation of an average value in the window where objects of interest are mixed up with all other sources from the background noise. Different kinds of non-linear filters were used in the course of various LSB galaxy searches (Irwin et al. 1990; Dalcanton et al. 1997; Armandroff, Davies & Jacoby 1998). Proper filtering is a very important step. Our tests showed that 42% of the galaxies with $\mu_{\rm eff}(r^*) \geq 23$ mag arcsec^{-2} presented in this paper were detected only after we applied filtering. Without filtering they were not detected by our programs even when a threshold as low as 1.5σ of the noise of the combined *gri* frame was used. For $\mu_{\rm eff}(r^*) \geq 24$ mag arcsec^{-2} the number of galaxies that remain undetected without filtering is 90%.

Two criteria were used for the choice of the filter and smoothing window size: (1) the requirement to detect all galaxies from the test sample while minimizing false detections and (2) the requirement that the total calculation time required by all our programs should not exceed more than 1–2 months for ∼7000 SDSS fields that we plan to analyze in future (see Section 5.3). Finally, after a number of tests, we use the combination of two filters that work one after the other with the same window size of 27 pixels ($\approx 10\farcs5$): a smooth-and-clip (SAC) filter (Shergin, Kniazev & Lipovetsky 1996) and the fast median smoothing algorithm with circular window, implemented into MIDAS by Shergin (1997).

3.3. *Object detection*

We use simple thresholding to detect galaxies with large angular sizes at the surface brightness level above the limiting isophote. We divide this procedure into two separate iterations: (1) the detection of objects above the 3σ noise level on the unsmoothed combined images, (2) additional detection of objects above the 3σ noise level on the smoothed combined images. In both cases the σ of the noise is estimated by the same method as described in Section 3.1. Mask frames are generated during each step. These are frames where topologically isolated areas have their own unique integer labels. Such areas are called masks and show the location of the selected objects. For both steps we are looking for objects with areas of connected pixels at or above the detection threshold of 2900 pixels. This corresponds to the area of round objects with the radii R≥12″ or diameters D≥24″. This radius was selected as limit to detect the smallest galaxy in our test sample. In the course of the first iteration we usually detect all bright stars and bright large galaxies. Comparison with the positions of the 50 brightest stars from the `fpObj` table allows us to select all such cases in our list except for bright stars ($g^*, r^* \leq 15^m$)[11], which were usually classified as galaxies by the SDSS PHOTO software. We remove bright stars from our list but save their masks in the mask frame. The two mask frames after two iterations are joined into one and the areas around the brightest stars are excluded. Finally, all selected objects have their own mask labels and mask size with the isophotal level found in the smoothed combined image. For illustration, several of our detected galaxies with overplotted mask borders are shown in Figure 1.

---

[10] MIDAS stands for Munich Image Data Analysis System, the data reduction package of the European Southern Observatory.

No other criteria except the total area are used for the primary selection step. Objects with centers that are located closer than 40 pixels (≈16″) to the frame borders are rejected since most of them are detections of ghosts of bright stars. The centers of all selected objects are calculated using mask and filtered frames to exclude effects of background stars and possible bright H II regions. The position angle (PA) and axis ratio are calculated through the flux-weighted second-moments method (see, e.g., Stoughton et al. 2002) using masks and combined *gri* images.

3.4. *Integrated photometry*

This task is intended to derive accurate magnitudes and colors for the selected objects. Subimages are extracted from the images in the u, g, r, i and z bands (u and z images are transformed to the r coordinate system as described above). Their centers coincide with the centers of the selected objects while their sizes are 1.5 times larger than the masks created in the previous task. The latter is necessary for the correct local background determination and its proper subtraction. For each object the mask created with the previous task is increased by 10 pixels (∼4″) in all directions before the local background is calculated. All stars are subtracted from the image using their positions and Petrosian radii in each filter from the SDSS photometric database. All previously unrecognized background galaxies and foreground stars can be masked out by hand with additional circular masks.

A code for fitting the sky background from the `AIP` package for adaptive filtering is used, which constructs the background within the masked regions. This algorithm iteratively fills the background inside the mask by interpolating the background from the regions outside the mask (Lorenz et al. 1993; Vennik et al. 1996, 2000). This algorithm is used twice: (1) to subtract any contaminating sources like foreground stars or background galaxies and (2) to fit and subtract the sky background. After that the apparent flux is measured inside the same mask for background-subtracted *ugriz* images. The instrumental flux is transformed into the apparent magnitude in the standard SDSS photometric system. An example of several of our detected galaxies after preparation for the apparent magnitude calculation in the r-band is shown in Figure 1.

The total uncertainty of the instrumental magnitudes includes the uncertainty of the background determination σ_{sky} and the photon noise σ_{obj}, which can be calculated from Poisson statistics. Therefore the instrumental magnitude uncertainty σ_{instr} is computed for the cumulative flux CF in the total mask area N_{pix} with the value of the local background dispersion SKY:

$$\sigma_{instr} = 2.5 \cdot \log\Big(1 + \frac{\sqrt{\sigma_{obj}^2 + \sigma_{sky}^2}}{\sigma_{obj}^2}\Big), \qquad (2)$$

where $\sigma_{obj} = \sqrt{CF}$ and $\sigma_{sky} = \sqrt{N_{pix} \cdot SKY}$. The distributions of apparent r magnitudes, absolute r magnitudes ($\mathrm{M_r}$), velocities, calculated instrumental errors of the integrated magnitudes, PAs, and axis ratios for all galaxies found in the 93 test fields with our programs are shown in Figure 2.

3.5. *Creation of surface brightness profiles*

The next task creates $u^*g^*r^*i^*z^*$ SBPs of each detected galaxy using the background-subtracted images, which were used for the calculation of the integrated magnitudes. To simplify our programs and to make them more robust with regard to the creation of SBPs for galaxies with different morphologies, our software generates SBPs in the same way as PHOTO does (Stoughton et al. 2002), i.e., by measuring magnitudes in circular apertures. As the analysis in Bremnes, Binggeli & Prugniel (1999) showed, good agreement exists between an elliptical fit and circular aperture photometry. Standard SDSS software creates SBPs only for a constant number of apertures (15 apertures; Stoughton et al. 2002) at a fixed spacing. Our task is capable of measuring SBPs with any constant step size. We selected 1.″0 step sizes as the standard aperture steps for our work. The uncertainty of each SB level is calculated in the same way as the uncertainty of the integrated magnitude (with equation (2)). After a SBP is created, the effective radius $\mathrm{R_{eff}}$ (limiting the region of the galaxy, which contains the half of the light), the effective surface brightness μ_{eff} (the mean SB inside $\mathrm{R_{eff}}$), the radius of the region containing 90% of the integrated flux ($\mathrm{R_{90}}$), and the concentration index $\mathrm{C{=}R_{90}/R_{eff}}$ are calculated. As an example of the output from this task we show in Figure 3 SBPs in g and the radial $(g^* - r^*)$ color profiles for several galaxies from the test sample. We also use some programs from the `AIP` package to calculate the following parameters: the PA of the major axis for each filter, the axis ratio b/a for each filter, effective surface brightnesses $\mu_{\mathrm{eff}}^{\mathrm{AIP}}$, and effective radii $\mathrm{R_{eff}^{AIP}}$. All these additional parameters are calculated using the multilevel mask approach (Vennik et al. 1996, 2000), in which each region of intensities of the studied object is labelled with a different mask.

Apart from SBPs, our task calculates curves of growth to compare the final magnitude with the integrated magnitude calculated with the previous task. Usually these two magnitudes practically coincide. However, for galaxies located near the frame borders, whose masks are truncated by the borders, our programs in this task calculate galaxy parameters under the assumption that they are symmetric relative to their centers. The best illustration of such a case is NGC 4996, found as an additional (i.e., non-ISIB96) very extended galaxy in the fields containing the galaxies from the test sample. The difference between the magnitude calculated within the mask area on the frame, and that calculated for the "restored", extrapolated image is $\Delta m(g^*) = 0\overset{\mathrm{m}}{.}22$. This galaxy (as it was originally found) is reproduced in the left panel of Figure 4. In the right panel of the same Figure we show its "restored" image resulting from the assumption of symmetry beyond the frame borders.

---

[11] We note that EDR magnitudes will be referred to with asterisk superscripts in order to denote their preliminary nature in accordance with the recommended SDSS EDR usage (see Stoughton et al. 2002). As can be seen from Abazajian et al. (2003), the differences between the *ugriz* and $u^*g^*r^*i^*z^*$ photometric systems are small, typically no more than a few hundredths of a magnitude.

3.6. *Rejection of false detections*

After the primary selection algorithm identifies all sufficiently large objects and their model-independent parameters are calculated, we need to clean the list of false detections. This task is performed on an automatic level, subjecting the detected objects to selection criteria that identify: (1) very bright stars not recognized by PHOTO as stars and which are therefore selected by our programs in the course of the object detection procedure; (2) ghosts close to the borders of the SDSS fields that stem from bright stars located outside of our fields; (3) parts of extended halos around bright stars resembling the galaxies in which we are interested; (4) parts of satellite tracks. All these false detections selected in the primary selection have either very unusual colors, or bright effective surface brightnesses $\mu_{\rm eff}^{\rm AIP}$ calculated with `AIP` package. To be confident we have checked visually all the rejected objects in order to estimate the quality of our criteria. As our statistics show about 80% of all false detections were rejected during this stage.

Since our programs are very simple and, by design, are looking for extended objects, they cannot recognize all possible blends and other complicated cases (ghosts, parts of halos around bright stars) if these have photometric parameters close to "normal" galaxies. Such cases thus cannot be rejected by our task automatically either. Therefore, during the second step we interactively checked all remaining candidates by eye to identify such objects.

We applied our programs to all selected 93 SDSS fields where the 92 galaxies from the test sample are located. Altogether 245 candidates with sufficiently large angular sizes ($R \geq 12''$) were identified automatically in these fields in the course of the primary selection procedure. In the second step, as described above, most of the remaining bright stars (marked in the SDSS database as "galaxies" and therefore not rejected during the first step), their ghosts or parts of halos around them, and linear tracks from satellites were removed. This step resulted in the removal of 82 objects (or ~79% of all false detections among the non-galaxies). All objects remaining after these two steps have been checked by eye to identify possible complicated cases that were not rejected automatically. This step revealed 22 more false candidates (~21% of all false detections), which were then removed by hand.

3.7. *Fitting of SBPs*

This task produces fits to the $g^*r^*i^*$ SBPs created earlier. It is well known that the fitting functions should be based upon the physics of the formation and evolution processes. Unfortunately, these processes are still not well understood and the most commonly used functions are derived empirically. The fitting functions for elliptical galaxies and spiral galaxy bulges include the King model (King 1966) and de Vaucouleurs law (de Vaucouleurs 1953). Recently Andredakis, Peletier & Balcells (1995) suggested that a generalized version of the de Vaucouleurs profile ($r^{1/n}$) provides better bulge fits. On the other hand, Andredakis & Sanders (1994) and Beijersbergen, de Block & van der Hulst (1999) suggest that late-type spirals often have bulges best fitted by an exponential. Exponentials (Freeman 1970) and inner-truncated exponentials (Kormendy 1977) are usually used for the disk components of spiral galaxies.

Our programs follow the scheme to fit both the disk and bulge components with exponential SB profiles to measure their central surface brightness μ_0 and scale length α. The equation for such profiles in logarithmic scale usually looks as follows (Sérsic 1968):

$$\mu(R) = \mu_0 + 1.086 \cdot (R/\alpha)^n, \qquad (3)$$

where R is the distance along the axis and n is taken to be 1 for both bulge and disk. In very rare cases for dwarf galaxies (e.g., Jerjen, Binggeli & Freeman (2000)) with obvious $n > 1$ we fit the profile with only a disk and with n as an additional parameter.

This task is interactive and is based on the MIDAS `FIT` package (MIDAS Users Guide 1995), which uses different methods for performing a nonlinear least-squares fit of the data to a specified function. It also allows control over the inclusion of different parameters and the range of the data to be fitted. Our program performs the fitting on the surface intensity data and accomplishes an optimized fit by minimizing the weighted rms deviation of the data from the fit function. It calculates weights as $w_k = \sigma_k^{-1}$, where σ_k is the uncertainty calculated for each SB level with the previous task for the creation of SBPs. Some examples of our fitting are presented in Figure 3.

We also incorporated the de Vaucouleurs profile ($n = 1/4$) in our fit task in order to have the possibility (1) to automatically classify our observed SBPs by comparing them to different model light profiles and finding the model profile with the smallest χ^2 difference, and (2) to get fit parameters for bright elliptical galaxies in future applications of our programs.

3.8. *Total magnitudes*

Our method of galaxy detection and the subsequent determination of their integrated magnitudes is essentially isophotal photometry with a sufficiently deep isophotal detection limit ($\mu_{\rm lim}$) that will be discussed in more detail in Section 5.1. It is well-known that unlike for point sources, the fraction of light of a galaxy contained within the limiting isophote $\mu_{\rm lim}$ is a function of several parameters such as central surface brightness μ_0, redshift, point-spread function (PSF), and cosmological dimming (see, e.g., Dalcanton (1998)). In our case the minimal diameter of the selected galaxies of $24''$ is much larger than the PSF, since the typical seeing in the SDSS EDR images is $\sim 1\overset{''}{.}5$ (Stoughton et al. 2002). Thus any sample, selected with this method from SDSS images, will be independent of the PSF. In the case of a purely exponential surface brightness profile (equation (3) with $n = 1$) it can be shown in simple analytical form that the ratio of the total galaxy flux to that observed within the limiting isophote $\mu_{\rm lim}$ (Allen & Shu 1979; Impey, Bothun & Malin 1988) obeys

$$\frac{F_{\rm lim}}{F_{\rm tot}} = 1 - (1 + n_\alpha) \cdot e^{-n_\alpha}, \qquad (4)$$

where n_α is the number of scale lengths α observed within the limiting isophote. And in the general case n_α is given by

$$n_\alpha = \frac{\mu_{\rm lim} - \mu_0 - 10 \cdot \log{(1+z)} - k(z)}{1.086}, \qquad (5)$$

where $10 \cdot \log{(1+z)}$ is a term accounting for the $(1+z)^4$ cosmological dimming in surface brightness and $k(z)$ is a term to correct for the redshifting of the spectral energy distribution (the k-correction). The dependence of a fraction of the light above the limiting isophote on $(1+z)^4$ is illustrated in Dalcanton (1998). In Figure 5 we show the behaviour of the $F_{\rm lim}/F_{\rm tot}$ ratio versus the central surface brightness μ_0 for various values of the limiting isophotes. In real galaxies the situation is, of course, more complicated. The true ratio $F_{\rm lim}/F_{\rm tot}$ is higher for galaxies with detectable bulge subsystems or Sérsic SBPs ($n > 1$ in equation (3)).

If one wishes to avoid such a systematic bias in the determination of magnitudes, it is possible to calculate total magnitudes $\mathrm{m}_{\rm tot}$ integrated out to infinity (for equation (3) with $n = 1$) using the equation

$$m^d_{\rm tot} = \mu_0 - 5 \cdot \log_{10}(\alpha) - 2.5 \cdot \log_{10}(2\pi) \qquad (6)$$

Here α is in arcsec and index 'd' refers to a purely exponential disk. The last term is ≈1.995. It is, however, difficult to get very accurate values for $\mathrm{m}_{\rm tot}$, since they depend on the accuracy of the scale length and μ_0 derived during the fit procedure and thus introduce extra uncertainties

$$\sigma_{\rm model} = \sqrt{\sigma^2_{\mu_0} + \Big(\frac{5\sigma_\alpha}{\alpha}\Big)^2} \qquad (7)$$

As one can see in Figure 6 (top and middle panels), the mean uncertainty of the central surface brightness in, for example, the g band is about 0.12 mag arcsec^{-2}, and the mean relative uncertainty of the scale length in this filter is ∼4%. The respective median parameters are 0.08 mag arcsec^{-2} and ∼3%. This leads to the mean value of $\sigma_{\rm tot}$ of $0\overset{\rm m}{.}25$ (or median value of $\sigma_{\rm tot}$ of $0\overset{\rm m}{.}17$), since it is $\geq \sigma_{\rm model}$ with equation (7). To decrease this error and to take any excess non-disk light into account, our program calculates $m_{\rm tot}$ as the sum of two components: (1) the integrated magnitude inside $\mu_{\rm lim}$ (see Section 5.1 for the determination of $\mu_{\rm lim}$ values in different SDSS bands) and (2) a part of an extrapolated disk for $\mu > \mu_{\rm lim}$, which is easy to calculate from equation (4) and equation (6). The full uncertainty in this case is calculated as

$$\sigma_{\rm tot} = \sqrt{\sigma^2_{\rm instr} + \frac{F_{\rm tot} - F_{\rm lim}}{F_{\rm tot}} \cdot \sigma^2_{\rm model}}, \qquad (8)$$

where $\sigma_{\rm instr}$ is the uncertainty in the instrumental magnitude calculated with equation (2). As one can see, for example, $\sigma_{\rm tot}$ for g calculated in this way (bottom panel of Figure 6) is a factor of three lower than the value derived by a standard method: the mean value is of $0\overset{\rm m}{.}08$ and the median one is of $0\overset{\rm m}{.}06$.

In a few cases where we used the Sérsic profile (equation (3) with $n > 1$), to calculate parameters like $F_{\rm tot}$ and $\sigma_{\rm model}$, we used the modified formula for $m_{\rm tot}$ instead of formula (6) (see, e.g. MacArthur, Courteau & Holtzman (2003); our and their n are defined inversely of each other):

$$m^{\rm Sersic}_{\rm tot} = m^d_{\rm tot} - 2.5 \cdot \log_{10}\Big(\frac{1}{n} \cdot \Gamma\Big(\frac{2}{n}\Big)\Big), \qquad (9)$$

where $m^d_{\rm tot}$ is exactly the expression from formula (6) and $\Gamma(x)$ is the Gamma function. For the range of n ($1 \leq n \leq 4$), which is sufficient for our goals, it can be well estimated from the approximation of $\Gamma(x)$ by the Stearling series (e.g., Korn & Korn (1961), formula 24-4-10). The respective additional term $\sigma_{\rm add}(n)$, depending on n, will appear in the expression for $\sigma^2_{\rm tot}$

$$\sigma_{\rm tot} = \sqrt{\sigma^2_{\rm instr} + \frac{F_{\rm tot} - F_{\rm lim}}{F_{\rm tot}} \cdot (\sigma^2_{\rm model} + \sigma^2_{\rm add})} \qquad (10)$$

It can be estimated with an accuracy of ∼10% as follows:

$$\sigma_{\rm add} \approx \frac{2.17 \cdot \sigma_{\rm n}}{n^2} \cdot \Big(\ln\Big(\frac{2}{n}\Big) + \frac{n}{4}\Big), \qquad (11)$$

where $\sigma_{\rm n}$ is uncertainty of the index n as one of the fitting parameters.

4. RESULTS

4.1. *Detected galaxies*

After the cleaning the list of originally selected objects from false detections (Section 3.6) we were left with 141 objects selected as galaxies of sufficiently large size (with 'equivalent' diameter $D \geq 24''$). We also cleaned our sample from the evident elliptical (E) galaxies, as unwanted non-LSB objects. They were rejected after the SBP fitting procedure. Altogether we identified and removed from our sample 9 galaxies (∼6%) with SBPs typical for ellipticals and were finally left with 132 galaxies. Of these 132 non-E galaxies 3 objects were detected independently in two different, partially overlapping SDSS fields. Therefore, we ended up with 129 unique non-E galaxies.

The list of test sample galaxies is given in Table 1. It also includes additional galaxies that we found in the same SDSS fields, applying the same selection criteria (see Section 4.1) as for the galaxies from ISIB96 sample. Therefore, the total number of galaxies in Table 1 is 129. The table contains the following information:

column 1 – Galaxy name based on the equatorial coordinates for equinox J2000.

column 2 – Galaxy names as given in the paper by ISIB96. If not from ISIB96, this entry is blank.

columns 3–4 – Right ascension and declination for equinox J2000. These coordinates were measured on the SDSS images, using the programs described in Section 3.

column 5 – SDSS image identification (run number, column, and field).

column 6 – Apparent B-magnitude and its error. Both were recalculated from g^* and r^* integrated magnitudes using of equations from Smith et al. (2002).[12]

---

[12] We did not find any large and/or systematic differences when using the transformation equations of Fukugita et al. (1996) or of Smith et al. (2002) for the calculation of $UBVR_cI_c$ magnitudes from $u^*g^*r^*i^*z^*$ magnitudes for our galaxies. We thus adopt the equations from Smith et al. (2002) throughout the paper.

column 7 – $(B-V)$ color, calculated from g^* and r^* magnitudes using the respective equations from Smith et al. (2002).

column 8 – Absolute B-magnitude, calculated from the apparent B-magnitude in the previous column and the distance derived from the known heliocentric velocities, assuming a Hubble flow with H_0= 75 km s^{-1} Mpc^{-1}, with no corrections for the motion of the Sun and Local Group. No corrections have been made for Galactic foreground extinction.

column 9 – Heliocentric velocities taken from ISIB96, from the SDSS EDR database and the NASA/IPAC Extragalactic Database (NED).

column 10 – Morphological classification in the system of de Vaucouleurs et al. (1991). This classification was based on that suggested in ISIB96 and NED, where applicable. However, accounting for the superb quality of the SDSS images relative to most of the previously available data, we have checked the classification for all sample galaxies and revised it in a number of cases. For the remaining galaxies the classification was also done by the authors.

column 11 – One or more alternative names, according to the information from the NED.

Of the 132 detected objects, 87 are from our test sample of 92 galaxies. They appeared as 90 detections in 93 fields, thus three of these 87 galaxies were detected twice in overlapping fields. This implies a detection rate of our algorithms of 87/92, or ∼94%. In fact, we have found that the two dimmest objects of the ISIB96 test sample (0956−0034 with $\mu_0(B)$=25.8 mag arcsec^{-2} and 1304+0054 with $\mu_0(B)$=26.5 mag arcsec^{-2} according to ISIB96) are very likely artifacts, as explained below. Indeed it is hard to understand how ISIB96 could detect an object with $\mu_0(B)$=26.5 mag arcsec^{-2}, if their limiting isophote in the APM scans was $\sim$ 26 mag arcsec^{-2}). Following the analysis of the possible range for μ_0 in Section 5.1, we know that our software is capable of detecting objects with $\mu_0(g^*) = 26.2$ mag arcsec^{-2} (recalculated from $\mu_0(B) = 26.5$ for 1304+0054 mag arcsec^{-2} assuming that the object is very blue with $(g^* - r^*) = 0\overset{m}{.}3$), if their $\alpha > 30''$. For redder objects the detectability is even higher. But even if these galaxies are less extended than the scale length limit that we imposed, and thus cannot be detected by our programs with their fixed limiting parameters, they should be visible on the SDSS images. We have checked carefully their positions on the combined g, r, i SDSS images, which certainly are deeper than the UKST plates used by ISIB96. Nothing is seen at the positions where the ISIB96 finding charts show some fuzzy objects.

We also obtained images at the positions of these two galaxies in the framework of the Key Project for SDSS Follow-up Observations at the Calar Alto Observatory in Spain (Grebel 2001). We used the Calar Alto Focal Reducer and Faint Object Spectrograph (CAFOS) at the 2.2-m telescope in direct imaging mode. CAFOS was equipped with a 2048 × 2048 pixels SITe CCD with an image scale of $0.53''$ pixel^{-1}, resulting in a field of view of $16' \times 16'$. The observations consisted of 3×20-min exposures in the Gunn g-band (i.e., deeper than the 54s exposures in the SDSS g-band obtained with the SDSS 2.5-m telescope at Apache Point Observatory). We did not find anything obvious at the positions of these two galaxies in these new direct images. We therefore conclude that the detections noted by ISIB96 are probably caused by photographic plate defects. The occurrence of artifacts among some of the faintest galaxies in the sample of ISIB96 was also noticed by Karachentseva & Karachentsev (1998). Accounting for these false "galaxies" from the test sample, the real detection rate of our algorithms approaches 87/90 (∼96.5%).

The three remaining galaxies from the test sample were not detected by our automatic algorithms for similar reasons. 1331−0002 (name from ISIB96) is near a very bright star. 1025−0040 is also near a very bright star, coinciding with one of the diffraction spikes of this star on the SDSS images. 1103+0010 is located in the halo of galaxy NGC3521 with B=$10\overset{m}{.}0$. Thus, summarizing the results for the non-detected galaxies from the test sample, we conclude that with our rather simple automatic algorithms, we lose a few galaxies in the vicinity of bright objects. However, their fraction is fairly small, ∼3% from the test sample.

42 galaxies were found in addition to the 87 detected galaxies from the test sample within the same 93 SDSS fields. All these objects were selected objectively with the same criteria that we predefined to recover all galaxies from the test sample. To the 90 true galaxies from the test sample, the additionally detected 42 new galaxies add another 47%, i.e., almost half as many new galaxies in addition to the number previously known.

Several model-independent observational parameters derived from the integrated photometry of the test sample and of the additionally found galaxies are presented in Table 2. It includes the following columns: u^*, g^*, r^*, i^*, z^* integrated magnitudes with their errors, axis ratio b/a, position angle PA, and some additional parameters of these galaxies in the r-band: the effective radius $R_{\rm eff}(r^*)$, mean surface brightness inside this radius $\mu_{\rm eff}(r^*)$, concentration index C(r), and $a_{26.2}(r^*)$ – size for $\mu_{\rm lim}(r^*) = 26.2$ mag arcsec^{-2}. For all sample galaxies, whose SBPs were fitted with double exponential disks (disk and bulge), we present in Table 3 the following model photometric parameters: $\mu_0^d(g^*)$, $\alpha^d(g^*)$, $\mu_0^b(g^*)$, $\alpha^b(g^*)$, $\mu_0^d(r^*)$, $\alpha^d(r^*)$, $\mu_0^b(r^*)$, $\alpha^b(r^*)$, $\mu_0^d(i^*)$, $\alpha^d(i^*)$, $\mu_0^b(i^*)$, $\alpha^b(i^*)$, where the index 'd' refers to a disk and 'b' refers to a bulge. For those sample galaxies, whose SBPs were fitted with the Sérsic profile, the respective model parameters $\mu_0(g^*)$, $\alpha(g^*)$, $n(g^*)$, $\mu_0(r^*)$, $\alpha(r^*)$, $n(r^*)$, $\mu_0(i^*)$, $\alpha(i^*)$, $n(i^*)$ are presented in Table 4. Four obviously interacting systems, 1113+0107, 1208+0120, 1250−0009, and 1327−0020, were not included in the latter two tables.

4.2. *Total versus apparent magnitudes*

In Figure 7 we show the difference between apparent and total g^* and r^* magnitudes versus apparent magnitudes for galaxies from our sample. The total magnitudes were calculated as described in Section 3.8. The mean difference Δg(Apparent−Total) is $0\overset{m}{.}04 \pm 0\overset{m}{.}04$, which is well consistent with the mean value of the total error for this band, $\sigma_{\rm tot}(g^*) = 0\overset{m}{.}08$. Only 17 galaxies ($\sim$ 13% of the total number of the sample galaxies) have $\Delta g^* > 0\overset{m}{.}08$, and only 4 galaxies ($\sim$ 3%) have $\Delta g^* > 2 \cdot \sigma_{\rm tot}(g^*)$. The situation is similar for the r and i filters. As was described in Section 3, the total magnitudes in our method are available only after fitting SBPs. This is due to the need to extrapolate the apparent light profile. While developing our software, we tried to use the extrapolation of curves of growth in order to calculate total magnitudes. However, we found that in any case we need to choose different types of extrapolation. They are different for pure exponential disk, Sérsic profile, and bulge plus disk systems, and thus need to be taken into account when fitting the SBPs. Therefore, our total magnitudes are derived only for the g, r and i filters, since we confine our SBP determinations to these three filters. For the u and z filters we do not perform this procedure, since the uncertainty of the additional light contributions affecting these extrapolations is in most cases significantly larger than the value of the respective term. As Figure 7 shows, our apparent magnitudes are often a sufficiently good approximation of the total magnitudes. For example, in Section 4.3 we compare our magnitudes and NED magnitudes for objects with brightnesses up to $B = 15\overset{\rm m}{.}5$ (see Figure 8), i.e., to $g^* \sim 15\overset{\rm m}{.}0$ for the typical color index $(g^* - r^*) = 0\overset{\rm m}{.}5$. As one can see in Figure 7, most of our galaxies in this magnitude range have Δg^* and Δr^* less than $0\overset{\rm m}{.}03$. Therefore it will be only a minor difference when using apparent magnitudes instead of total magnitudes, if total magnitudes are not available.

4.3. *Photometric quality*

To examine the photometric quality of our data and to check our programs we tested our results in two ways: (1) we compared the magnitudes obtained for the same objects detected in different SDSS fields (observed either within the same run, or in two different runs) as an internal consistency check, and (2) we compared our magnitudes for previously known objects with the results of published photometry from the literature as an external consistency check.

Three galaxies from the test sample each were found in 2 different fields. Thus, they were measured independently twice, and their integrated magnitudes are suitable to check the quality of our photometry and reliability of our error estimates. This comparison is shown in Table 5. One can see that the integrated magnitudes for the two independent measurements of the galaxies SDSS J113457−004514 and SDSS J144856−004337, found in different fields of the same run, are consistent in all bands, since they differ only by 1–3σ of the cited uncertainties. This implies that galaxies located in adjacent fields of the same run do not show significant differences in their total magnitudes. This repeatability underlines both the data quality and correct functioning of our programs. In both fields we are dealing with the same object from the same run. Because the adjacent SDSS fields have common regions with a width of 128 pixels (Stoughton et al. 2002), our programs found these galaxies in two fields, and the only difference is global and local background and noise determination. The same situation holds for galaxy SDSS J135230+002504, found in two fields of *different* runs. Therefore, we can state that we do not see any differences in the calibration between the SDSS runs 752 and 756. Since one galaxy is too little for statistics, the planned future extension of this study to a much larger number of SDSS fields (of the same two interleaving runs, see Section 5.3) will yield many more pairs of independent photometric measurements.

In Figure 8 (top-left panel) we show the comparison of our integrated magnitudes (transformed to B-band magnitudes using the equations from Smith et al. 2002) with $B_{\rm tot}$ magnitudes of ISIB96. The comparison of our integrated B-band magnitudes with those from ISIB96 shows that although the majority of the galaxies exhibit photometric scatter consistent with the uncertainties for the ISIB96 sample (typical uncertainties cited by ISIB96 are $\sim 0\overset{\rm m}{.}07$ for galaxies with CCD photometry and $\sigma \sim 0\overset{\rm m}{.}25$ for those without), there are about a dozen galaxies that significantly deviate from the expected mean difference ΔB(Our−Impey)=0. The latter galaxies result in a weighted r.m.s. of $0\overset{\rm m}{.}55$. We have checked carefully every object exhibiting a large difference. However, no reasonable explanation was found. We did not find any new B-band photometry for this sample in Burkholder, Impey & Sprayberry (2001) or Impey, Burkholder & Sprayberry (2001), where instead the same magnitudes as in ISIB96 are used.

As an additional test, we compared our values, (transformed to $UBVR_cI_c$-band magnitudes using Smith et al. 2002) and the ISIB96 B-band magnitudes with an independent dataset, extracted for several bright galaxies from NED. 17 galaxies from our sample also have B-band magnitudes listed in the NED, and 12 of these are galaxies from ISIB96, which are shown by filled circles on the top-right panel of Figure 8. Therefore, even if we consider that NED data come from many different sources and do not constitute a uniform dataset as such, we expect that the comparison of our photometry with NED photometry and the comparison of ISIB96 photometry and NED data should show similar trends (if any).

The comparison shows that our magnitudes (in B-band, as well as in other broad bands), after accounting for the uncertainties cited in NED (Figure 8, both bottom panels), are well consistent with the magnitudes from NED. In particular, for the 12 ISIB96 galaxies in common with our sample and with NED the weighted r.m.s. of ΔB(Our−NED) is $0\overset{\rm m}{.}29$. For all 17 galaxies in common with our list and NED the weighted r.m.s. of ΔB(Our−NED) is $0\overset{\rm m}{.}25$. For four galaxies, which we find to have B fainter by $0\overset{\rm m}{.}5$–$0\overset{\rm m}{.}6$ than NED, the difference is most likely due to projected stars, which were subtracted in our data, but presumably remained in the photoelectric diaphragm photometry, cited by NED from the Third Reference Catalogue of Bright Galaxies (RC3) (de Vaucouleurs et al. 1991). The role of superimposed stars in diaphragm photometry is, on average, larger for fainter galaxies. If we account for this trend in the comparison between our and NED photometry, the resulting r.m.s. for ΔB(Our−NED) will decrease to $\sim 0\overset{\rm m}{.}18$, fully consistent with the cited NED errors, since our uncertainties for this range of magnitudes are significantly smaller ($0\overset{\rm m}{.}01$ – $0\overset{\rm m}{.}03$).

The comparison of the B-magnitudes of galaxies from ISIB96 with NED shows larger scatter, significantly exceeding the amount expected from their cited uncertainties. The weighted r.m.s for ΔB(ISIB96−NED) is $0\overset{\rm m}{.}8$. For extreme cases the difference between ISIB96 magnitudes and those listed in NED amounts to up to $1\overset{\mathrm{m}}{.}0$–$1\overset{\mathrm{m}}{.}5$. This suggests that besides the random errors in the ISIB96 sample, some of their galaxies suffer from rather large systematic shifts. Further support of this conclusion can be found in Sprayberry et al. (1995), where one additional measurement is presented for the galaxy 1226+0105 from ISIB96. Its magnitude in ISIB96, B=$15\overset{\mathrm{m}}{.}7$, is very different from our value for this galaxy, B=$16\overset{\mathrm{m}}{.}34$. Sprayberry et al. (1995) obtained CCD photometry of this galaxy and measured B=$16\overset{\mathrm{m}}{.}10\pm0\overset{\mathrm{m}}{.}07$. The latter value is already corrected for Galactic extinction, k-correction, and cosmological dimming $(1+z)^2$. After the de-correction for dimming ($\mathrm{V_{hel}}$ = 23655 km s^{-1}, (Sprayberry et al. 1995)) and extinction we get B=$16\overset{\mathrm{m}}{.}27$, which is within the 1σ uncertainty of our B-magnitude.

As the last test we show CCD BV total photometry from Salzer, MacAlpine & Boroson (1989) for 5 galaxies in common with our sample. We analyzed these measurements separately from the NED because they are a uniform set of observations and have fainter magnitudes than the galaxies listed in the NED. Four of these galaxies are also part of the ISIB96 data. The comparison of these published magnitudes with our photometry is shown in the right panels of Figure 8 with asterisks. These comparisons show the same picture as above: (1) the mean difference ΔB(Our−Salzer) is $-0\overset{\mathrm{m}}{.}06\pm0\overset{\mathrm{m}}{.}03$ and the mean difference ΔB(ISIB96−Salzer) is $-0\overset{\mathrm{m}}{.}32\pm0\overset{\mathrm{m}}{.}07$; (2) the weighted r.m.s. for ΔB(Our−Salzer) is $0\overset{\mathrm{m}}{.}06$ and weighted r.m.s. for ΔB(ISIB96−Salzer) is $0\overset{\mathrm{m}}{.}15$ (in both cases only the four common galaxies were used). This lends further support to our conclusion that the absolute accuracy of our SDSS photometry as compared to external data is $\leq 0\overset{\mathrm{m}}{.}1$.

Additionally, Figure 8 (both bottom panels) demonstrates that our software allows us to get reliable magnitudes even for galaxies as bright as $\sim10\overset{\mathrm{m}}{.}0$ in B-band from SDSS data, whereas galaxies this luminous are excluded from the public SDSS photometric database. Most of the NED magnitudes for passbands other than B are from CCD observations, while B-band magnitudes are mainly photoelectric. In the other bands we therefore see even better consistency between the magnitudes compiled in the NED and our total magnitudes. Since, unfortunately, there are only a few measurements in each band, we estimated the scatter of the combined data in the remaining UVRI bands. The mean difference $\Delta UVRI$(Our−NED) is $0\overset{\mathrm{m}}{.}03\pm0\overset{\mathrm{m}}{.}04$, and the weighted r.m.s. $\Delta UVRI$(Our−NED) is $0\overset{\mathrm{m}}{.}12$.

Thus, summarizing the results of the comparison of our new photometry with the B_{tot} magnitudes from ISIB96 and NED we conclude that: (1) In general the agreement is very good for the different bands, and our photometry results are reliable; (2) The external quality of photometry for SDSS data is about the same for the different bands and has a precision of $\leq 0\overset{\mathrm{m}}{.}1$; (3) With our software we are capable of obtaining accurate photometry also for all bright (non-LSB) galaxies within the studied sky region, while photometry for many of these galaxies is not available from the SDSS database or has larger uncertainties. This is an important by-product of our programs, since a large fraction of bright galaxies has either only photoelectric photometry (de Vaucouleurs et al. 1991) or CCD photometry only in one or two bands.

4.4. *Quality of structural parameters*

To investigate the quality of structural parameters of our data we compared them with the data from ISIB96. We emphasize that our definition of μ_{eff} is different from the one used by ISIB96. Their μ_{eff} corresponds to the surface brightness in the narrow annulus with a mean radius equal to R_{eff}. If these parameters would be defined for the same band, then for a pure exponential disk μ_{eff} as defined by ISIB96 should be $0\overset{\mathrm{m}}{.}70$ fainter than according to our definition.

In Figure 9 we compare our parameters $\mathrm{R_{eff}}(g^*)$, $\mu_{\mathrm{eff}}(B)$, and $\mu_0(B)$ with the corresponding ones in ISIB96. Interacting galaxies as complex, composite systems were not included in this comparison. As shown in the upper panel of Figure 9, the values of the model-independent parameter $\mathrm{R_{eff}}$ obtained in the present work for the test sample galaxies are in good agreement for most of the galaxies in ISIB96. The difference is within 1–2 combined σ of $\mathrm{R_{eff}}$. To estimate this parameter we used $\sigma_{R_{\mathrm{eff}}}$ derived directly from our measurements and the estimate for a purely exponential disk for ISIB96 data, based on their $\sigma_{\mathrm{tot}} = 0\overset{\mathrm{m}}{.}25$. This results in a relative error of $\mathrm{R_{eff}} \sim 0.15$. Only for five galaxies (that is, 6%) are the differences significant. They exceed 2σ of the combined error, and it is difficult to explain them by random errors. Since all our data are of uniform quality, we can suggest that a few galaxies of ISIB96 are based on lower quality data (as follows also from our photometry comparison in Section 4.3), which caused larger uncertainties in the determination of their $\mathrm{R_{eff}}$ as well.

The parameter $\mu_{\mathrm{eff}}(B)$ is more difficult to compare (middle panel of Figure 9), since only for pure exponential disks our defined value (the mean inside $\mathrm{R_{eff}}$) and the ISIB96 parameter (μ of the narrow annulus at $\mathrm{R_{eff}}$) can be converted into each other through a simple relation. Even when accounting for this "disk" difference, the scatter is still significant and shows some systematic deviations on both high and low surface brightness levels. The typical uncertainty of the photometric calibration of the photographic plates used in the work by ISIB96 is $\sim0\overset{\mathrm{m}}{.}25$ (Sprayberry, Impey & Irwin 1996). This implies that the uncertainty of their $\mu_{\mathrm{eff}}(B)$ is at least at this level. Besides the term related to $\sigma_{\mu_{\mathrm{eff}}}$ should be added. Thus, $\sigma_{\mu_{\mathrm{eff}}}$ is calculated with the equation

$$\sigma_{\mu_{\mathrm{eff}}} = \sqrt{\sigma^2_{\mathrm{tot}} + \left(2.17 \cdot \frac{\sigma_{R_{\mathrm{eff}}}}{\mathrm{R_{eff}}}\right)^2}, \tag{12}$$

where σ_{tot} is the uncertainty in the total/observed magnitude and $\sigma_{R_{\mathrm{eff}}}$ is the uncertainty for R_{eff}. As discussed above, the error in $\mathrm{R_{eff}}$ for our data was estimated directly. For ISIB96 data it was estimated for a purely exponential disk as 0.15 of $\mathrm{R_{eff}}$.

The combined error bars for the differences in μ_{eff} are shown in the middle panel of Figure 9. The great majority of the data from our SDSS parameters and those from ISIB96 are consistent within 2σ of the combined error ($\sim0\overset{\mathrm{m}}{.}8$–$1\overset{\mathrm{m}}{.}0$). However, for about 20% of the galaxies the differences are larger. As follows from Section 4.3, the uncertainties of our photometry are significantly lower than those from ISIB96. Thus the total uncertainties for the differences in μ_{eff} will be defined mainly by uncertainties from Sprayberry, Impey & Irwin (1996). Therefore, large deviations (i.e., more than twice the combined σ, or $\sim 0.^{m}8$–$1.^{m}0$) should be attributed both to the mentioned photometry problems for some objects in ISIB96 and to differences in the definition of $\mu_{\rm eff}$.

Of greater concern, however, are the rather large differences apparent in the comparison of the model-dependent central surface brightness $\mu_0(B)$ that is shown in the bottom panel of Figure 9. For each point the total uncertainty includes the $0.^{m}25$ from ISIB96 and the uncertainty that was defined in course of our fitting procedure. In reality, the average uncertainty for $\mu_0(B)$ given by ISIB96 should probably be at least two times larger than average uncertainty of the total magnitude. We show, therefore, the average combined 2σ level as $1.^{m}0$. However, even with this 2σ uncertainty level about 23% of objects exhibit larger deviations. In particular, in many cases, for galaxies with a central luminous component such as a bulge or bar, the parameter $\mu_0(B)$ from ISIB96 was significantly brighter than ours. Since our surface photometry is very deep, in most of these cases we could see that the value presented by ISIB96 refers to the $\mu_0(B)$ of this central brighter component, but not to the underlying disk, in spite of ISIB96's description of their procedure for the derivation of $\mu_0(B)$. In Figure 3 we show, as an illustration, SB profiles of two such cases. According to ISIB96, the galaxy 1212−0039 has $\mu_0(B)$=22.40 mag arcsec^{-2}, while 1349+0039 has $\mu_0(B)$=20.30 mag arcsec^{-2}. For seven galaxies we found that ISIB96 give a $\mu_0(B)$ significantly lower ($>1.^{m}0$) than what we derive. We show SBPs of two of these galaxies in Figure 3 to illustrate that according to our data it would be very difficult to get such a large error. According to ISIB96, 1213+0127 and 1442+0026 have $\mu_0(B)$=22.10 mag arcsec^{-2} and 24.10 mag arcsec^{-2}, respectively.

Only for one galaxy, 1226+0105 from the test sample, we found a SBP published in the literature. According to ISIB96, its $\mu_0(B)$=20.90 mag arcsec^{-2}, which differs considerably from our $\mu_0(B)$=22.94±0.11 mag arcsec^{-2}. On the other hand, according to Sprayberry et al. (1995), its uncorrected $\mu_0(B)$=23.00±0.14 mag arcsec^{-2}, which is very close to our value.

To summarize, we exploited the superb quality of the SDSS imaging data to re-measure the structural and photometric properties. We then compared our results with the published data for the test sample galaxies. For a substantial number of galaxies the estimates of some parameters that are important for further analysis are improved in comparison to the values derived in the original work.

5. DISCUSSION

5.1. *The selection thresholds of our method*

In a later paper we will address issues concerning the resulting selection function, and completeness via Monte-Carlo simulations of the selection process. However, some useful estimates for the selection thresholds of our method can be derived using very simple models and through the measured parameters of the detected galaxies.

5.1.1. *Limiting isophote*

The use of highly homogeneous SDSS images obtained in drift-scan mode and of a very simple primary selection criterion (total area) allow us to easily estimate the limiting isophote parameter of our selection procedure. However, the use of combined *gri* and filtered images to search for galaxies makes the estimation of this criterion more complicated. As a first step, we tried to estimate the limiting isophote in the g filter ($\mu_{\rm lim}(g^*)$) using the background level and noise estimation on g band images before combining, after combining, and after filtering of the combined frames. This is possible only because our background level for images in the g filter and in the combined images is the same as follows from our description of the steps for aligning and combining the *gri* images (see Section 3.1 for details). We carried out such estimates for several randomly selected fields. They show that we have a mean limiting surface brightness 3σ isophote $\mu_{\rm lim}(g^*) \approx 26.4$ mag arcsec^{-2}. Unfortunately, devising a similar procedure of estimating $\mu_{\rm lim}$ for other bands is less straightforward.

Next, we tried to estimate the limiting surface brightness isophote analytically using the following equation for a pure exponential surface brightness profile (Allen & Shu 1979):

$$m_{\rm tot} = \mu_0 + 5 \cdot \log_{10}\Big[\frac{0.7349}{\theta_{\rm lim}}(\mu_{\rm lim} - \mu_0)\Big] \qquad (13)$$

In this equation $\theta_{\rm lim}$ is the limiting angular diameter (in arcsec) of the galaxy with an exponential SBP at the limiting surface brightness isophote $\mu_{\rm lim}$. Since μ_0 and $\mu_{\rm lim}$ in this equation refer to the same band as $m_{\rm tot}$, we can apply equation (13) to any photometric band of interest. The expression for $\theta_{\rm lim}$ may be used for any angular-limited sample. For example, Impey, Bothun & Malin (1988) applied it to analyze selection effects based on the structural parameters for a sample of LSB galaxies found in the Virgo Cluster.

In our case $m_{\rm tot}$ for a purely exponential SBP can be calculated using the fit parameters and equation (6). The limiting surface brightness is defined as the level above which we detected our objects. It can therefore be determined by comparison with a grid of model curves from equation (13) with $\mu_{\rm lim}$ as a parameter. Since we defined our limiting angular size $\theta_{\rm lim}$ precisely as $24''$ (Section 3.3), one needs to vary only the limiting surface brightness $\mu_{\rm lim}$ of these models in order to put the model curves on the plot of $\mu_0(g^*)$ versus total g^* magnitude for underlying disks. The respective lines for the g band are shown in Figure 10, where we plotted them for three limiting surface brightnesses $\mu_{\rm lim}$ = 25.0, 26.0, and 26.5 mag arcsec^{-2}. As evident from the figure, both the test sample galaxies (filled diamonds) and additionally selected galaxies (crosses) define the unique model curve (as expected from the selection procedure), corresponding to the limiting surface brightness $\mu_{\rm lim}(g^*)$ = 26.5 mag arcsec^{-2}. There are no galaxies to the left of this curve. All are situated either to the right of it or fall (within the uncertainties of their parameters) right on top of this curve.

This estimated limiting surface brightness isophote for g is even slightly fainter than our previous rough estimate $\mu_{\rm lim}(g^*)$ = 26.4 mag arcsec^{-2}, but the difference between these two values is not large. Since the second estimate is a global one (i.e., it allows us to produce an estimate for all data simultaneously), we will adopt this value as the estimate of $\mu_{\rm lim}(g^*)$ hereafter. A similar analysis was performed for the r and i bands as well. The resulting threshold values are $\mu_{\rm lim}(r^*) = 26.2$ mag arcsec^{-2} for the r band and $\mu_{\rm lim}(i) = 25.9$ mag arcsec^{-2} for the i band. To compare our limiting parameters with those from previous studies we transformed $\mu_{\rm lim}(g^*)$ and $\mu_{\rm lim}(r^*)$ to $\mu_{\rm lim}(B)$ with the equations from Smith et al. (2002). Thus, our limiting surface brightnesses correspond to $\mu_{\rm lim}(B) \sim 26.9$ mag arcsec^{-2} in the standard Johnson B-band. This value is slightly deeper in comparison to the claimed value of ISIB96 $\mu_{\rm lim}(B) \sim 26$ mag arcsec^{-2}.

5.1.2. *Scale lengths*

Based on the plot in Figure 10 we can also discuss the distribution of scale lengths α of the detected galaxies. The dotted straight lines drawn in this plot show the positions of exponential disks from equation (6) with scale lengths of $\alpha = 2''$, $2\overset{\prime\prime}{.}5$, $3''$, $10''$, $30''$, and $90''$. As expected from the limiting isophotes in Figure 10, the most compact galaxies that our software should be able to detect are objects with $\alpha = 2''$, if their $\mu_0(g^*)$ is brighter than or equal to 20 mag arcsec^{-2}. However, although our sample contains galaxies with bright centers, the five most compact galaxies actually detected (both from the test sample as well as new detections) have $\alpha(g^*) \approx 2\overset{\prime\prime}{.}5$. Thus, from this rather limited sample we can infer that our programs can confidently detect disk galaxies with scale lengths $\alpha_{\rm lim}(g^*) \gtrsim 2\overset{\prime\prime}{.}5$. As one can see, most of the sample galaxies have $\alpha(g^*)$ ranging from $3''$ to $10''$. Only 11 galaxies (∼8%) have $\alpha(g^*) > 10''$. Two galaxies in the sample are found to have $\alpha(g^*) > 20''$. One of them, with $\alpha(g^*) = 23''$, is a galaxy from the test sample. So, the real fraction of extended objects in our sample is seemingly limited not by our methods, but by their presence in the test sample. The evidence for the effective detection of extended galaxies comes from the largest and the brightest galaxy in our sample – NGC 3521 with $\alpha(g^*) \approx 75''$, which was absent in the test sample.

Finally, we conclude that our software is capable to detect galaxies with scale lengths $\alpha(g^*)$ at least up to $\sim 1'$ on SDSS images. Of course, the limited size of the SDSS fields ($12' \times 10'$) begins to play a significant role in the selection procedure for such extended galaxies. However, even for such extended galaxies our programs will detect at least “the tip of iceberg” with sufficiently high probability. It is also worth noting that on the SDSS frame containing NGC 3521, whose final mask had the size of ∼1/2 of the whole frame, our programs found two more galaxies, one of which (1103+0007) exists also in the test sample. As for galaxies with $\alpha \geq 90''$ (dashed line in Figure 10) one has to work with the much larger SDSS mosaic frames (see Stoughton et al. 2002 for details) to ensure their detection.

5.1.3. *Central surface brightnesses*

The expected limiting μ_0 also can be estimated from the plot in Figure 10. It of course depends on the galaxy scale length. In particular, for galaxies with $\alpha(g^*) \geq 25''$ our software should detect galaxies as dim as $\mu_0(g^*) \geq 26.0$ mag arcsec^{-2} (which corresponds to $\mu_0(B) \geq 26.3$ mag arcsec^{-2}). Since these estimates account only for pure exponential disks, any additional light from bulge, bar, or H II regions will improve the possibility to detect such a faint disk.

The distribution of $\mu_0(g^*)$ for all studied galaxies is shown in Figure 11. All objects, both from the test sample as well as the additional detections, fall in the range of $19.5 < \mu_0(g^*) < 25.1$ mag arcsec^{-2}. Based only on the properties of these galaxies one can hardly judge the possibility to detect fainter disks with our software. However, for further analysis we can use the fact that several objects as dim as $\mu_0(g^*) = 26.0$ mag arcsec^{-2} were detected during the preliminary process of extended object identification. In the subsequent checks they were recognized as artifacts (ghosts of bright stars). Their parameters, however, indicate that if these objects were real galaxies, galaxies this faint will very likely be detected by our software. In Figure 12 we show for illustration the surface brightness profile of one of the ghost artifacts with $\mu_0(g^*) = 26.00$ mag arcsec^{-2} and $\alpha(g^*) = 24\overset{\prime\prime}{.}18$. These “disk” parameters correspond to a total magnitude of $g^*_{\rm tot} = 17\overset{\rm m}{.}08$. A real galaxy with such parameters will appear just on the border of the allowed region on diagram $\mu_0(g^*)$ versus $g^*_{\rm tot}$ in Figure 10 (star symbol).

5.1.4. *Edge-on galaxies*

It is worth noting that our selection criteria produce a bias against edge-on galaxies. Since we separate objects with the total area within the limiting isophote greater than some minimal threshold, the lower limit for their major-axis diameter of $24''$ is valid only for round, face-on galaxies. For elongated galaxies, the lower limit for this parameter varies as

$$D_{\rm lim} = \frac{24''}{\sqrt{b/a}} \qquad (14)$$

Thus, for the most elongated galaxies (b/a ∼0.1) we will detect all objects with major-axis diameter larger than $76''$.

5.1.5. *Objects with Sérsic profiles*

Since in order to describe SBPs of galaxies with general Sérsic profiles one needs one more parameter, the discussion of galaxy selection effects becomes more complicated when indices of $n > 1$ (equation 3) have to be used. We detected all galaxies of this type present in the test sample when applying our homogeneous selection criteria based on the size on the limiting isophote. They are shown in Figure 10 by open circles. However, for the same values of α and μ_0 such objects have total magnitudes fainter than objects with $n = 1$. The amount of the total flux decrease depends on value of n. For example, $F_{\rm n}/F_{\rm n=1} = 0.8$ for $n = 1.67$ and $F_{\rm n}/F_{\rm n=1} = 0.58$ for $n = 5$. Thus, $n > 1$ shifts effectively such objects to the left in Figure 10. This implies, e.g., that some of these galaxies with SBP parameters falling close to the limiting model curve with $\mu_{\rm lim}(g^*) = 26.55$ mag arcsec^{-2} will remain undetected. This will cause some additional problems for the analysis of completeness in the future survey. This issue may be properly addressed via modelling of the Sérsic profile disk detection.

5.2. *First scientific results*

Our test sample from ISIB96 was chosen to allow us to optimize our search criteria such that we are capable of retrieving known LSB galaxies. For the development of our programs and algorithms we confined ourselves to the subset of SDSS fields containing the galaxies from the test sample. These fields are non-contiguous and are drawn from a much larger area. Owing to our biased area selection we cannot draw conclusions regarding the statistical distribution and density of LSB galaxies, nor can we easily assess the overall completeness. However, the detection of numerous additional galaxies that fall in the same parameter space as the ISIB96 sample indicates that the SDSS imaging data have the potential to significantly increase the number of known LSB galaxies (see also Section 5.3). In any case, even our current, limited survey has lead to a number of interesting scientific findings, some of which will be discussed briefly below.

5.2.1. *Galaxy SDSS J140831−000737: two disks with distinct spiral structure?*

The depth and homogeneity of the SDSS imaging data allow us to study processes such as large-scale star formation in the faint outer regions of galactic disks (Ferguson et al. 1998), which have been little studied so far. For example, a galactocentric radius $R > R_{25}$ (where R_{25} is defined by the $B = 25$ mag isophote) corresponds to an isophotal level $\mu(g^*) \sim 24.6$ mag arcsec^{-2} for $(g^* - r^*) = 0\overset{m}{.}5$, and an even brighter level for redder $(g^* - r^*)$ colors. These levels are much brighter than our limiting isophotal level of $\mu(g^*) = 26.55$ mag arcsec^{-2}. The study of star formation processes in the faint outskirts of disk galaxies provides a unique insight into the nature of the star formation law, preconditions for star formation, and star formation thresholds in regions that are characterized by physical environments (such as lower metallicities and longer dynamical time scales, etc.) that are very different from those typical of the bright, inner regions of disks (see, e.g., Noguchi 2001).

An interesting galaxy offering such an opportunity is SDSS J140831−00073 (1405+0006 in ISIB96). This galaxy has an unusual structure reminiscent of the multicomponent disks mentioned by Bosma & Freeman (1993). The SBP of the disk of this galaxy is approximated best by two exponentials, corresponding to an "inner" and an "outer" disk. This galaxy was classified by ISIB96 as Sb(r). On the SDSS images, a bulge, a bar, and different spiral patterns in the "inner" disk and in the "outer" disk are clearly seen (Fig. 13). The "inner" disk is characterized by $\mu_0(B) = 21.1$ mag arcsec^{-2} and $\alpha = 1.6$ kpc. At a surface brightness of $\mu(g^*) \sim 24.5$ mag arcsec^{-2} ($R > 15''$), the "inner" spiral arms disappear. This surface brightness limit also corresponds to the apparent size of this galaxy given in previous studies, and to the outer limit of the "inner" disk. On the SDSS images we found a new subsystem of spiral arms fainter than $\mu(g^*) \sim 25.0$ mag arcsec^{-2}. The contrast-enhanced image (plotted with -1σ to 5σ, where σ is the noise of the sky background) is shown in the right panel of Figure 13. The limiting isophotal level above which this galaxy was detected corresponds to $\mu(g^*) \sim 26.55$ mag arcsec^{-2} (plotted as a solid line in Figure 13), yielding a scale length α for the "outer" disk of ~ 7 kpc. The central surface brightness for the "outer" disk is $\mu_0(B) = 24.5$ mag arcsec^{-2}. The flux ratio of the "inner" and the "outer" disk, $\mathrm{m}_{tot}^{ext.disk}/\mathrm{m}_{tot}^{int.disk}$, is approximately 1.2.

While the detailed nature of this galaxy remains uncertain at this point, we may be seeing an example of the class of galaxies with "stepped disks" described in Matthews & Gallagher (1997). It is interesting that each of the two disk components exhibits its own distinct spiral pattern. Planned long-slit spectroscopy will tell us more about the rotational properties of SDSS J140831−00073 and the metallicities of the "inner" and "outer" disks. (Impey, Burkholder & Sprayberry 2001) show that the H I profile of this system is very narrow ($\mathrm{W}_{50} = 92$ km s^{-1} and $\mathrm{W}_{20} = 112$ km s^{-1}). Matthews & Gallagher (1997) discuss the possibility that this kind of galaxy may have a very low effective viscosity, allowing outlying gas to retain its initial angular momentum. A possibly similar case is the galaxy NGC 6946 described in Ferguson et al. (1998), which also shows spiral arms in its outskirts that do not appear to be connected with its "inner" arms.

5.2.2. *Morphological types and concentration index*

Our photometric programs calculate a number of global morphological parameters for every galaxy. Some of these may be useful for morphological galaxy classifications (see earlier discussions by, e.g., Kent (1985); Kodaira, Watanabe & Okamura (1986); Fioc & Rocca-Volmerange (1999); Shimasaku et al. (2001); Strateva et al. (2001)). A particularly useful parameter is the concentration index (C hereafter), defined as the ratio of the radii containing 90% and 50% of a galaxy's light. For the classical de Vaucouleurs profile, C is ∼5.5, and for pure exponential disks, $C \sim 2.3$. These values are valid for the idealized seeing-free case, which we are approximating due to the limiting angular size $\theta_{\mathrm{lim}} \gg PSF$ that we impose in this work.

In Figure 14 the relation between the color index $(g^* - i^*)$ and the concentration index in the r-band, $\mathrm{C}(r^*)$, is plotted. We selected the color index $(g^* - i^*)$ for two reasons: (1) as a robust index from the point of view of signal to noise, and (2) since it provides a good temperature baseline considering the wavelength separation between the two bands. ISIB96 and NED list morphological classifications for the galaxies in our sample, which we revised in a number of cases based on the SDSS image material. The adopted classification is shown in column 10 of Table 1 (see Section 2). Based on this classification we divided all galaxies in our sample into following categories (barred types included) shown in Figure 14: (a) early-type spiral galaxies (S0 – Sa); (b) intermediate-type spirals (Sb – Sc); (c) late-type galaxies: Sd, Sm, and various Irr and dI; (d) dEs; and (e) interacting galaxies. We added E galaxies (open squares) in this Figure to see overall distribution of all different morphological types. The theoretical values for the concentration index for classical de Vaucouleurs profiles and for pure exponential disks are shown by dashed lines there too.

The bimodality in the distribution of galaxies noticed by Strateva et al. (2001) is clearly visible in Figure 14: Early-type galaxies are located in the parameter region $(g^* - i^*) > 0\overset{m}{.}9$ and $C(r^*) > 2.6$, and late-type galaxies are characterized by $(g^* - i^*) \leq 1\overset{m}{.}2$ and $C(r^*) < 2.6$. Intermediate-type spirals are found in both branches of the distribution. Our empirical separation at $C(r^*) = 2.6$ for these "branches" is in excellent agreement with the one found by Strateva et al. (2001), $C(r^*) = 2.63$. But using $C(r^*)$ as the only morphological separation criterion has certain drawbacks that lead to ambiguities: Additional substructure such as spiral arms and bulges in spiral galaxies or H II regions in irregular galaxies will change both C and color and often act in opposite ways. We plan to use the large sample of galaxies that will result from the application of our programs to larger areas of the SDSS (Section 5.3) to devise an improved, more detailed classification scheme.

A few more comments on Figure 14: (1) Our empirical upper limit for the concentration index is ~ 5.2, close to the theoretical value for the classical de Vaucouleurs profile ($C = 5.5$). Our upper limit differs from the value ~ 3.7 calculated based on Petrosian radii by (Shimasaku et al. 2001; Strateva et al. 2001) as given in the SDSS photometric database. This difference is caused by the method employed for the calculation of Petrosian magnitudes by the standard SDSS software (e.g., Strauss et al. (2002)), which systematically underestimates Petrosian magnitudes not only for galaxies with pure de Vaucouleurs profiles, but for all galaxies with bulges. The amplitude of this shift depends on the bulge-to-disk ratio (Strauss et al. 2002)). (2) Interacting galaxies as complex systems may be located in any part of this diagram and cannot easily be recognized. (3) Disk systems are characterized by $C(r^*) < 2.3$. Shifts to lower values of C occur when additional light from spiral arms and/or H II regions contribute. (4) Practically all dE systems are located below $C(r^*) = 2.3$ as well. This is in agreement with the theoretical expectations since most of these galaxies have SBPs with $n > 1$ (equation (3)).

The $(g^* - i^*)$ versus $C(r^*)$ contains five outliers at $(g^* - i^*) < 0\overset{\mathrm{m}}{.}9$ and $C(r^*) > 2.8$. One of them is the interacting system SDSS J133031−003613 (1327−0020). The other four galaxies have unusual morphologies: The "stepped disk" galaxy SDSS J140831−000737 ($(g^* - i^*) = 0\overset{\mathrm{m}}{.}51$ and $C(r^*) = 3.46$) was described in the previous Section 5.2.1. The galaxy SDSS J101142+003520 ($(g^* - i^*) = 0\overset{\mathrm{m}}{.}85$ and $C(r^*) = 2.92$) looks lopsided and is shown in Figure 15 (left panel). The galaxy SDSS J131215+003554 ($(g^* - i^*) = 0\overset{\mathrm{m}}{.}70$ and $C(r^*) = 3.29$) may be interacting with what appears to be a smaller galaxy seen at the extension of the tip of its western spiral arm (Figure 15, right panel). Alternatively, this seemingly smaller object may be a background galaxy. The galaxy SDSS J095939+003227 ($(g^* - i^*) = 0\overset{\mathrm{m}}{.}87$ and $C(r^*) = 3.29$) may have an outer blue disk of low surface brightness. All of these "unusual" galaxies identified in the $(g^* - i^*)$, $C(r^*)$ diagram are characterized by unusual processes in their faint outer regions and are interesting targets for future follow-up studies.

5.2.3. *Giant LSB galaxies*

An interesting aspect of this pilot study is the identification of 10 luminous distant galaxies with considerable bulge and/or bar components. The underlying disks are low-surface-brightness disks with disk scale lengths in the range of ∼7.5 to 13 kpc. These galaxies fall into the category of the so-called giant LSB galaxies, or 'cousins' of Malin 1 (Bothun et al. 1987). Sprayberry et al. (1995) define these objects as LSB galaxies that meet a "diffuseness index" criterion: $\mu_{0,\mathrm{c}} + 5 \cdot \log(\alpha) > 27.6$ (adopting a Hubble constant of $\mathrm{H}_0 = 75$ km s^{-1} Mpc^{-1}). Here $\mu_{0,\mathrm{c}}$ is the extrapolated, deprojected, and corrected for cosmological dimming B-band disk central brightness. The properties of giant LSB galaxies are summarized in the paper by Sprayberry et al. (1995). Currently, only 16 galaxies of this type are known. Their H I properties were recently studied by Matthews, van Driel, & Monnier-Ragaigne (2001).

We present a list of eleven giant LSB galaxy candidates (Table 6), which includes only one previously known galaxy of this type – 1226+0105, described by Sprayberry et al. (1995). The location of these galaxies in a plot of scale length versus central surface brightness is shown in Figure 16. As Bothun, Impey & McGaugh (1997) emphasize, giant LSB galaxies are quite enigmatic from the point of view that they normally formed their spheroidal component, but no conspicuous stellar disk ever formed around their bulge. Improved statistics for these objects will lead to a better understanding of the relationship between their fundamental parameters and the conditions/processes that led to their formation. The high detection rate of giant LSB galaxy candidates with our programs promises substantial progress for future systematic studies.

5.3. *A large LSB survey with SDSS data*

The main goal of our project is to create a big and uniform LSB sample on the base of SDSS imaging data. We plan to extend our analysis to the entire sky region from which the test sample described here was extracted, i.e., the EDR runs 752 and 756 (7272 SDSS fields) comprising $\approx$228 deg^2 (Stoughton et al. 2002). This area is 76 times larger than the total area of the sky region analyzed in the current study. This future sample will cover a sufficiently large region of the sky to provide us with better statistics and to decrease the effects caused by large-scale fluctuations of galaxy density.

We plan to use our final sample to conduct a thorough study of the properties of LSB galaxies, including the analysis of their luminosity function. We will also investigate the space density of galaxies as a function of central surface brightness, for which we will need to create a volume-limited sample. This implies that we need redshifts for all our selected galaxies from the whole region of the two EDR runs. In this sense, the selection threshold on total magnitude of about $r = 18\overset{\mathrm{m}}{.}0$, which we derive from the estimations performed using Figure 10, looks very promising. It is rather close to the SDSS galaxy spectroscopy threshold magnitude of $r = 17\overset{\mathrm{m}}{.}77$. Accounting for the 2dF redshift survey information already available in the discussed region (Colless et al. 2001), we expect that only for a small fraction of the detected LSB galaxies we will need additional redshift determinations.

6. SUMMARY AND CONCLUSIONS

In this paper we pursued the goal to develop an effective method to search for LSB and dwarf galaxies in the SDSS image database based on a test sample from the galaxy catalog of ISIB96. We developed our own programs to search for galaxies with large angular sizes from SDSS images. The reliability of these programs was carefully tested using a training subsample of galaxies from the catalog of ISIB96. This allowed us to choose our selection criteria such that we achieved very high efficiency in recovering galaxies from the test sample, limited only by cases when a candidate galaxy falls too close to a very bright star or galaxy. The dimmest LSB galaxy from the test sample detected so far has $\mu_0(B) \sim 25$ arcsec^{-2}. Based on the tests discussed in the previous sections, we estimate our detection limits to be $\mu_0(g^*) = 26\overset{\mathrm{m}}{.}0 - 26\overset{\mathrm{m}}{.}5$ arcsec^{-2}, which will need to be verified in our planned studies. Furthermore, our new method, which applies predefined objective selection criteria, resulted in the detection of 42 (47%) additional galaxies with similar parameters within the test fields.

A continuation of this work is planned within a region with a 76 times larger area. On the one hand, this will allow us to refine the determination of the detection limit of our method, and on the other hand is expected to create a new sample of $\sim 10^3$ galaxies.

Based on the work described in our current paper, the following conclusions can be drawn:

1. Dealing directly with the SDSS catalog database parameters, we found it difficult to reliably identify LSB galaxies. To overcome these difficulties we developed our own method, which we plan to apply to the entire SDSS imaging data. A program package intended to search for galaxies with large angular size was created and carefully tested, and is described in the present paper in detail. These programs allowed us to find 87 of a training set of 90 galaxies from the Impey et al. (1996) catalog, distributed over 93 SDSS fields. That is, the efficiency of the method is ~96.5%. Our new software also resulted in the discovery of 42 additional galaxies in the same SDSS fields, whose parameters are similar to those of the test sample objects.

2. We also created programs that produce independent photometry of all selected galaxies within the studied SDSS images. The comparison of our photometry for galaxies found twice in overlapping fields of the same SDSS run shows good repeatability. All differences are within 1–3σ of the photometric uncertainties, indicating that our programs are very robust. We compared our photometry with published data in various bands for several galaxies in common. This shows the external consistency of our magnitudes to be within $\sim 0\overset{\mathrm{m}}{.}1$ for different bands. We demonstrate that our programs allow us to obtain accurate photometry for galaxies as bright as B=$10\overset{\mathrm{m}}{.}0$ from SDSS images.

3. The results of this study show that the SDSS images can be efficiently used to search for LSB galaxies down to at least $\mu_0(g^*) \sim 25.0$ mag arcsec^{-2}. Our software has been shown to be sensitive to galaxies with scale lengths α in the range between $2\overset{\prime\prime}{.}5$ and $75''$and with central surface brightness $\mu_0(g^*)$ in the range between 19.5 and 26.0 mag arcsec^{-2}; it may work fine over an even larger range.

4. The results obtained for the test sample also demonstrate the potential of the SDSS imaging data for the study of unusual LSB galaxies:
    - We found a galaxy (SDSS J140831−000737) with a “stepped disk” structure that looks like two exponential disks, an “inner” and an “outer” one, akin to galaxies described in Matthews & Gallagher (1997). Both disks show their own distinct spiral pattern.
    - We showed that galaxies with unusual faint outer structure may be found on the base of a color ($g^* - r^*$) vs. concentration index $C(r^*)$ diagram. We confirm the usefulness of this diagram for crude morphological galaxy classifications.
    - We found ten new giant LSB galaxy candidates in addition to the 15 previously known giant LSB galaxies or Malin 1-like objects, underlining the potential of the SDSS for the study of these enigmatic LSB objects.

In subsequent papers, we will explore the selection function of our galaxy sample, luminosity functions, and the detailed properties of our galaxies and of their environment. Also, we will continue our survey for LSB galaxies using SDSS data and targeted follow-up observations. Our studies will help to improve the census of volume-selected LSB galaxies and of their evolutionary status.

S.A.P. and A.G.P. acknowledge financial support and hospitality of MPIA during part of this work. The authors are grateful to the referee for the useful questions and suggestions which helped to improve the paper presentation.

Funding for the creation and distribution of the SDSS Archive has been provided by the Alfred P. Sloan Foundation, the Participating Institutions, the National Aeronautics and Space Administration, the National Science Foundation, the U.S. Department of Energy, the Japanese Monbukagakusho, and the Max Planck Society. The SDSS Web site is http://www.sdss.org/.

The SDSS is managed by the Astrophysical Research Consortium (ARC) for the Participating Institutions. The Participating Institutions are The University of Chicago, Fermilab, the Institute for Advanced Study, the Japan Participation Group, The Johns Hopkins University, Los Alamos National Laboratory, the Max-Planck-Institute for Astronomy (MPIA), the Max-Planck-Institute for Astrophysics (MPA), New Mexico State University, University of Pittsburgh, Princeton University, the United States Naval Observatory, and the University of Washington.

This work is based in part on observations in the framework of the “Calar Alto Key Project for SDSS Follow-up Observations” (Grebel 2001) obtained at the German-Spanish Astronomical Centre, Calar Alto Observatory, operated by the Max Planck Institute for Astronomy, Heidelberg, jointly with the Spanish National Commission for Astronomy.

This research has made use of the NASA/IPAC Extragalactic Database (NED) which is operated by the Jet Propulsion Laboratory, California Institute of Technology, under contract with the National Aeronautics and Space Administration.

REFERENCES

Abazajian et al. 2003, AJ, 126, 2081

Allen, R.J., & Shu, F.H. 1979, ApJ, 277, 67

Andredakis, Y.C., Peletier, R.F., & Balcells, M. 1995, MNRAS, 275, 874

Andredakis, Y.C., & Sanders, R.H. 1994, MNRAS, 267, 283

Armandroff, T.E., Davies, J.E., & Jacoby G.H. 1998, AJ, 116, 2287

Armandroff, T.E., Jacoby, G.H., & Davies, J.E. 1999, AJ, 118, 1220

Beijersbergen, M., de Block, W., & van der Hulst, J. 1999, A&A, 351, 903

Bosma, A., & Freeman, K.C. 1993, AJ, 106, 1394

Bremnes, T., Binggeli, B., & Prugniel, P. 1999, A&AS, 137, 337

Bothun, G.D., Beers, T., Mould, J.R., & Huchra, J. 1985, AJ, 90, 2847

Bothun, G.D., Impey, C.D., Malin, D.F., & Mould, J.R. 1987, AJ, 94, 23

Bothun, G., Impey, C., & McGaugh, S. 1997, PASP, 109, 745

Blanton, M.R., Dalcanton, J., Eisenstein, D. et al. 2001, AJ, 121, 2358

Burkholder, V., Impey, C., & Sprayberry D. 2001, AJ, 122, 2318

Colless, M., Dalton, G., Maddox, S. et al. 2001, MNRAS, 328, 1039

Cross, N., & Driver, S. 2002, MNRAS, 329, 579

Dalcanton, J.J., Spergel, D.N., Gunn, J.E., Smith, M., & Schneider, D.P. 1997, AJ, 114, 635

Dalcanton, J.J. 1998, ApJ, 495, 251

de Vaucouleurs, G. 1953, MNRAS, 113, 134

de Vaucouleurs, G., de Vaucouleurs, A., Corwin, H.G., Buta, R., Paturel, G., & Fouqué, P. 1991, Third Reference Catalog of Bright Galaxies (New York: Springer-Verlag)

Ferguson, A.M.N., Wyse, R.F.G., Gallagher, J.S., & Hunter, D.A. 1998, ApJ, 506, L19

Fioc, M., & Rocca-Volmerange, B. 1999, å, 351, 869

Fischer, P., McKay, T.A., Sheldon, E. et al. 2000, AJ, 120, 1198

Freeman, K.C. 1970, ApJ, 160, 811

Fukugita, M., Ichikawa, T., Gunn, J.E., et al. 1996, AJ, 111, 1748

Grebel, E. K. 2001, Reviews in Modern Astronomy, 14, 223

Grebel, E. K., & Guhathakurta, P. 1999, ApJ, 511, L101

Gunn, J.E., Carr, M.A., Rockosi, C.M., Sekiguchi, M., et al. 1998, AJ, 116, 3040

Impey, C.D., Bothun, G.D., & Malin, D. 1988, ApJ, 330, 634

Impey, C.D., Sprayberry D., Irwin, M.J., & Bothun, G.D. 1996, ApJS, 105, 209 (ISIB96)

Impey, C.D., & Bothun, G.D. 1997, ARA&A, 35, 267

Impey, C.D., Burkholder, V., & Sprayberry, D. 2001, AJ, 122, 2341

Irwin, M.J., Davies, J.I., Disney, M.J., & Phillips, S. 1990, MNRAS, 245, 289

Jerjen, H., Binggeli, B., & Freeman, K.C. 2000, AJ, 119, 593

Karachentseva, V.E. & Karachentsev, I.D. 1998, A&AS, 127, 409

Kent, S.M. 1985, ApJS, 59, 115

King, I.R. 1966, AJ, 71, 64

Kniazev, A.Y., Salzer, J., Lipovetsky, V.A., et al. 1997, Newsletter of the Working Group on Wide Field Imaging, IAU Commission 9, 9, 5

Kniazev, A.Y., Salzer, J., Lipovetsky, V.A., et al. 1998, in IAU Symp. 179, New Horizons from Multi-Wavelength Sky Surveys, ed. B.J.McLean, D.A. Golombek, J.J.E. Hayes, & H.E. Payne (Dordrecht: Kluwer), 302

Kniazev, A.Y. 1997, Ph.D. Thesis, Special Astrophys. Obs., Nizhnij Arkhyz (http://precise.sao.ru)

Knox, R.A., Hambly, N.C., Hawkins, M.R.S., & MacGillivray, H.T. 1998, MNRAS, 297, 839

Kodaira, K., Watanabe, M., & Okamura, S. 1986, ApJS, 62, 703

Kormendy, J., 1977, ApJ, 217, 406

Korn, G.A., & Korn, T.M. 1961, Mathematical Handbook for Scientists and Engineers, McGraw-Hill

Lorenz, H., Richter, G.M., Capaccioli, M., & Longo G 1993, A&A, 277, 321

Lupton, R.H., Gunn, J.E., Ivezić, Z., Knapp, G.R., Kent,S., & Yasuda, N. 2001, Astronomical Data Analysis Software and Systems X, ASP Conf. Proc. Vol. 238, eds. F. R. Harnden, Jr., F. A. Primini, & H. E. Payne (San Francisco: ASP), 269

MacArthur, L.A., Courteau, S., & Holtzman, J.A. 2003, AJ, 582, 689

Matthews, L.D., & Gallagher, J.S. 1997, AJ, 114, 1899

Matthews, L.D., van Driel, W., & Monnier-Ragaigne, D. 2001, A&A, 365, 1

McKay, T. A. et al. 2002, ApJ, 571, L85

MIDAS Users Guide, 1995, Volume A

McGaugh, S.S. 1996, MNRAS, 280, 337

Noguchi, M. 2001, ApJ, 555, 289

O'Neil, K., Bothun, G. D., Schombert, J., Cornell, M. E., & Impey, C. D. 1997a, AJ, 114, 2448

O'Neil, K., Bothun, G.D., & Cornell, M.E. 1997b, AJ, 113, 1212

Ostriker, J. 1993, ARA&A, 31, 589

Patat, F. 2003, A&A, 401, 797

Peebles, P.J.E. 2001, ApJ, 557, 495

Richter, G.M. 1978, Astronomische Nachrichten, 299, 331

Salzer, J.J., MacAlpine, G.M., & Boroson, T.A. 1989, ApJS, 70, 447

Salzer, J.J., Gronwall, C., Lipovetsky, V.A., Kniazev, A., Moody, J.W., et al. 2000, AJ, 120, 80

Sérsic, J.L. 1968, Atlas de Galaxes Australes (Cordoba, Argentina: Observatorio Astronomico)

Shergin, V.S., Kniazev, A.Yu., & Lipovetsky, V.A. 1996, Astronomische Nachrichten, 2, 95

Shergin, V.S. 1997, private communication

Shimasaku, K., Fukugita, M., Doi, M. et al. 2001, AJ, 122, 1238

Smith, J.A., Tucker, D.L., Kent, S. et al. 2002, AJ, 123, 2121

Sprayberry, D., Impey, C.D., Bothun, G.D., & Irwin, M.J. 1995, AJ, 109, 558

Sprayberry, D., Impey, C.D., & Irwin, M.J. 1996, ApJ, 463, 535

Stoughton, C., Lupton, R.H., Bernardi, M. et al. 2001, AJ, 123, 485

Strateva, I., Ivezić, Z., Knapp, G.R., et al. 2001, AJ, 122, 1861

Strauss, M.A., Weinberg, D.H., Lupton, R.H., et al. 2002, AJ, 124, 1810

Trentham, N. & Tully, R. B. 2002, MNRAS, 335, 712

van Zee, L., Haynes, M. P., Salzer, J. J., & Broeils, A. H. 1997, AJ, 113, 1618

Vennik, J., Hopp, U., Kovachev, B., Kuhn, B,. & Elsasser, H. 1996, A&AS, 117, 261

Vennik, J., Hopp, U., & Popescu, C. 2000, A&AS, 142, 399

Whiting, A.B., Hau, G.K.T., & Irwin, M. 1999, ApJ, 118, 2767

Yasuda, N., Fukugita, M., Narayanan, V.K. et al. 2001, AJ, 122, 1104

York, D.G., Adelman, J., Anderson, J.E. et al. 2000, AJ, 120, 1579

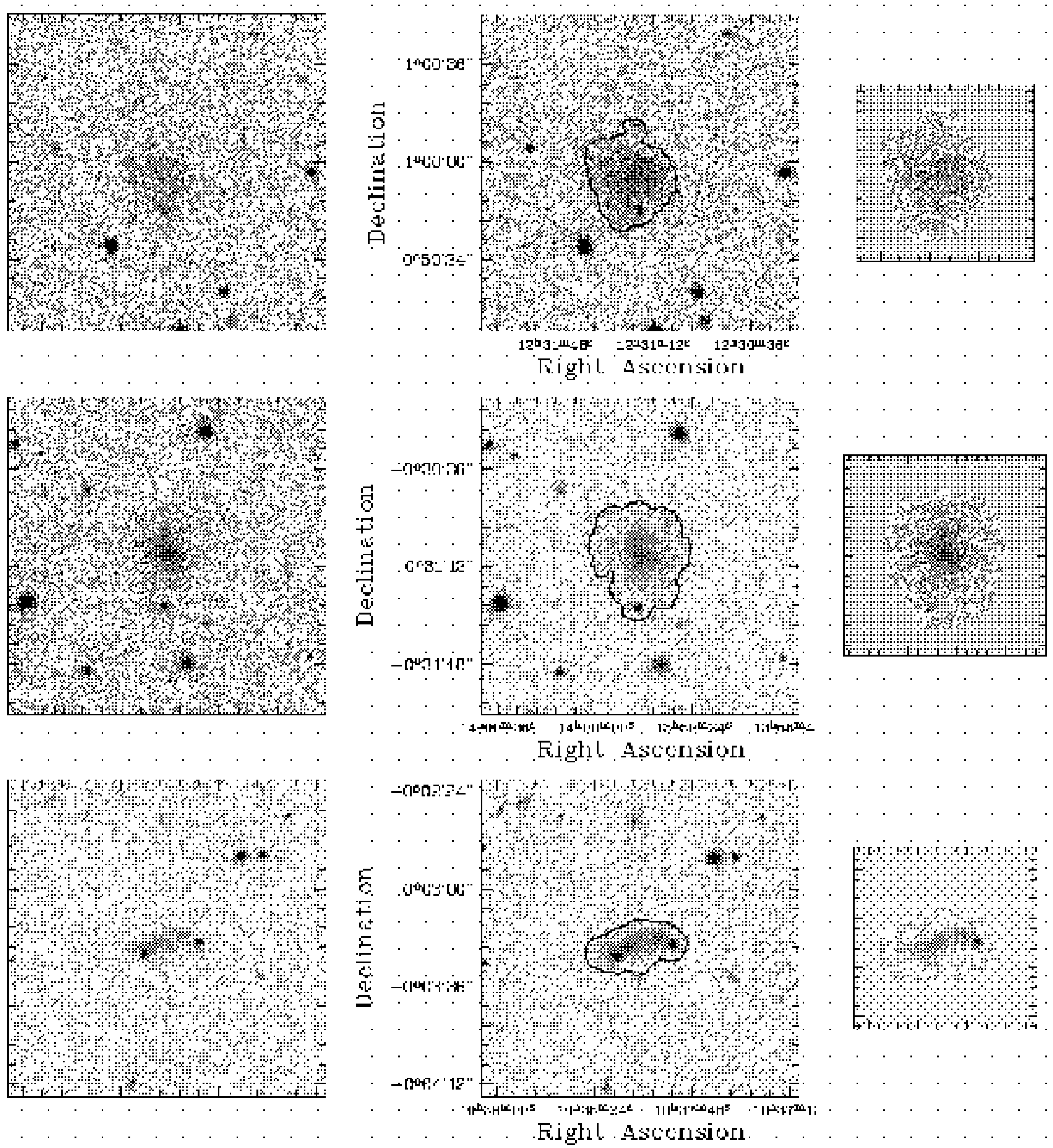

FIG. 1.— Direct images of two galaxies from the ISIB96 test sample, SDSS J123116+005939 and SDSS J135943−003133, and of one additional galaxy, SDSS J103806−000319, which was detected in the same fields. All of these galaxies were detected as objects with R≥12″ only after applying the filtering procedure. Three images are shown for each galaxy. *Left panels:* SDSS r-band images with the target galaxy in the center, *Middle panels:* A combined g, r, and i image with a superimposed isophote corresponding to the threshold level of the selection criterion, *Right panels:* r-band extracted subimage, which is then stored in the temporary work database and prepared for integrated photometry, i.e., with background/foreground sources and sky have been subtracted. All images have the same scale, and each object is plotted with the same relative low and high intensity threshold values, -3σ to $+15\sigma$. The images in the left and middle panels have sizes of 117″×117″. The image sizes in the right panels differ from the former since they depend on the mask sizes.

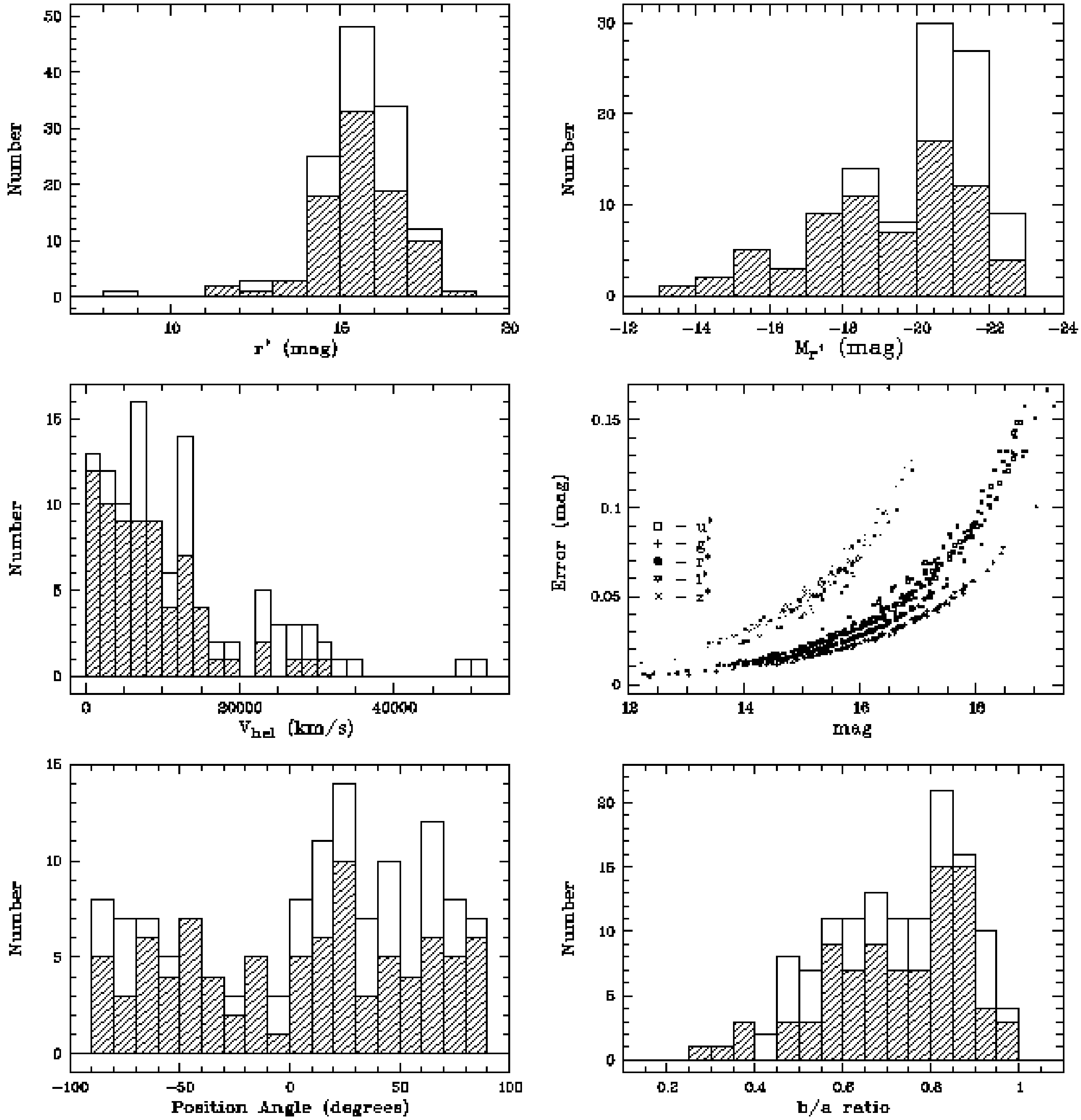

FIG. 2.— The distributions of the apparent r^* magnitudes (top-left), of the absolute M_{r^*} magnitudes uncorrected for Galactic foreground extinction (top-right), the heliocentric velocities (middle-left), the calculated instrumental uncertainties of the integrated magnitudes for various SDSS filters (middle-right), the position angles (bottom-left), and the axis ratios (bottom-right) for all galaxies detected in the 93 test fields with our programs. The galaxies from ISIB96 are shown with hashed bins.

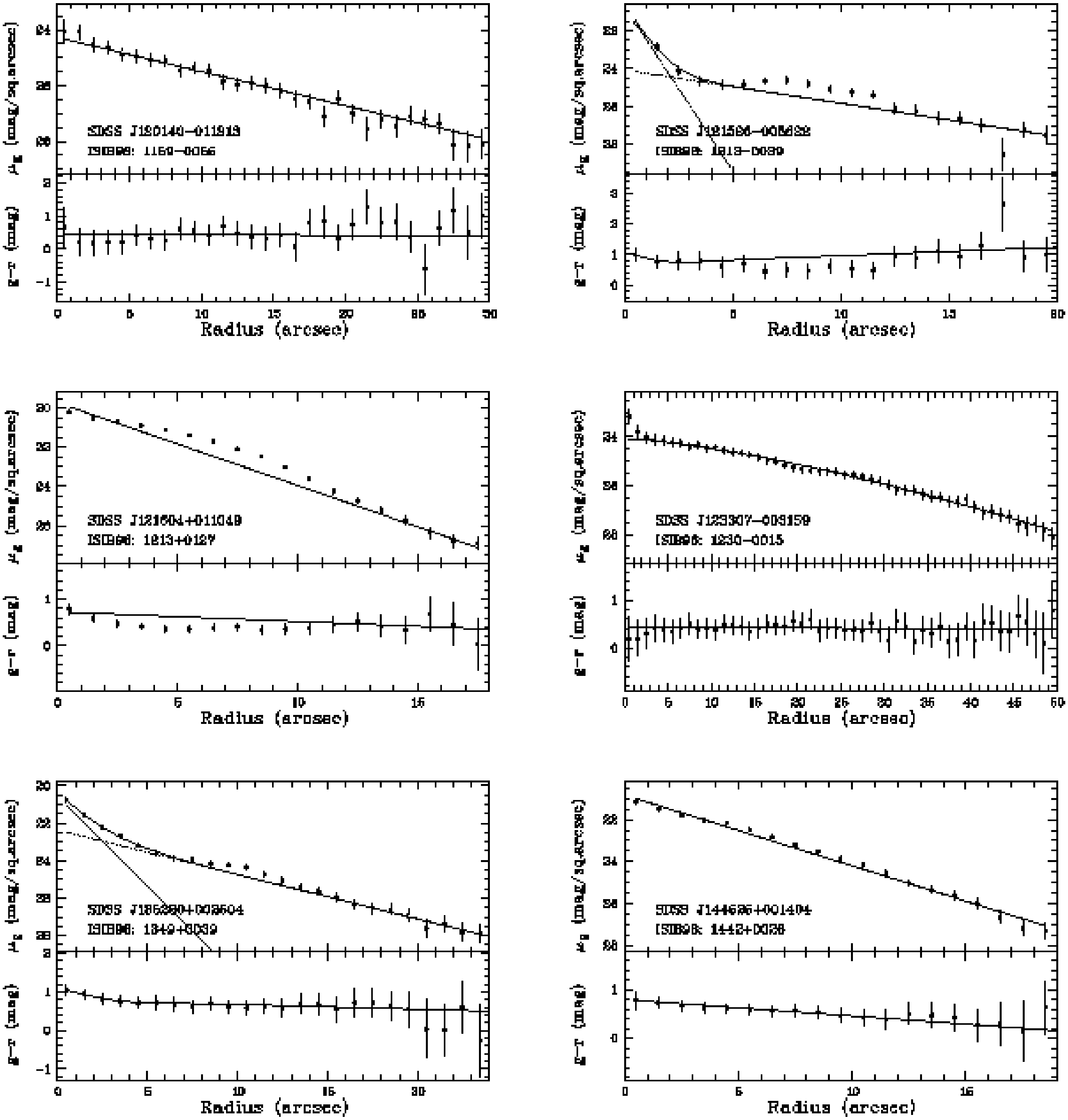

FIG. 3.— The SDSS g-band SBPs and $(g^* - r^*)$ color radial profiles for six of the galaxies from the test sample. Three kinds of profiles are shown: pure exponential (1159−0055, 1213+0127, 1442+0026), disk and bulge (1212−0039 and 1349+0039), and Sérsic profiles (1230−0015). The different lines in the SBPs panels show the model fit distributions to the data, including bulge (if any), disk, and the total light. The lines in the $(g^* - r^*)$ color panels show the model $(g^* - r^*)$ color distributions derived as the difference between the model g^* and r^* distributions.

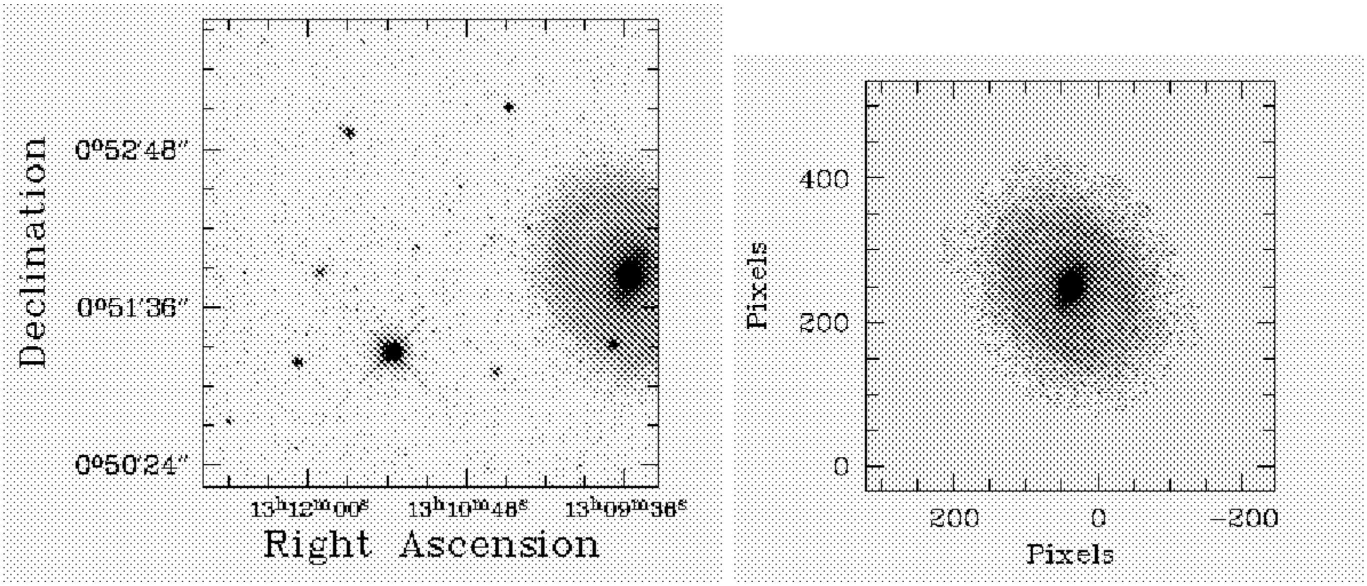

Fig. 4.— Galaxy NGC 4996 (J130931+005125), detected as an additional, non-ISIB96 object in one of the fields of the test sample. The galaxy (as seen in the SDSS field) is shown in the left panel. It is truncated by the field border. In order to "restore" the truncated part, we assumed point symmetry. The resulting "restored" image is shown in the right panel. The difference between the magnitude calculated within the original mask and the one calculated for the "restored" image is $\Delta m(g^*) = 0\overset{m}{.}22$.

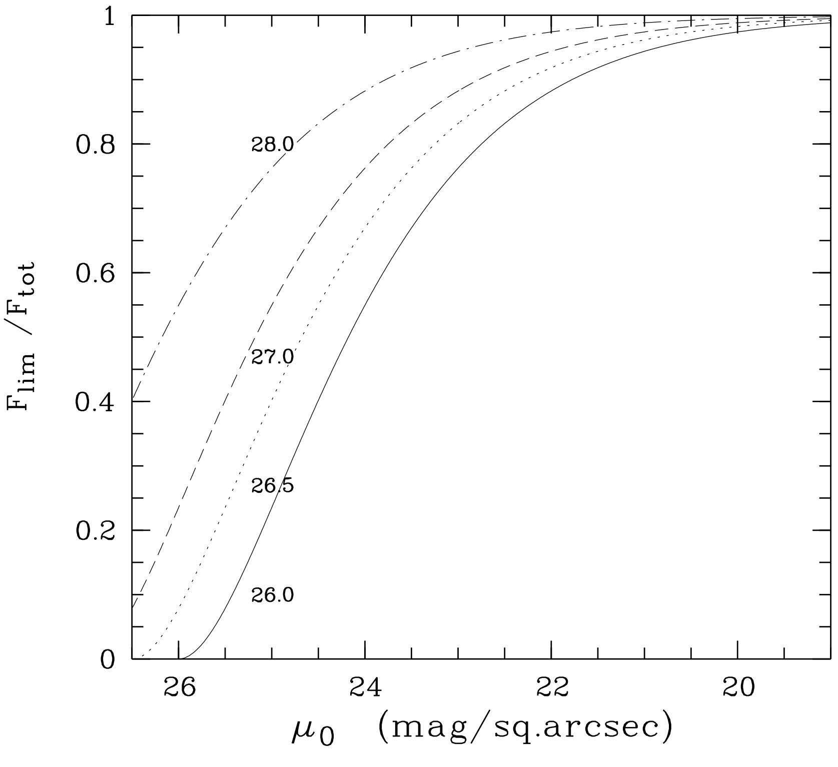

Fig. 5.— Filter-independent ratio $F_{\rm obs}/F_{\rm tot}$ of the total galaxy flux to that observed within the limiting surface brightness $\mu_{\rm lim}$ versus the central surface brightness μ_0.

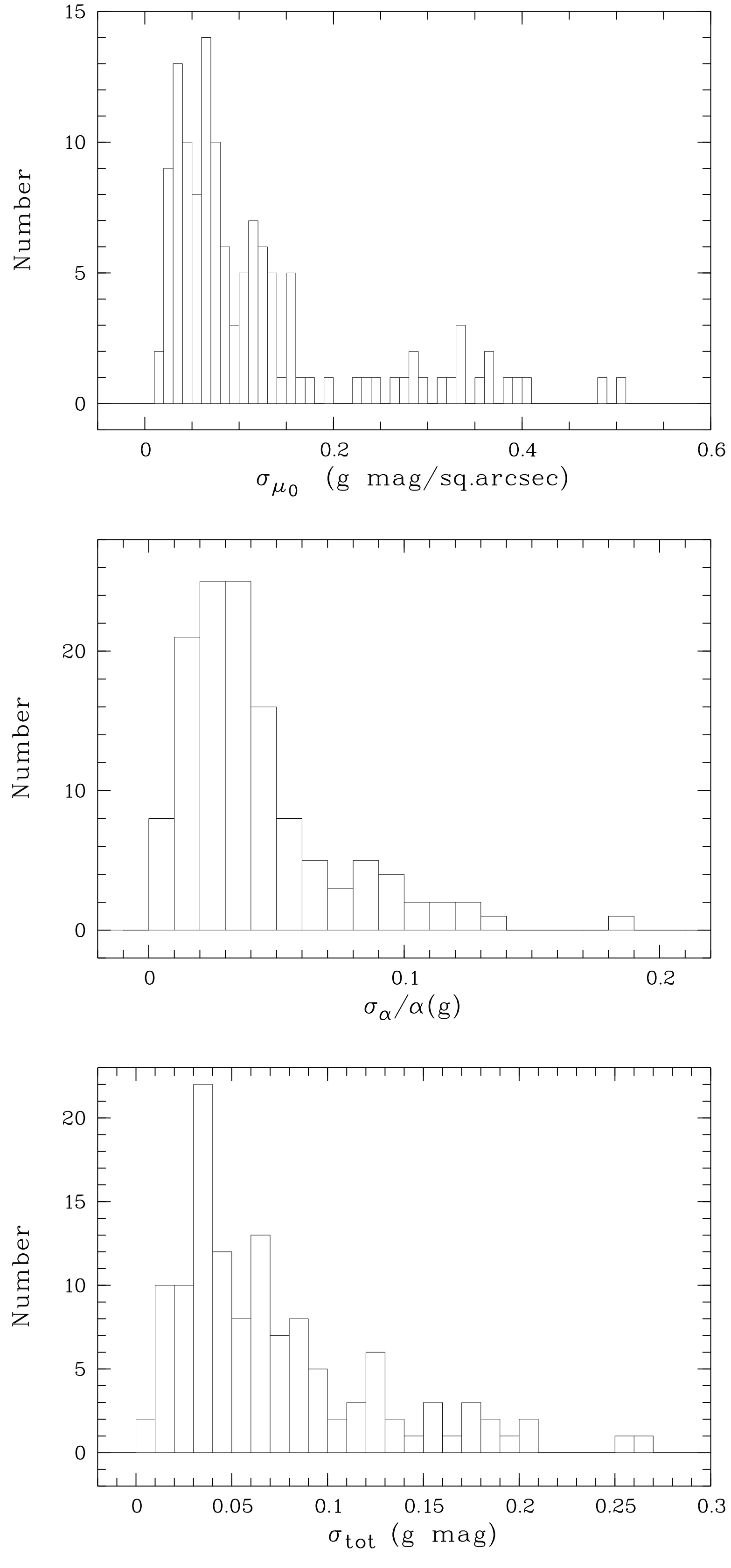

FIG. 6.— The distributions of the errors of the exponential fitting parameters μ_0 and α for the galaxies of our sample in the g-band (top and middle panels, respectively) and the distribution of the uncertainties in their g-band total magnitude (bottom panel), derived with the procedure outlined in Section 3.8.

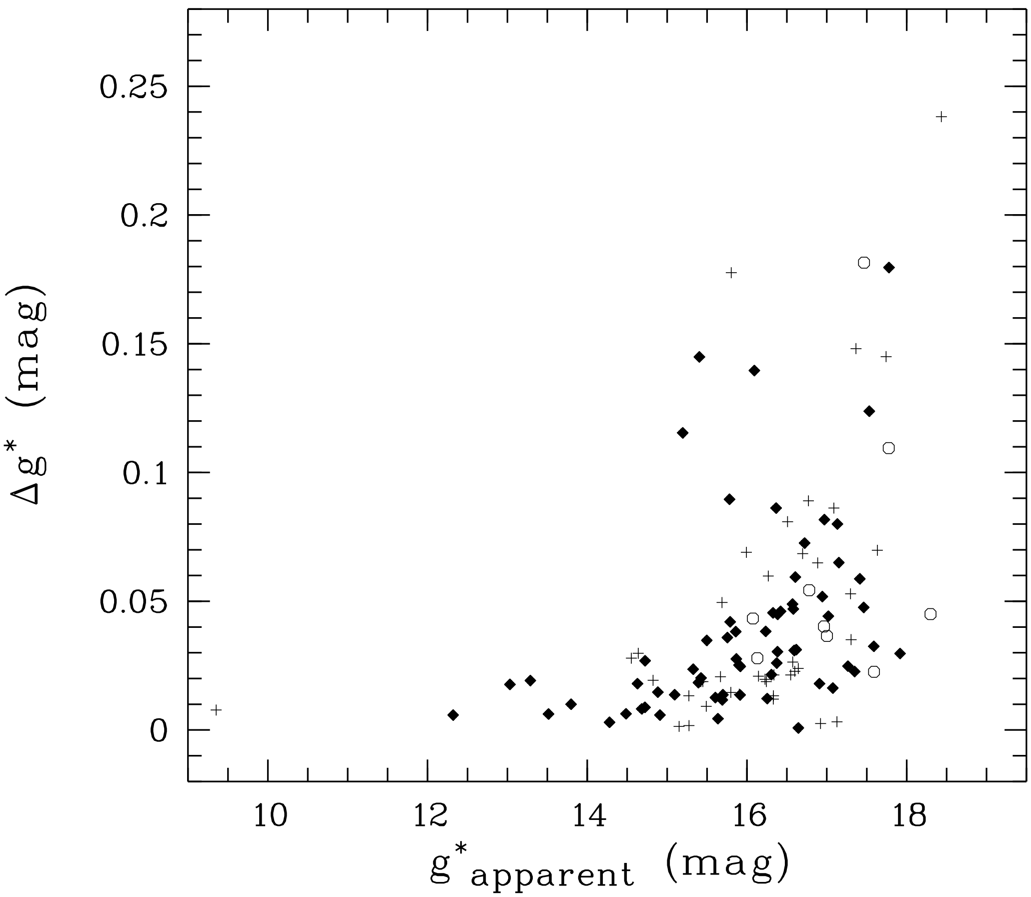

FIG. 7.— The difference between the apparent and the total *g*-band magnitudes versus the apparent magnitude for our sample galaxies. The different symbols are the same as in Figure 5 and denote the type of SBP fitting.

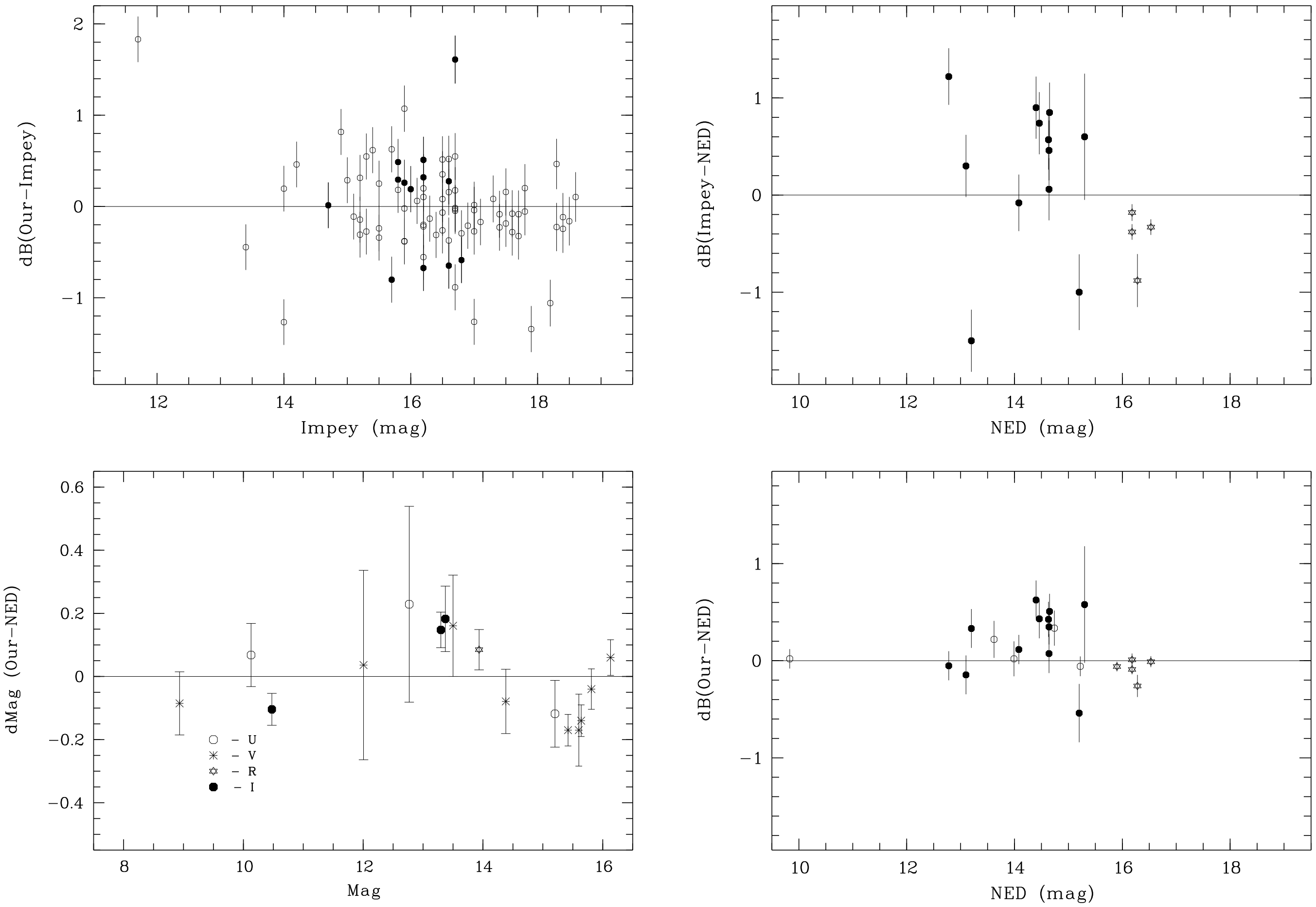

FIG. 8.— Comparison of our photometry (transformed to $UBVR_cI_c$ magnitudes using the equations from Smith et al. (2002)) with $B_{\rm tot}$ from ISIB96 and with magnitudes for several bright galaxies retrieved from NED. *Top-left panel:* The difference ΔB(Our−Impey) versus $B_{\rm tot}$ from ISIB96. The filled circles denote galaxies that, according to ISIB96, had CCD photometry as opposed to have been measured on photographic plates. *Top-right panel:* ΔB(Impey−NED) versus B(NED). The filled circles show all galaxies in ISIB96 and NED in common. The comparison of ISIB96 photometry with the magnitudes from Salzer, MacAlpine & Boroson (1989) is shown with asterisks. *Bottom-left panel:* Comparison of our photometry (transformed to UVR_cI_c) with the magnitudes from NED. *Bottom-right panel:* ΔB(Our−NED) versus B(NED). The galaxies from ISIB96 are shown by filled circles, while the additional galaxies that we found in the test sample fields are shown by open circles. The comparison of our photometry with the magnitudes from Salzer, MacAlpine & Boroson (1989) is shown with asterisks.

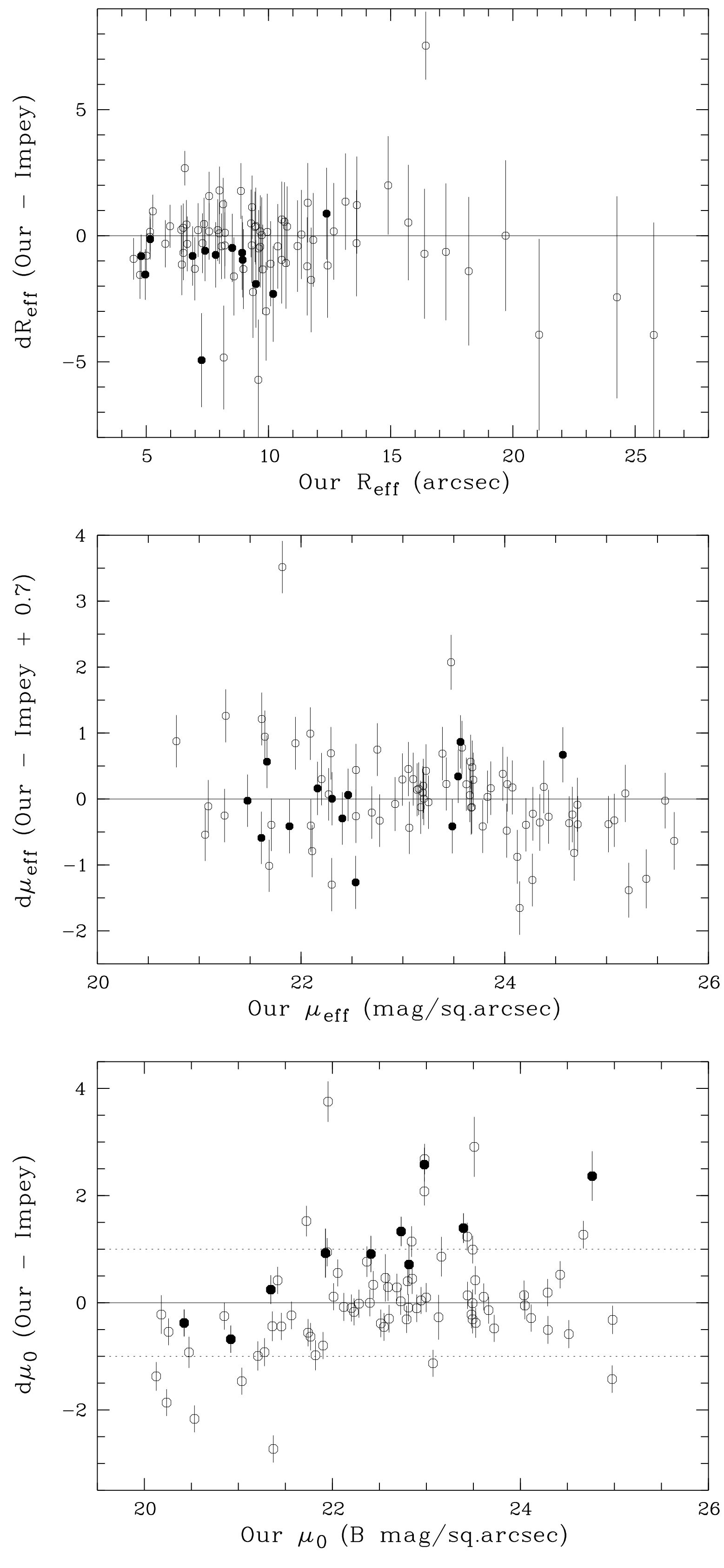

FIG. 9.— Comparison of our structural parameters $R_{eff}(g^*)$, μ_{eff}, and μ_0 with those from ISIB96 for the test sample galaxies. Our original g and r-band μ_{eff} and μ_0 were transformed to B-band magnitudes. The error bars corresponding to the total r.m.s. uncertainties of shown differences. Filled circles denote galaxies that according to ISIB96 had parameters derived from CCD photometry (as opposed to photographic plates).

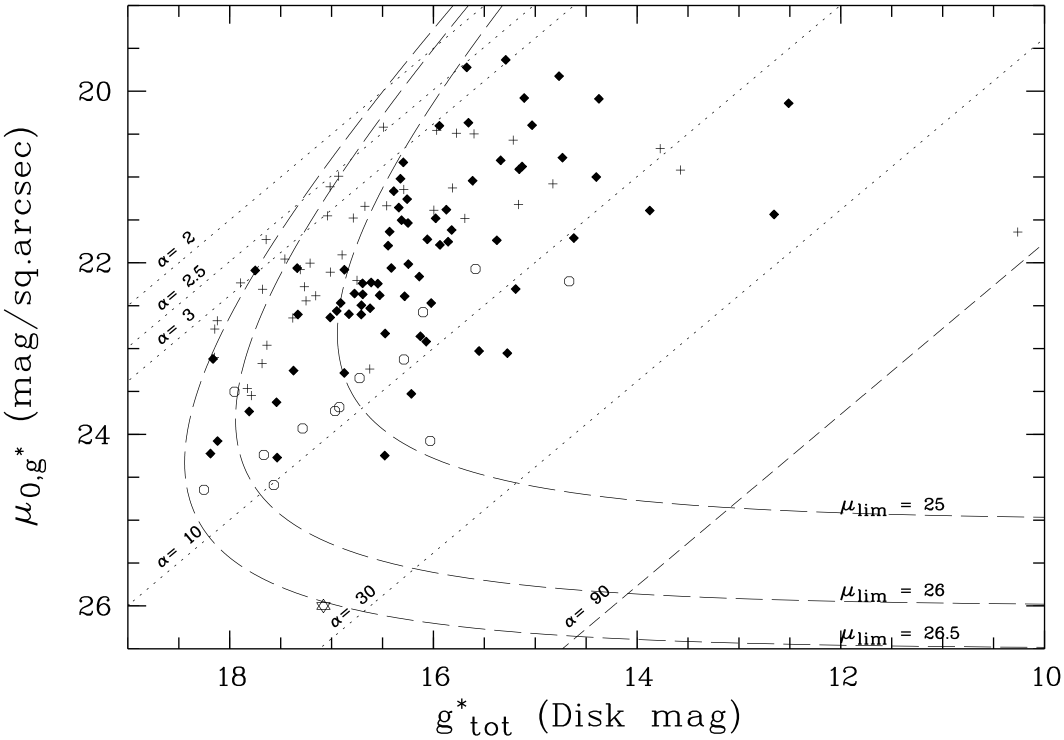

FIG. 10.— The total disk g^*-magnitude versus the central surface brightness μ_0 for all detected galaxies. The long-dashed curves are the envelopes of the selection function defined by the limiting isophotes $\mu_{\rm lim}$ labelled in the legend and the limiting angular size at those isophotes, $\theta_{\rm lim} = 24''$. They were calculated using equation 13. Isolines (dotted) with constant scalelength α are overplotted as well. Filled diamonds denote the galaxies from the ISIB96 test sample. Open circles mark the galaxies from this test sample with Sérsic SBPs ($n > 1$). Crosses show the additional galaxies found in the SDSS fields with the same selection criteria as used to retrieve the test sample. The star symbol at $g^*_{\rm tot} \approx 17\overset{\rm m}{.}0$ shows the location of the faintest ghost image detected with our software.

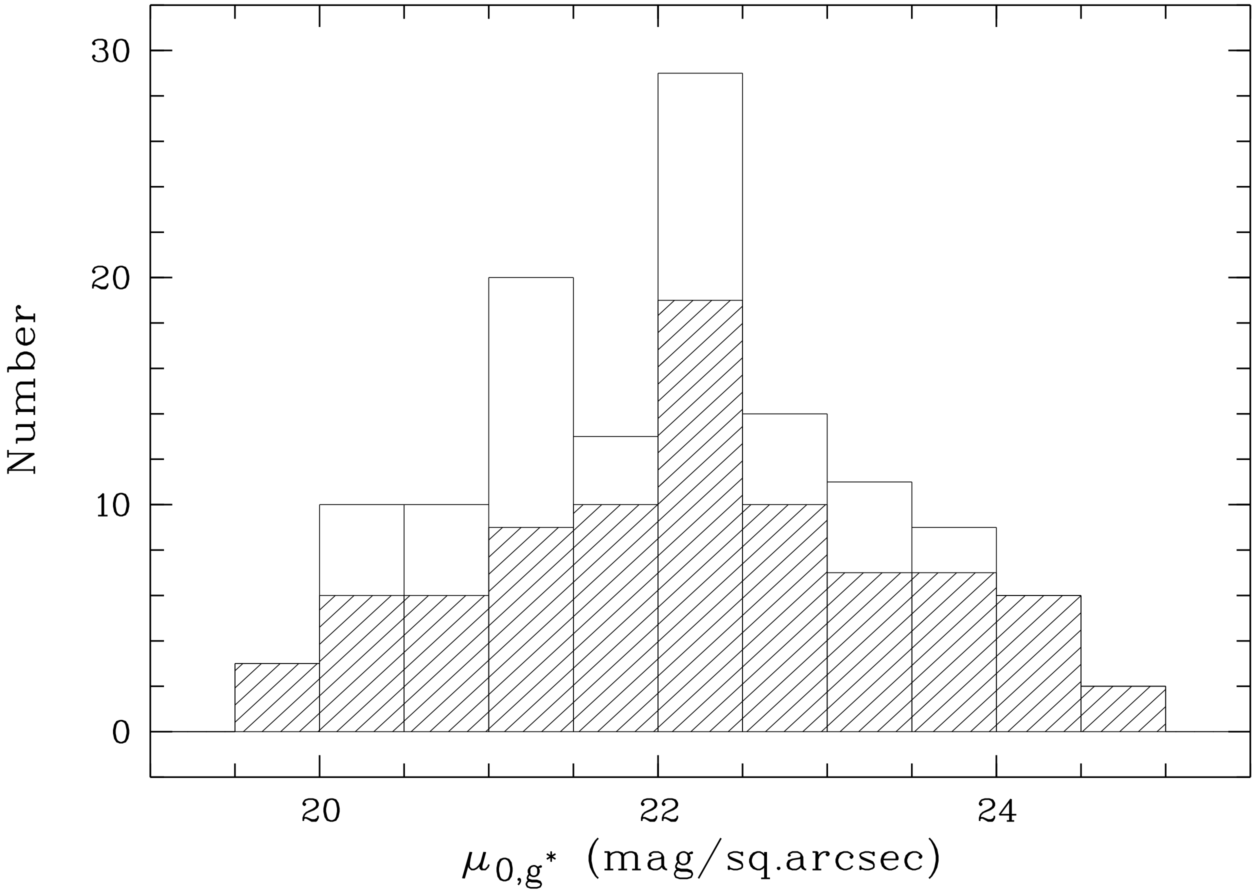

Fig. 11.— The histogram of the observed central surface brightnesses $\mu_0(g^*)$. The galaxies from ISIB96 are shown as hashed bins.

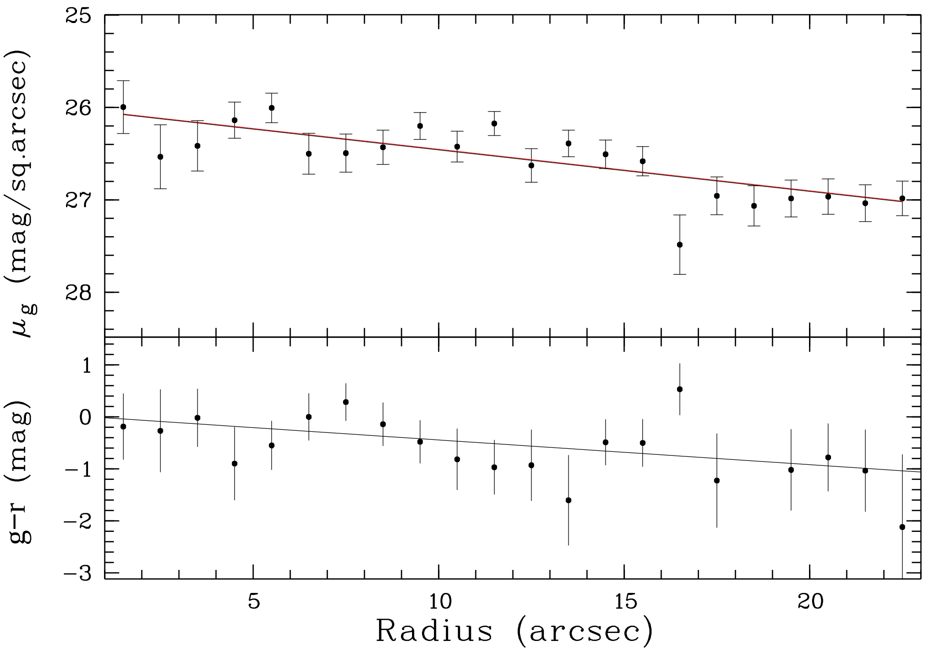

FIG. 12.— The SBP in the g-band, and the $(g^* - r^*)$ radial profile of the faintest ghost image detected by our programs in one of the test sample fields.

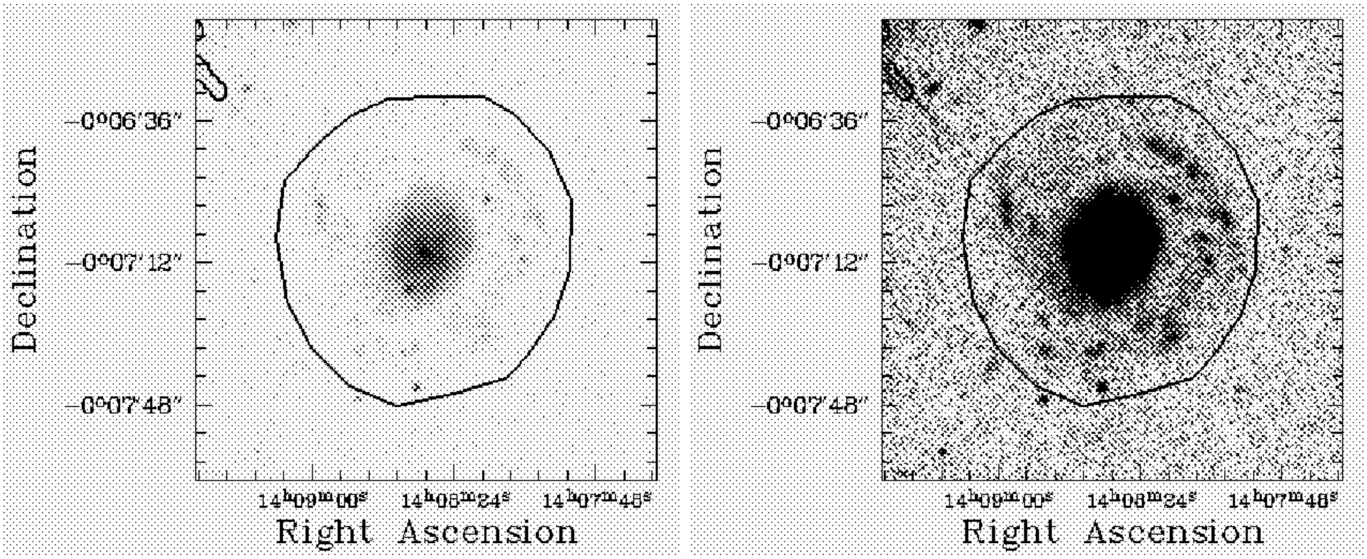

FIG. 13.— Two presentations of galaxy SDSS J140831−000737 to highlight its unusual structure. *Left panel:* A combined SDSS g, r, i image with the isophotal selection level superimposed. This image is plotted with relative low and high intensity levels of -1σ and 100σ, respectively. Spiral arms in the central, "inner" disk are clearly recognizable on the combined image, as are bulge and bar-like structures. *Right panel:* The same image is plotted, but with relative low and high intensity values of -1σ and 5σ. Patchy outer spiral arms can be clearly seen at this level of contrast. Previous studies missed the "outer disk" visible in the SDSS data and detected only the inner portion of this galaxy.

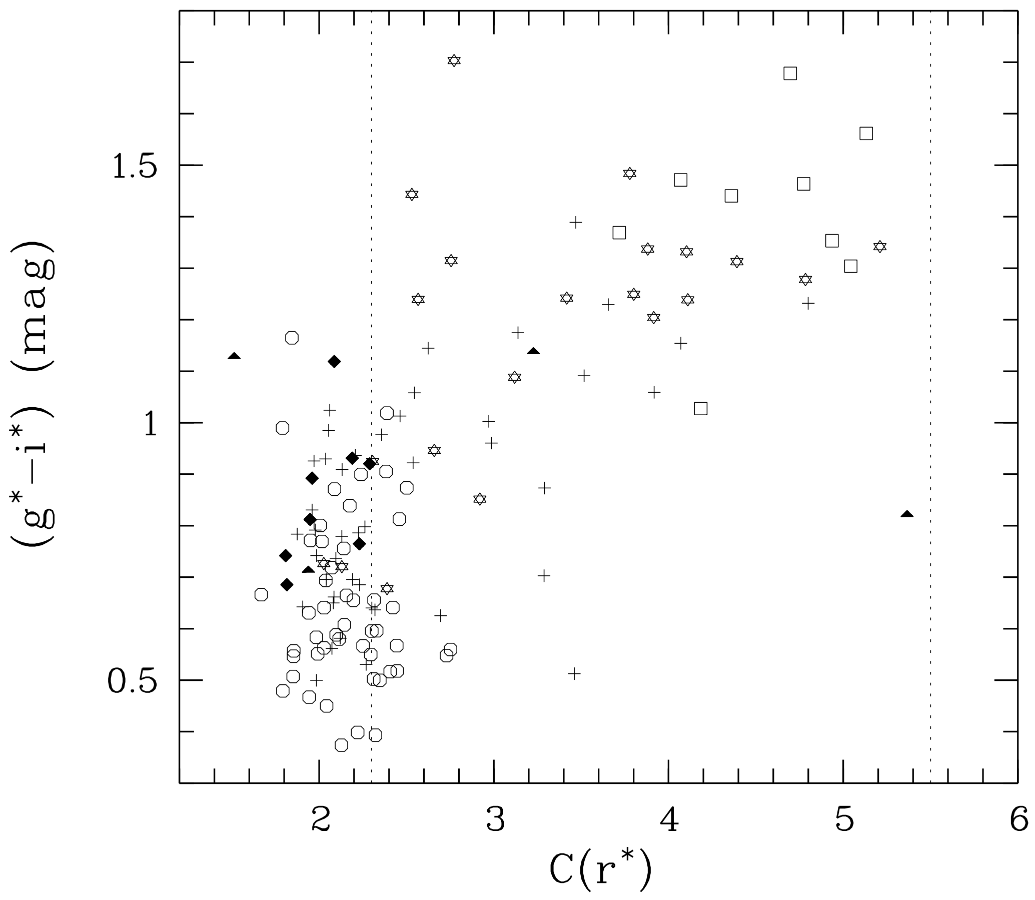

FIG. 14.— The relation between the color index $(g^* - i^*)$ and the concentration index in the r^*-band, $C(r^*)$. Open squares denote E galaxies. Asterisks denote early-type galaxies (S0 – Sa). Crosses indicate galaxies of “intermediate” type (Sb – Sc). Open circles stand for late-type galaxies (Sd – Irr and dI). Filled lozenges denote dEs. Filled triangles denote interacting galaxies. The values of the concentration index for classical de Vaucouleurs profiles (5.5) and for pure exponential disks (2.3) are shown by dashed lines.

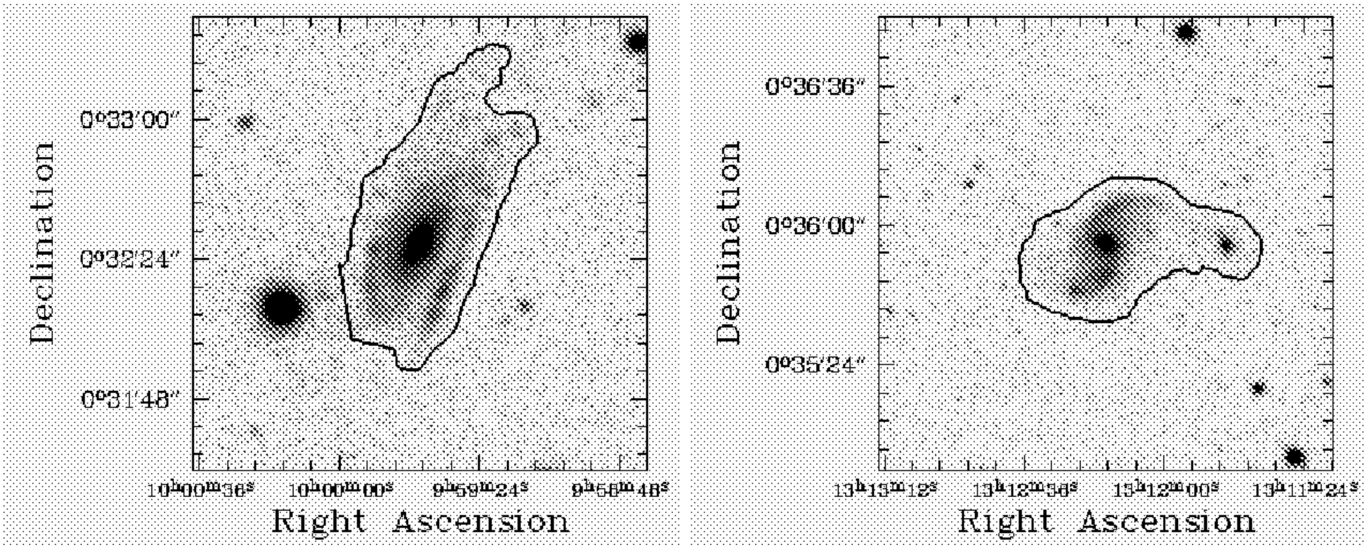

FIG. 15.— Combined g, r, and i images of the galaxies SDSS J101142+003520 and SDSS J131215+003554 with superimposed isophotes that correspond to the threshold level of the selection criterion. Both galaxies together with SDSS J140831-000737 (see Figure 13) were found as unusual objects using the $(g^* - r^*)$ vs. C plot in the region of the parameters $(g^* - i^*) < 0.^{\rm m}9$ and $C > 2.8$ (see Figure 14). Galaxy SDSS J101142+003520 (*left panel*) looks lopsided, and galaxy SDSS J131215+003554 (*right panel*) exhibits either a bright H II region, an interacting galaxy, or a superimposed background galaxy at the far end of its western spiral arm. The small object was observed spectroscopically by the SDSS. It has a velocity of 14406 km s^{-1} and a strong H II emission line spectrum. A spectrum for the galaxy SDSS J131215+003554 has not yet been obtained, preventing further interpretation.

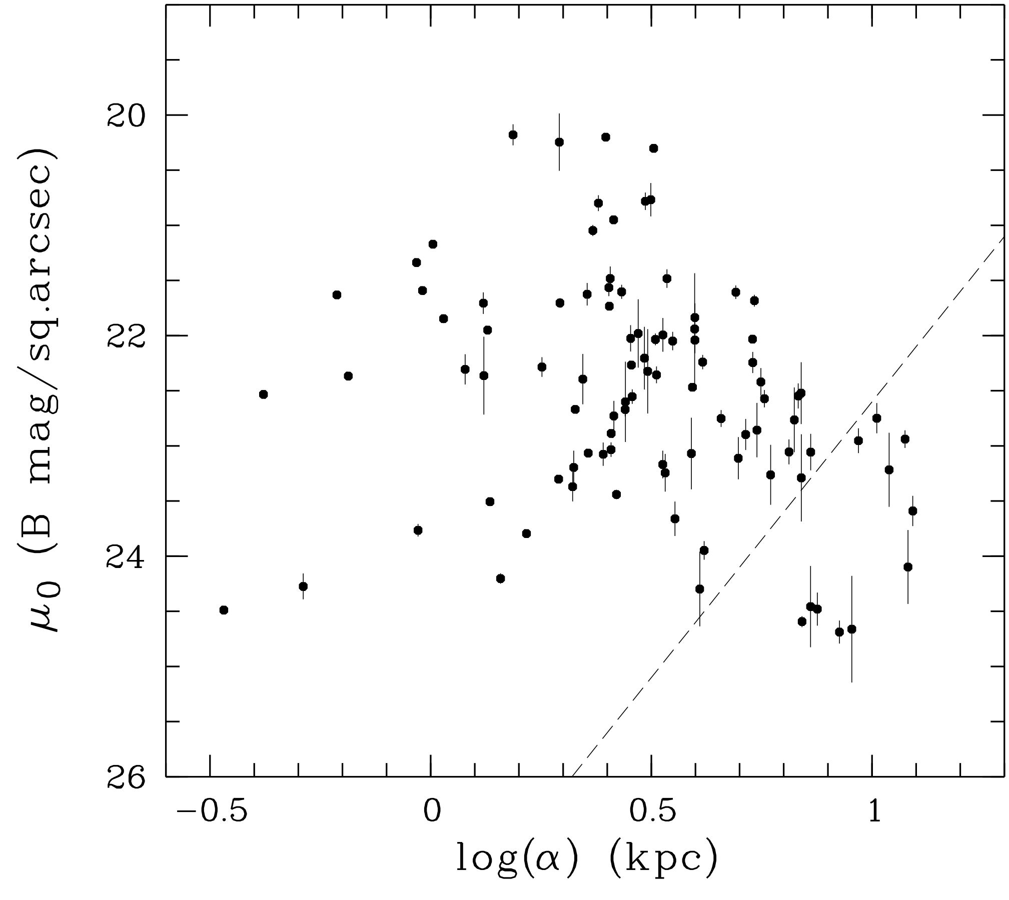

FIG. 16.— Central surface brightness μ_0 as a function of scale length α for our sample. The dashed line marks the cutoff in "diffuseness index" of $\mu_{0,\rm c}(B) + 5 \cdot \log(\alpha) = 27.6$, which is used to define a giant LSB disk (Sprayberry et al. 1995).

TABLE 1

The general parameters of large-angular-size galaxies identified in the fields of the test subsample.

#	SDSS name (1)	Impey name (2)	α(2000.0) (3)	δ(2000.0) (4)	R,C,F (5)	B mag (6)	$B-V$ mag (7)	M_B mag (8)	V_{hel} km/s (9)	Type (10)	Other names (11)
1	SDSS J095146+001950		09:51:46.80	+00:19:50.09	756 4 214	17.13±0.05	0.99	−20.51	25291	Sc(r)	
2	SDSS J095138+002211	0949+0036	09:51:38.88	+00:22:11.27	756 4 214	17.31±0.06	0.58	−14.70	1897	Im	
3	SDSS J095938+003047		09:59:38.16	+00:30:47.29	752 5 42	16.72±0.04	0.67	−20.35	19466	Sa	
4	SDSS J095939+003227		09:59:39.60	+00:32:27.57	752 5 42	16.11±0.03	0.72	−20.15	13386	SBc	UGC5370
5	SDSS J095939+003511	0957+0049	09:59:39.60	+00:35:11.89	752 5 42	15.95±0.03	0.92	−21.15	19762	Irr?	
6	SDSS J095959+003816	0957+0052	09:59:59.52	+00:38:16.02	756 5 228	16.88±0.05	0.55	−18.69	9735	Sm	
7	SDSS J095930−003745		09:59:30.24	−00:37:45.46	752 2 42	17.45±0.06	0.80			Sa	
8	SDSS J100439+001653		10:04:39.36	+00:16:53.38	756 4 236	17.07±0.05	0.85	−17.60	6464	E?	
9	SDSS J100440+001942		10:04:40.56	+00:19:42.77	756 4 236	17.95±0.07	0.89	−19.90	27883	SBc	
10	SDSS J100440+002211	1002+0036	10:04:40.80	+00:22:11.57	756 4 236	16.29±0.03	0.99	−19.92	13042	SBb(r)	
11	SDSS J101114+002646		10:11:14.16	+00:26:46.94	752 5 62	17.75±0.06	1.17	−20.24	29752	Sa	
12	SDSS J101117+002632	1008+0041	10:11:17.76	+00:26:32.43	752 5 62	14.20±0.01	0.69	−19.24	3644	SBb	UGC5493
13	SDSS J101142+003520		10:11:42.48	+00:35:20.58	752 5 62	17.32±0.06	0.70	−20.64	29378	S0	
14	SDSS J103135−005624	1029−0040	10:31:35.04	−00:56:24.18	756 1 281	16.68±0.04	0.73			Sc	
15	SDSS J103339−003939	1031−0024	10:33:39.84	−00:39:39.91	752 2 99	17.44±0.06	0.59			Sc	
16	SDSS J103825−000104	1035+0014	10:38:25.44	−00:01:04.77	756 3 292	16.76±0.04	0.64	−17.63	5656	SBc	
17	SDSS J103806−000319		10:38:06.96	−00:03:19.32	756 3 292	18.11±0.08	0.55			Irr	
18	SDSS J104406−005744	1041−0041	10:44:06.00	−00:57:44.85	756 1 302	16.87±0.04	0.63	−18.20	7759	Sc	
19	SDSS J104509+000433	1042+0020	10:45:09.12	+00:04:33.22	752 4 118	16.71±0.04	0.86	−21.09	27185	Irr	MCG+00−28−005
20	SDSS J104504+000617		10:45:04.32	+00:06:17.25	752 4 118	15.16±0.02	0.78	−20.82	11791	SBb	UGC5867
21	SDSS J104614+000300	1043+0018	10:46:14.88	+00:03:00.75	752 4 120	15.98±0.03	0.46	−20.37	13966	Sm	CGCG010−007
22	SDSS J104819−000119	1045+0014	10:48:19.92	−00:01:19.16	756 3 309	16.30±0.03	0.68	−19.65	11644	Sc	
23	SDSS J110440+000329	1102+0019	11:04:40.32	+00:03:29.16	752 4 151	17.38±0.06	0.74			dE	
24	SDSS J110548−000209		11:05:48.48	−00:02:09.15	756 3 338	9.85±0.00	0.92	−20.30	805	SABbc	NGC3521
25	SDSS J110546−000813	1103+0007	11:05:46.56	−00:08:13.38	756 3 338	16.69±0.04	0.61			SBc	
26	SDSS J110535−000946		11:05:35.28	−00:09:46.65	756 3 338	16.36±0.03	0.82	−19.52	11226	Sc	PGC033536
27	SDSS J110646+001524		11:06:46.32	+00:15:24.12	756 4 340	16.82±0.04	1.06	−19.31	12611	S0	
28	SDSS J110655−001845	1104−0002	11:06:55.20	−00:18:45.86	752 3 155	17.02±0.05	0.52	−18.47	9379	Sm	
29	SDSS J110708+002152	1104+0038	11:07:08.40	+00:21:52.91	756 4 340	17.66±0.06	0.62			Irr	
30	SDSS J110840+001602	1106+0032	11:08:40.32	+00:16:02.65	756 4 343	14.90±0.02	0.73	−20.14	7639	Sm	CGCG011−004
31	SDSS J110839+001703		11:08:39.60	+00:17:03.67	756 4 343	16.16±0.03	1.05	−18.81	7411	S0	CGCG1106.1+0033
32	SDSS J110841+002331		11:08:41.04	+00:23:31.23	756 4 343	15.70±0.03	0.77	−19.32	7589	Sd	ARK279
33	SDSS J111055+010537	1108+0121	11:10:55.20	+01:05:37.86	756 6 347	15.88±0.03	0.46	−14.73	993	dI	CGCG011−018
34	SDSS J111050+011232	1108+0128	11:10:50.16	+01:12:32.22	756 6 347	16.59±0.04	0.60			SBc	
35	SDSS J111104+010525		11:11:04.08	+01:05:25.37	756 6 347	17.62±0.05	1.38	−20.18	27264	Sc	
36	SDSS J111117+010914		11:11:17.04	+01:09:14.90	756 6 347	17.62±0.06	1.02	−20.00	25083	Sa	
37	SDSS J111247−003406	1110−0017	11:12:47.76	−00:34:06.86	756 2 350	17.75±0.07	0.44	−17.52	8472	Sm	
38	SDSS J111549+005137	1113+0107	11:15:49.44	+00:51:37.34	752 6 170	15.53±0.02	0.93	−20.74	13444	Inter	UGC6284
39	SDSS J111612+005935		11:16:12.72	+00:59:35.39	752 6 170	17.75±0.07	0.79			SBc	
40	SDSS J111849+003709	1116+0053	11:18:49.44	+00:37:09.14	752 5 175	15.52±0.03	0.63	−19.64	8059	Sa	CGCG011−051
41	SDSS J111916+003241		11:19:16.08	+00:32:41.51	752 5 175	17.21±0.05	1.06			Sa	
42	SDSS J112418+003837		11:24:18.72	+00:38:37.50	756 5 369	15.05±0.02	0.55	−20.06	7905	SBc	CGCG011−090
43	SDSS J112409+004201	1121+0058	11:24:09.12	+00:42:01.94	756 5 369	15.26±0.02	0.65	−19.82	7784	Sc	CGCG011−089
44	SDSS J112712−005940	1124−0043	11:27:12.48	−00:59:40.51	756 1 374	14.89±0.02	0.57	−15.65	963	dIn	UGC6457
45	SDSS J112829+000838	1125+0025	11:28:29.52	+00:08:38.80	752 4 191	17.52±0.06	0.68	−18.99	15042	Sb	
46	SDSS J113158−000301	1129+0013	11:31:58.56	−00:03:01.32	756 3 382	16.17±0.03	0.65	−19.84	11899	Sbc	CGCG012−004
47	SDSS J113256−004024		11:32:56.88	−00:40:24.21	752 2 198	18.67±0.09	1.45	−20.52	51726	S0	
48	SDSS J113245−004428	1130−0027	11:32:45.12	−00:44:28.42	752 2 198	16.00±0.03	0.51	−18.75	6688	Sm	CGCG012−015
49	SDSS J113457−004514	1132−0028	11:34:57.12	−00:45:14.66	752 2 201	16.67±0.04	0.55	−17.76	5783	Sm	
50	SDSS J120148−010802		12:01:48.96	−01:08:02.80	752 1 246	17.79±0.06	1.21	−20.55	34872	Sa	
51	SDSS J120140−011213	1159−0055	12:01:40.56	−01:12:13.50	752 1 246	18.00±0.08	0.63			Irr	
52	SDSS J120804+004153	1205+0058	12:08:04.08	+00:41:53.58	756 5 442	16.16±0.03	0.62	−18.31	5870	Irr	
53	SDSS J121121+010348	1208+0120	12:11:21.36	+01:03:48.82	756 6 448	16.09±0.03	0.61	−20.28	14100	Inter	UM480
54	SDSS J121243+005854	1210+0115	12:12:43.92	+00:58:54.71	752 6 265	18.77±0.12	0.55			dE	
55	SDSS J121257+011348	1210+0130	12:12:57.12	+01:13:48.04	756 6 450	18.70±0.11	0.71			dE	
56	SDSS J121203−003621	1209−0019	12:12:03.36	−00:36:21.59	756 2 449	16.19±0.04	0.42	−19.55	10544	Sm	CGCG013−101, UM482
57	SDSS J121500−005506		12:15:00.96	−00:55:06.28	756 1 454	17.98±0.06	1.21	−20.12	31273	Sb	
58	SDSS J121526−005622	1212−0039	12:15:26.88	−00:56:22.53	756 1 454	18.31±0.08	0.99	−19.07	22449	Sc	
59	SDSS J121502−010212		12:15:02.16	−01:02:12.52	756 1 454	17.87±0.07	0.56	−19.74	24944	Sc	
60	SDSS J121604+011049	1213+0127	12:16:04.56	+01:10:49.69	756 6 455	15.65±0.03	0.64	−20.86	14976	Sa	CGCG013−116
61	SDSS J121925+001244	1216+0029	12:19:25.92	+00:12:44.72	756 4 461	16.96±0.05	0.52	−13.36	867	dI	
62	SDSS J122034+004714	1217+0103	12:20:34.32	+00:47:14.25	756 5 463	14.99±0.02	0.59	−17.26	2109	Sm	UGC7396
63	SDSS J122342−001526	1221+0001	12:23:42.24	−00:15:26.67	752 3 283	18.16±0.08	0.73			Sm	
64	SDSS J122430+000416	1221+0020	12:24:30.96	+00:04:16.85	752 4 284	17.32±0.06	0.52	−16.64	4650	Irr	KDG118
65	SDSS J122427+000910		12:24:27.36	+00:09:10.21	752 4 284	15.08±0.02	0.80	−19.97	7646	SBd(s)	UGC7487
66	SDSS J122404+011123	1221+0128	12:24:04.80	+01:11:23.39	756 6 469	15.52±0.02	0.75	−19.62	7982	Sd	CGCG014−042
67	SDSS J122411+011247		12:24:11.76	+01:12:47.77	756 6 469	15.81±0.03	0.67	−19.32	7949	Sd	CGCG0014−044
68	SDSS J122619+010112	1223+0117	12:26:19.20	+01:01:12.04	752 6 287	16.93±0.05	0.61	−14.54	1473	dI	
69	SDSS J122654−005239		12:26:54.72	−00:52:39.53	756 1 474	14.01±0.01	0.90	−18.31	2179	SABa	NGC4355, UGC7545
70	SDSS J122610−010923		12:26:10.08	−01:09:23.22	752 1 287	17.00±0.04	0.70	−19.12	12583	BCG	
71	SDSS J122622−011520	1223−0058	12:26:22.56	−01:15:20.77	752 1 287	16.52±0.04	0.33	−15.63	2018	dI	UM501
72	SDSS J122704−005421	1224−0037	12:27:04.56	−00:54:21.56	756 1 474	15.16±0.02	0.56	−17.21	2229	Irr	CGCG014−040, VV635
73	SDSS J122903+000614	1226+0022	12:29:03.84	+00:06:14.44	752 4 292	16.40±0.04	0.71			dE	
74	SDSS J122902+001159		12:29:02.16	+00:11:59.93	752 4 292	18.19±0.07	1.14	−20.02	32937	S0	
75	SDSS J122912+004903	1226+0105	12:29:12.96	+00:49:03.89	756 5 477	16.33±0.03	0.83	−21.17	23655	Sc	
76	SDSS J122921+010324	1226+0119	12:29:21.60	+01:03:24.95	756 6 478	15.06±0.02	0.64	−19.78	6958	Scd	CGCG014−051
77	SDSS J122932+010608		12:29:32.40	+01:06:08.96	756 6 478	17.31±0.05	1.45	−20.16	23400	S0	
78	SDSS J123141+005733		12:31:41.28	+00:57:33.40	752 6 296	17.94±0.07	0.99	−16.89	6932	S0	
79	SDSS J123116+005939	1228+0116	12:31:16.56	+00:59:39.95	752 6 296	18.07±0.08	0.48	−14.35	2289	dI	
80	SDSS J123309−002231	1230−0005	12:33:09.60	−00:22:31.20	752 3 299	18.28±0.09	0.84			dE	
81	SDSS J123307−003159	1230−0015	12:33:07.92	−00:31:59.06	756 2 484	16.43±0.04	0.61	−16.77	3279	Irr	UGCA285

TABLE 1—*Continued*

#	SDSS name (1)	Impey name (2)	α(2000.0) (3)	δ(2000.0) (4)	R,C,F (5)	B mag (6)	$B-V$ mag (7)	M$_B$ mag (8)	V$_{\rm hel}$ km/s (9)	Type (10)	Other names (11)
82	SDSS J125004−001356	1247+0002	12:50:04.80	−00:13:56.28	752 3 327	17.99±0.08	0.70			dE	
83	SDSS J125323−002529	1250−0009	12:53:23.28	−00:25:29.47	756 2 518	16.21±0.03	0.97	−20.52	16667	Inter	CGCG015−030
84	SDSS J125405−000604	1251+0010	12:54:05.04	−00:06:04.90	756 3 519	16.55±0.04	0.84	−13.26	688	dEn	
85	SDSS J125700+010142	1254+0117	12:57:00.24	+01:01:42.56	752 6 339	15.74±0.03	0.55	−18.15	4489	SBc	UGC8066
86	SDSS J130058−000139	1258+0014	13:00:58.56	−00:01:39.18	756 3 530	12.73±0.01	0.73	−18.24	1169	SBc(s)	NGC4904, UGC8121
87	SDSS J130243+003949	1300+0055	13:02:43.44	+00:39:49.93	756 5 533	15.81±0.03	0.89	−20.24	12176	SBc	CGCG015−058
88	SDSS J130931+005125		13:09:31.92	+00:51:25.16	752 6 360	13.84±0.01	1.04	−20.46	5443	SB0+	NGC4996, UGC8235
89	SDSS J131004+005655	1307+0112	13:10:04.56	+00:56:55.97	752 6 360	17.14±0.05	0.64	−17.32	5842	dIn	
90	SDSS J131201+003532	1309+0051	13:12:01.92	+00:35:32.98	752 5 364	17.25±0.06	0.62	−17.16	5700	Irr	
91	SDSS J131215+003554		13:12:15.36	+00:35:54.91	752 5 364	16.42±0.04	0.60			SBcd	
92	SDSS J131244−000223	1310+0013	13:12:44.88	−00:02:23.76	756 3 550	17.12±0.05	0.69			dEn	
93	SDSS J131305−003540	1310−0019	13:13:05.76	−00:35:40.88	756 2 551	16.97±0.04	1.15	−19.06	12040	SBc	
94	SDSS J131809+001322	1315+0029	13:18:09.36	+00:13:22.12	756 4 559	15.85±0.03	0.59	−19.66	9497	Sm	CGCG016−048
95	SDSS J131821+002055		13:18:21.60	+00:20:55.96	756 4 559	17.03±0.05	0.75	−20.31	22004	Sd	
96	SDSS J131821+002440		13:18:21.36	+00:24:40.60	756 4 559	17.88±0.07	0.77	−19.56	23058	Sc?	
97	SDSS J132345+010231	1321+0118	13:23:45.12	+01:02:31.27	752 6 383	16.85±0.04	0.77	−21.29	31814	Sc	
98	SDSS J132926+005412	1326+0109	13:29:26.40	+00:54:12.92	752 6 393	16.16±0.03	0.61	−17.03	3267	Sm	UGC8784
99	SDSS J133031−003613	1327−0020	13:30:31.92	−00:36:13.53	756 2 580	15.72±0.03	0.71	−20.92	15908	Inter	CGCG016−084
100	SDSS J133305−010208	1330−0046	13:33:05.28	−01:02:08.99	756 1 584	13.53±0.01	0.92	−19.94	3713	SBb(r)	NGC5211, UGC8530
101	SDSS J133435−002109		13:34:35.52	−00:21:09.25	752 3 401	15.84±0.03	0.59	−17.74	3897	Irr	UM588, CGCG017−027
102	SDSS J135244+000748	1350+0022	13:52:44.64	+00:07:48.67	752 4 432	16.02±0.03	0.59	−17.92	4605	Sm	UM619, CGCG017−086
103	SDSS J135230+002504	1349+0039	13:52:30.96	+00:25:04.36	756 4 617	17.02±0.05	0.79	−20.93	29156	Sb	
104	SDSS J135214+003540		13:52:14.88	+00:35:40.84	752 5 431	16.96±0.04	1.07	−19.34	13595	SB0	
105	SDSS J135943−003133	1357−0017	13:59:43.68	−00:31:33.72	756 2 629	17.62±0.07	0.37	−16.15	4255	Irr	
106	SDSS J135943−003424		13:59:43.20	−00:34:24.68	756 2 629	17.74±0.06	0.86	−21.33	49046	Sc	
107	SDSS J140042−003020	1358−0015	14:00:42.96	−00:30:20.46	756 2 630	15.75±0.03	0.54	−17.53	3403	Sm	CGCG018−021
108	SDSS J140327+004359		14:03:27.84	+00:43:59.61	756 5 635	15.87±0.03	0.88	−20.29	12838	Sb	CGCG018−036
109	SDSS J140344+004849	1401+0103	14:03:44.16	+00:48:49.74	756 5 635	15.29±0.02	0.65	−20.84	12582	Sc	CGCG018−038
110	SDSS J140320−003259	1400−0018	14:03:20.88	−00:32:59.25	756 2 635	14.66±0.02	0.66	−20.31	7388	Sa	CGCG018−035
111	SDSS J140403+005347	1401+0108	14:04:03.60	+00:53:47.59	752 6 451	15.98±0.03	0.58	−20.20	12901	Sb	CGCG018−039
112	SDSS J140405+005953	1401+0114	14:04:05.04	+00:59:53.68	752 6 451	16.65±0.04	0.44	−18.34	7482	Sm	
113	SDSS J140831−000737	1405+0006	14:08:31.68	−00:07:37.47	756 3 643	15.52±0.03	0.52	−19.49	7518	SBb	CGCG018−057
114	SDSS J143327−000708	1430+0005	14:33:27.12	−00:07:08.64	756 3 685	16.09±0.03	0.50	−19.60	10300	Irr	
115	SDSS J143638+000702	1434+0020	14:36:38.64	+00:07:02.59	752 4 505	17.31±0.06	0.63	−18.09	9030	Sd	
116	SDSS J143907+003030	1436+0043	14:39:07.20	+00:30:30.78	752 5 509	16.24±0.04	0.56	−19.37	9932	Sm	
117	SDSS J143960−001110	1437+0001	14:39:60.00	−00:11:10.24	756 3 696	18.34±0.09	0.67			dI	
118	SDSS J143940−001810	1437−0005	14:39:40.80	−00:18:10.46	752 3 510	17.17±0.05	0.68	−14.89	1939	dI	
119	SDSS J144056−001905	1438−0006	14:40:56.40	−00:19:05.19	752 3 512	12.95±0.01	1.15	−18.88	1743	SBb	NGC5719, UGC9462
120	SDSS J144103+003709	1438+0049	14:41:03.84	+00:37:09.67	752 5 512	16.73±0.04	0.70	−16.16	2837	dIn	
121	SDSS J144148+004114	1439+0053	14:41:48.72	+00:41:14.10	756 5 699	15.03±0.02	0.61	−16.98	1886	Sm	UGC9470
122	SDSS J144245−002103	1440−0008	14:42:45.84	−00:21:03.41	752 3 515	14.71±0.02	0.56	−17.08	1711	dIn	NGC5733
123	SDSS J144300−002259	1440−0010	14:43:00.48	−00:22:59.91	752 3 516	16.51±0.04	0.65	−15.33	1744	dI	
124	SDSS J144525+001404	1442+0026	14:45:25.44	+00:14:04.50	756 4 705	16.69±0.04	0.79			Sbc	
125	SDSS J144856−004337	1446−0031	14:48:56.40	−00:43:37.62	752 2 526	17.67±0.06	1.25	−17.58	8415	SBc	
126	SDSS J144821−004827		14:48:21.36	−00:48:27.24	752 2 525	16.61±0.04	0.85	−20.15	16841	Scd(r)	
127	SDSS J144900−003852		14:49:00.96	−00:38:52.10	752 2 526	16.90±0.04	1.13	−19.24	12689	S0	
128	SDSS J144916−004240		14:49:16.56	−00:42:40.27	752 2 526	17.15±0.05	1.06	−19.04	12935	Sa	
129	SDSS J144909−005410	1446−0041	14:49:09.36	−00:54:10.23	756 1 711	16.23±0.03	0.63	−19.00	8325	Sc	

TABLE 2

TOTAL MAGNITUDES AND MODEL-INDEPENDENT PARAMETERS OF LARGE-ANGULAR-SIZE GALAXIES IDENTIFIED IN THE TEST FIELDS.

#	SDSS name (1)	u^* mag (2)	g^* mag (3)	r^* mag (4)	i^* mag (5)	z^* mag (6)	b/a (7)	PA deg (8)	$R_{\rm eff}(r)$ ″ (9)	$\mu_{\rm eff}(r)$ mag/□″ (10)	C(r) (11)	$a_{26.2}(r)$ ″ (12)
1	SDSS J095146+001950	18.09± 0.10	16.59± 0.03	15.81± 0.03	15.42± 0.02	15.04± 0.05	0.47	24	3.6	20.6	3.1	16.4
2	SDSS J095138+002211	17.44± 0.08	16.97± 0.04	16.60± 0.04	16.38± 0.04	16.47± 0.17	0.77	−58	12.3	24.0	2.1	24.2
3	SDSS J095938+003047	17.31± 0.06	16.33± 0.03	15.87± 0.03	15.41± 0.02	15.17± 0.04	0.94	13	3.1	20.3	2.3	12.5
4	SDSS J095939+003227	16.76± 0.05	15.70± 0.02	15.19± 0.02	14.83± 0.02	14.63± 0.03	0.46	65	6.9	21.4	3.3	26.1
5	SDSS J095939+003511	16.68± 0.05	15.45± 0.02	14.74± 0.02	14.28± 0.01	13.97± 0.02	0.87	87	7.9	21.2	1.8	23.0
6	SDSS J095959+003816	17.26± 0.06	16.55± 0.03	16.21± 0.03	15.89± 0.03	15.71± 0.06	0.92	86	5.3	21.8	2.3	18.4
7	SDSS J095930−003745	17.97± 0.08	17.01± 0.04	16.45± 0.03	16.07± 0.04	15.45± 0.05	0.80	−55	3.4	21.1	2.7	13.9
8	SDSS J100439+001653	17.91± 0.09	16.61± 0.03	15.97± 0.03	15.49± 0.03	15.30± 0.06	0.93	−80	4.3	21.1	3.0	18.0
9	SDSS J100440+001942	18.48± 0.12	17.46± 0.05	16.79± 0.04	16.41± 0.04	15.84± 0.08	0.66	42	4.4	22.0	2.5	14.8
10	SDSS J100440+002211	17.29± 0.07	15.75± 0.02	14.98± 0.02	14.60± 0.02	14.27± 0.04	0.79	82	4.4	20.2	4.1	25.6
11	SDSS J101114+002646	19.09± 0.13	17.15± 0.04	16.14± 0.03	15.71± 0.03	15.35± 0.05	0.76	10	4.5	21.4	2.5	15.3
12	SDSS J101117+002632	15.01± 0.02	13.80± 0.01	13.31± 0.01	13.01± 0.01	12.80± 0.01	0.78	8	17.3	21.5	2.0	47.1
13	SDSS J101142+003520	17.93± 0.08	16.92± 0.04	16.43± 0.03	16.07± 0.03	15.88± 0.06	0.71	−86	3.2	21.0	3.0	14.1
14	SDSS J103135−005624	17.28± 0.06	16.27± 0.02	15.75± 0.02	15.48± 0.03	15.22± 0.05	0.63	19	7.7	22.2	2.2	22.0
15	SDSS J103339−003939	17.91± 0.09	17.09± 0.04	16.71± 0.04	16.40± 0.04	16.21± 0.08	0.59	−46	7.2	23.0	2.0	17.9
16	SDSS J103825−000104	17.38± 0.07	16.38± 0.03	15.95± 0.03	15.72± 0.03	15.34± 0.06	0.61	−13	10.8	23.1	2.1	25.6
17	SDSS J103806−000319	18.82± 0.13	17.78± 0.05	17.44± 0.06	17.11± 0.06	16.39± 0.10	0.47	−79	8.2	24.0	1.7	14.5
18	SDSS J104406−005744	17.31± 0.07	16.50± 0.03	16.08± 0.03	16.00± 0.03	15.64± 0.07	0.88	42	9.9	23.1	2.0	23.6
19	SDSS J104509+000433	17.31± 0.07	16.23± 0.03	15.58± 0.02	15.22± 0.02	14.81± 0.05	0.65	62	8.0	22.1	2.4	24.6
20	SDSS J104504+000617	15.88± 0.03	14.72± 0.01	14.15± 0.01	13.80± 0.01	13.59± 0.03	0.81	42	10.7	21.3	2.5	39.5
21	SDSS J104614+000300	16.59± 0.04	15.69± 0.02	15.43± 0.02	15.13± 0.02	15.06± 0.05	0.68	−86	4.4	20.7	2.8	17.8
22	SDSS J104819−000119	17.05± 0.06	15.91± 0.02	15.45± 0.02	15.08± 0.02	14.73± 0.04	0.87	−47	7.2	21.7	2.0	19.9
23	SDSS J110440+000329	18.10± 0.10	16.97± 0.04	16.44± 0.04	16.15± 0.04	15.72± 0.08	0.91	31	11.9	23.8	1.9	24.6
24	SDSS J110548−000209	10.82± 0.00	9.35± 0.00	8.66± 0.00	8.26± 0.00	7.97± 0.00	0.69	−25	65.6	19.7	3.0	367.0
25	SDSS J110546−000813	17.34± 0.06	16.33± 0.03	15.93± 0.03	15.71± 0.03	15.49± 0.06	0.56	−69	5.5	21.6	2.7	19.5
26	SDSS J110535−000946	17.21± 0.06	15.90± 0.02	15.29± 0.02	14.93± 0.02	14.65± 0.04	0.49	−64	5.2	20.9	2.4	18.6
27	SDSS J110646+001524	17.89± 0.08	16.25± 0.03	15.41± 0.02	14.98± 0.02	14.66± 0.04	0.62	6	2.3	19.2	4.8	18.7
28	SDSS J110655−001845	17.72± 0.07	16.70± 0.03	16.38± 0.03	16.15± 0.03	16.07± 0.08	0.89	24	6.2	22.4	2.3	18.8
29	SDSS J110708+002152	18.24± 0.10	17.30± 0.04	16.89± 0.04	16.43± 0.04	16.57± 0.10	0.82	−8	6.5	22.9	2.1	16.1
30	SDSS J110840+001602	15.56± 0.03	14.49± 0.01	13.97± 0.01	13.65± 0.01	13.39± 0.02	0.83	56	8.0	20.5	2.2	27.5
31	SDSS J110839+001703	17.28± 0.06	15.60± 0.02	14.77± 0.02	14.37± 0.01	14.01± 0.03	0.60	−7	2.6	18.8	4.1	19.6
32	SDSS J110841+002331	16.47± 0.04	15.27± 0.02	14.72± 0.02	14.40± 0.02	14.12± 0.03	0.81	46	5.3	20.3	2.5	24.5
33	SDSS J111055+010537	16.58± 0.05	15.59± 0.02	15.33± 0.02	15.21± 0.02	14.97± 0.05	0.45	−24	11.6	22.6	2.1	29.5
34	SDSS J111050+011232	17.12± 0.07	16.23± 0.03	15.84± 0.03	15.59± 0.03	15.35± 0.06	0.74	69	8.3	22.4	2.3	23.2
35	SDSS J111104+010525	18.38± 0.12	16.91± 0.04	15.72± 0.02	15.76± 0.03	15.38± 0.05	0.63	45	6.1	21.7	2.6	21.2
36	SDSS J111117+010914	18.31± 0.12	17.08± 0.04	16.27± 0.03	15.87± 0.03	15.47± 0.06	0.42	76	3.2	20.8	3.9	15.1
37	SDSS J111247−003406	18.26± 0.11	17.47± 0.05	17.24± 0.05	17.00± 0.06	16.88± 0.13	0.67	−82	8.6	23.9	1.9	17.9
38	SDSS J111549+005137	16.56± 0.06	15.02± 0.02	14.30± 0.01	13.88± 0.01	13.57± 0.02	0.47	67	8.4	20.9	3.2	35.2
39	SDSS J111612+005935	18.47± 0.13	17.31± 0.04	16.73± 0.04	16.38± 0.04	16.03± 0.07	0.82	68	4.0	21.8	2.0	11.8
40	SDSS J111849+003709	16.11± 0.04	15.15± 0.02	14.72± 0.02	14.47± 0.02	14.26± 0.03	0.88	−64	4.6	20.1	2.4	21.1
41	SDSS J111916+003241	18.16± 0.09	16.64± 0.03	15.80± 0.02	15.33± 0.02	14.97± 0.04	0.79	−78	4.4	21.0	2.8	19.2
42	SDSS J112418+003837	15.76± 0.03	14.72± 0.01	14.38± 0.01	14.19± 0.01	14.02± 0.02	0.99	−79	8.1	20.9	2.3	27.8
43	SDSS J112409+004201	16.02± 0.03	14.88± 0.01	14.45± 0.01	14.19± 0.01	13.96± 0.02	0.53	82	8.7	21.1	2.2	28.3
44	SDSS J112712−005940	15.60± 0.03	14.55± 0.01	14.19± 0.01	13.99± 0.01	13.80± 0.03	0.73	−34	15.8	22.2	2.4	48.3
45	SDSS J112829+000838	17.98± 0.09	17.13± 0.04	16.65± 0.04	16.34± 0.04	16.08± 0.08	0.87	1	6.0	22.5	1.9	14.6
46	SDSS J113158−000301	17.05± 0.06	15.79± 0.02	15.35± 0.02	14.99± 0.02	14.97± 0.05	0.60	80	8.4	22.0	2.3	25.7
47	SDSS J113256−004024	19.24± 0.17	17.93± 0.06	16.70± 0.04	16.22± 0.04	15.85± 0.07	0.52	13	4.0	21.7	2.8	14.5
48	SDSS J113245−004428	16.61± 0.05	15.69± 0.02	15.39± 0.02	15.18± 0.02	14.94± 0.04	0.91	88	10.1	22.4	1.9	23.7
49	SDSS J113457−004514	17.16± 0.06	16.34± 0.03	15.99± 0.03	15.74± 0.03	15.46± 0.06	0.75	80	8.1	22.5	2.3	22.4
50	SDSS J120148−010802	18.41± 0.11	17.15± 0.04	16.16± 0.03	15.67± 0.03	15.26± 0.05	0.74	65	3.5	20.9	3.8	17.8
51	SDSS J120140−011213	17.99± 0.09	17.63± 0.05	17.21± 0.06	16.99± 0.06	16.44± 0.10	0.80	−44	13.3	24.8	2.0	16.1
52	SDSS J120804+004153	16.75± 0.05	15.80± 0.02	15.39± 0.02	15.23± 0.02	14.98± 0.04	0.69	−18	5.4	21.1	2.3	18.4
53	SDSS J121121+010348	16.82± 0.06	15.74± 0.02	15.34± 0.02	15.02± 0.02	14.83± 0.04	0.85	−63	7.2	21.6	1.9	19.3
54	SDSS J121243+005854		18.43± 0.07	18.09± 0.08	17.75± 0.08	16.62± 0.10	0.83	−49	7.6	24.5	1.8	13.8
55	SDSS J121257+011348	19.52± 0.24	18.30± 0.07	17.80± 0.07	17.18± 0.06	16.48± 0.09	0.54	27	9.1	24.6	2.1	14.0
56	SDSS J121203−003621	16.72± 0.05	15.92± 0.02	15.70± 0.02	15.52± 0.03	15.14± 0.05	0.64	61	7.4	22.0	2.2	20.6
57	SDSS J121500−005506	18.82± 0.13	17.35± 0.04	16.36± 0.03	16.12± 0.03	15.75± 0.06	0.91	64	3.4	21.0	3.7	17.6
58	SDSS J121526−005622	18.86± 0.13	17.78± 0.05	17.01± 0.04	16.87± 0.05	16.36± 0.08	0.76	60	7.6	23.4	2.1	18.2
59	SDSS J121502−010212	18.24± 0.10	17.53± 0.05	17.18± 0.05	16.85± 0.05	16.49± 0.09	0.81	30	5.6	22.9	2.2	14.7
60	SDSS J121604+011049	16.32± 0.05	15.27± 0.02	14.85± 0.02	14.55± 0.02	14.38± 0.03	0.90	45	4.6	20.1	2.0	16.3
61	SDSS J121925+001244	17.55± 0.07	16.64± 0.03	16.33± 0.03	16.14± 0.03	15.85± 0.08	0.29	10	10.6	23.4	2.3	24.5
62	SDSS J122034+004714	15.51± 0.03	14.64± 0.01	14.25± 0.01	14.04± 0.01	13.89± 0.02	0.31	−77	16.3	22.3	2.3	46.5
63	SDSS J122342−001526	18.37± 0.11	17.75± 0.05	17.23± 0.05	16.95± 0.05	16.46± 0.10	0.81	−48	8.3	23.8	2.0	18.3
64	SDSS J122430+000416	17.87± 0.09	17.00± 0.04	16.69± 0.04	16.52± 0.04	16.31± 0.10	0.81	−25	10.9	23.9	1.8	21.6
65	SDSS J122427+000910	15.85± 0.03	14.63± 0.01	14.04± 0.01	13.73± 0.01	13.45± 0.02	0.82	7	10.8	21.2	2.2	35.0
66	SDSS J122404+011123	16.22± 0.05	15.09± 0.02	14.56± 0.01	14.28± 0.01	14.08± 0.03	0.73	−44	7.2	20.8	2.5	28.0
67	SDSS J122411+011247	16.54± 0.05	15.42± 0.02	14.96± 0.02	14.67± 0.02	14.45± 0.04	0.92	12	8.8	21.7	2.1	25.2
68	SDSS J122619+010112	17.56± 0.08	16.57± 0.03	16.17± 0.03	15.93± 0.03	15.63± 0.06	0.58	21	7.4	22.5	2.4	22.2
69	SDSS J122654−005239	15.14± 0.02	13.52± 0.01	12.83± 0.01	12.43± 0.01	12.21± 0.01	0.50	61	10.8	20.0	3.1	54.3
70	SDSS J122610−010923	17.72± 0.07	16.60± 0.03	16.11± 0.03	15.76± 0.03	15.32± 0.05	0.73	28	4.0	21.1	2.3	16.8
71	SDSS J122622−011520	16.82± 0.05	16.29± 0.03	16.16± 0.03	16.18± 0.04	15.69± 0.07	0.71	28	10.3	23.2	2.0	24.7
72	SDSS J122704−005421	15.69± 0.03	14.82± 0.01	14.47± 0.01	14.31± 0.02	14.17± 0.03	0.75	−13	10.9	21.7	2.4	36.2
73	SDSS J122903+000614	17.13± 0.06	15.99± 0.02	15.49± 0.02	15.23± 0.02	15.02± 0.06	0.89	−85	13.4	23.1	2.2	33.9
74	SDSS J122902+001159	18.65± 0.14	17.59± 0.05	16.67± 0.04	16.25± 0.04	15.80± 0.07	0.70	42	2.7	20.8	3.9	13.1
75	SDSS J122912+004903	16.85± 0.05	15.87± 0.02	15.25± 0.02	14.91± 0.02	14.56± 0.03	0.83	43	8.7	22.0	3.0	30.8
76	SDSS J122921+010324	15.81± 0.04	14.68± 0.01	14.25± 0.01	14.03± 0.01	13.85± 0.03	0.73	13	10.2	21.3	2.1	31.4
77	SDSS J122932+010608	18.11± 0.11	16.56± 0.03	15.34± 0.02	15.23± 0.02	14.89± 0.04	0.64	37	4.4	20.5	4.1	24.4
78	SDSS J123141+005733	18.53± 0.13	17.40± 0.05	16.63± 0.04	16.16± 0.03	15.77± 0.06	0.88	68	2.8	20.9	3.4	14.1
79	SDSS J123116+005939	18.61± 0.13	17.78± 0.05	17.50± 0.06	16.79± 0.05	16.63± 0.10	0.83	12	9.8	24.4	1.8	17.2
80	SDSS J123309−002231	18.56± 0.12	17.82± 0.06	17.19± 0.05	16.89± 0.05	16.28± 0.09	0.54	−14	9.3	24.0	2.2	18.1
81	SDSS J123307−003159	16.88± 0.06	16.07± 0.03	15.67± 0.03	15.44± 0.03	14.65± 0.04	0.85	28	20.5	24.2	1.9	36.9

TABLE 2—*Continued*

#	SDSS name	u^*	g^*	r^*	i^*	z^*	b/a	PA	$R_{\rm eff}(r)$	$\mu_{\rm eff}(r)$	C(r)	$a_{26.2}(r)$
		mag	mag	mag	mag	mag		deg	″	mag/□″		″
	(1)	(2)	(3)	(4)	(5)	(6)	(7)	(8)	(9)	(10)	(11)	(12)
82	SDSS J125004−001356	18.65± 0.13	17.59± 0.05	17.10± 0.05	16.85± 0.05	16.86± 0.11	0.89	−77	11.3	24.4	1.8	22.4
83	SDSS J125323−002529	16.75± 0.05	15.69± 0.02	14.93± 0.02	14.56± 0.02	14.41± 0.04	0.40	41	14.8	22.8	1.5	28.9
84	SDSS J125405−000604	17.22± 0.07	16.09± 0.02	15.46± 0.02	15.17± 0.02	14.71± 0.05	0.81	10	14.7	23.3	2.3	36.7
85	SDSS J125700+010142	16.33± 0.05	15.40± 0.02	15.06± 0.02	14.84± 0.02	14.69± 0.04	0.65	−16	18.4	23.4	2.1	42.6
86	SDSS J130058−000139	13.48± 0.01	12.32± 0.00	11.81± 0.00	11.54± 0.00	11.36± 0.01	0.58	12	23.3	20.6	2.1	76.9
87	SDSS J130243+003949	16.72± 0.05	15.33± 0.02	14.65± 0.01	14.34± 0.01	14.01± 0.02	0.88	4	9.3	21.5	2.1	27.4
88	SDSS J130931+005125	15.09± 0.03	13.29± 0.01	12.47± 0.01	12.05± 0.01	11.74± 0.01	0.61	8	17.2	20.6	2.6	63.6
89	SDSS J131004+005655	17.67± 0.09	16.77± 0.03	16.34± 0.03	16.00± 0.03	15.75± 0.07	0.95	28	9.3	23.2	2.0	20.1
90	SDSS J131201+003532	17.61± 0.07	16.89± 0.04	16.48± 0.03	16.30± 0.04	15.85± 0.06	0.70	−76	9.2	23.3	2.0	20.9
91	SDSS J131215+003554	16.96± 0.05	16.06± 0.03	15.67± 0.02	15.36± 0.02	15.16± 0.04	0.52	−79	6.9	21.9	3.3	20.7
92	SDSS J131244−000223	17.74± 0.08	16.72± 0.03	16.24± 0.03	15.83± 0.03	15.54± 0.06	0.95	67	7.9	22.7	2.0	19.0
93	SDSS J131305−003540	17.34± 0.07	16.36± 0.03	15.41± 0.02	15.72± 0.03	15.33± 0.06	0.85	−32	11.9	22.8	1.9	27.4
94	SDSS J131809+001322	16.38± 0.04	15.50± 0.02	15.11± 0.02	14.95± 0.02	14.73± 0.04	0.83	20	11.1	22.3	2.0	28.0
95	SDSS J131821+002055	17.75± 0.07	16.62± 0.03	16.11± 0.03	15.71± 0.03	15.37± 0.06	0.67	82	5.2	21.7	2.4	16.4
96	SDSS J131821+002440	18.04± 0.10	17.44± 0.05	16.89± 0.04	16.39± 0.04	15.52± 0.07	0.42	21	4.1	21.9	3.9	16.6
97	SDSS J132345+010231	17.54± 0.09	16.42± 0.03	15.87± 0.03	15.50± 0.03	15.20± 0.05	0.70	83	7.8	22.3	2.0	20.0
98	SDSS J132926+005412	16.61± 0.06	15.80± 0.02	15.40± 0.02	15.25± 0.02	14.93± 0.05	0.97	50	16.5	23.5	1.9	34.7
99	SDSS J133031−003613	16.35± 0.04	15.31± 0.02	14.81± 0.02	14.49± 0.02	14.23± 0.03	0.37	−34	5.2	20.4	5.4	34.3
100	SDSS J133305−010208	14.42± 0.02	13.03± 0.01	12.33± 0.01	11.94± 0.01	11.68± 0.01	0.78	39	13.4	20.0	3.5	68.4
101	SDSS J133435−002109	16.59± 0.04	15.49± 0.02	15.11± 0.02	14.94± 0.02	14.78± 0.04	0.53	38	5.0	20.6	2.7	21.2
102	SDSS J135244+000748	16.47± 0.04	15.67± 0.02	15.29± 0.02	15.17± 0.02	15.00± 0.05	0.58	−43	5.3	20.9	2.3	20.4
103	SDSS J135230+002504	17.63± 0.08	16.57± 0.03	15.99± 0.03	15.57± 0.03	15.29± 0.06	0.94	−51	4.6	21.3	3.0	18.6
104	SDSS J135214+003540	18.07± 0.09	16.38± 0.03	15.53± 0.02	15.07± 0.02	14.56± 0.03	0.91	79	2.3	19.4	4.4	16.5
105	SDSS J135943−003133	18.22± 0.11	17.37± 0.04	17.19± 0.05	16.70± 0.05	16.67± 0.10	0.82	13	8.5	23.8	2.2	19.0
106	SDSS J135943−003424	17.58± 0.08	17.27± 0.04	16.62± 0.04	16.04± 0.04	15.57± 0.06	0.78	29	2.2	20.3	4.8	13.7
107	SDSS J140042−003020	16.26± 0.04	15.42± 0.02	15.09± 0.02	14.97± 0.02	14.86± 0.04	0.67	76	8.2	21.7	2.0	24.3
108	SDSS J140327+004359	16.75± 0.05	15.39± 0.02	14.73± 0.02	14.37± 0.02	14.06± 0.02	0.92	−81	7.7	21.2	2.1	25.6
109	SDSS J140344+004849	16.00± 0.03	14.91± 0.01	14.47± 0.01	14.17± 0.01	13.97± 0.02	0.86	−50	7.2	20.7	2.0	24.8
110	SDSS J140320−003259	15.28± 0.02	14.28± 0.01	13.83± 0.01	13.56± 0.01	13.35± 0.02	0.88	42	6.2	19.8	2.1	25.9
111	SDSS J140403+005347	16.82± 0.06	15.64± 0.02	15.26± 0.02	14.90± 0.02	14.71± 0.04	0.81	76	5.5	21.0	2.1	19.3
112	SDSS J140405+005953	17.09± 0.07	16.37± 0.03	16.14± 0.03	15.98± 0.03	15.90± 0.07	0.68	25	7.5	22.5	2.3	21.7
113	SDSS J140831−000737	16.17± 0.04	15.20± 0.02	14.88± 0.02	14.68± 0.02	14.33± 0.04	0.88	25	7.5	21.2	3.5	33.6
114	SDSS J143327−000708	16.77± 0.05	15.78± 0.02	15.49± 0.02	15.23± 0.02	15.03± 0.05	0.83	−58	12.6	23.0	1.9	28.3
115	SDSS J143638+000702	17.79± 0.09	16.94± 0.04	16.52± 0.04	16.23± 0.04	15.97± 0.08	0.59	71	7.0	22.7	2.1	17.8
116	SDSS J143907+003030	16.81± 0.05	15.90± 0.02	15.54± 0.02	15.32± 0.02	15.14± 0.04	0.72	32	8.9	22.3	2.1	24.5
117	SDSS J143960−001110	18.68± 0.13	17.95± 0.06	17.50± 0.06	17.35± 0.07	16.76± 0.12	0.65	−70	6.7	23.6	2.1	14.4
118	SDSS J143940−001810	17.73± 0.08	16.78± 0.03	16.31± 0.03	16.09± 0.03	15.61± 0.07	0.56	−85	11.1	23.5	2.0	23.8
119	SDSS J144056−001905	13.92± 0.01	12.35± 0.00	11.41± 0.00	10.96± 0.00	10.60± 0.01	0.49	−69	23.2	20.2	3.5	120.6
120	SDSS J144103+003709	17.12± 0.06	16.33± 0.03	15.83± 0.03	15.56± 0.03	15.33± 0.05	0.72	−63	13.0	23.4	2.0	29.2
121	SDSS J144148+004114	15.67± 0.03	14.67± 0.01	14.27± 0.01	14.10± 0.01	13.97± 0.02	0.60	53	15.8	22.3	2.0	42.0
122	SDSS J144245−002103	15.25± 0.02	14.38± 0.01	14.02± 0.01	13.86± 0.01	13.69± 0.03	0.37	25	8.9	20.8	2.4	32.7
123	SDSS J144300−002259	17.24± 0.06	16.13± 0.02	15.69± 0.02	15.47± 0.03	15.28± 0.06	0.68	−32	10.6	22.8	2.2	27.3
124	SDSS J144525+001404	17.55± 0.07	16.25± 0.03	15.67± 0.02	15.31± 0.02	15.03± 0.05	0.66	60	4.8	21.1	2.2	16.2
125	SDSS J144856−004337	17.96± 0.09	17.01± 0.04	15.92± 0.03	16.43± 0.04	16.05± 0.08	0.86	74	10.8	23.1	2.0	16.6
126	SDSS J144821−004827	17.41± 0.07	16.14± 0.03	15.51± 0.02	15.13± 0.02	14.80± 0.04	0.58	71	4.3	20.7	2.5	16.4
127	SDSS J144900−003852	17.94± 0.09	16.31± 0.03	15.40± 0.02	14.96± 0.02	14.60± 0.04	0.49	−1	2.4	19.3	5.2	20.5
128	SDSS J144916−004240	17.85± 0.08	16.58± 0.03	15.74± 0.02	15.33± 0.03	14.92± 0.04	0.69	11	3.0	20.1	3.8	17.4
129	SDSS J144909−005410	16.90± 0.05	15.86± 0.02	15.44± 0.02	15.22± 0.02	14.97± 0.05	0.75	−87	8.7	22.1	2.3	26.0

TABLE 3

MODEL-DEPENDENT PHOTOMETRIC PARAMETERS OF LARGE-ANGULAR-SIZE GALAXIES IDENTIFIED IN THE TEST FIELDS.

SDSS name (1)	$\mu_0^d(g^*)$ mag/$\square''$ (2)	$\alpha^d(g^*)$ ″ (3)	$\mu_0^b(g^*)$ mag/$\square''$ (4)	$\alpha^b(g^*)$ ″ (5)	$\mu_0^d(r^*)$ mag/$\square''$ (6)	$\alpha^d(r^*)$ ″ (7)	$\mu_0^b(r^*)$ mag/$\square''$ (8)	$\alpha^b(r^*)$ ″ (9)	$\mu_0^d(i^*)$ mag/$\square''$ (10)	$\alpha^d(i^*)$ ″ (11)	$\mu_0^b(i^*)$ mag/$\square''$ (12)	$\alpha^b(i^*)$ ″ (13)
J095146+001950	21.34±0.13	3.43±0.15	19.61±0.14	0.91±0.09	20.78±0.12	3.56±0.15	18.52±0.09	0.95±0.06	20.24±0.13	3.36±0.15	17.98±0.10	0.90±0.06
J095138+002211	23.28±0.06	7.64±0.22	23.47±0.75	1.07±0.53	23.21±0.08	8.54±0.30	23.02±0.26	1.96±0.46	23.06±0.13	8.84±0.51	22.50±0.28	1.95±0.48
J095938+003047	20.42±0.08	2.44±0.05			19.73±0.07	2.20±0.04			19.29±0.10	2.13±0.06		
J095939+003227	23.24±0.37	8.39±0.78	20.35±0.03	1.99±0.09	22.68±0.39	8.07±0.78	19.48±0.02	1.87±0.07	21.82±0.27	7.47±0.47	18.98±0.02	1.67±0.07
J095939+003511	22.36±0.29	5.22±0.36			21.75±0.27	5.18±0.34			21.05±0.15	5.79±0.22		
J095959+003816	22.06±0.23	3.51±0.21			21.68±0.25	3.87±0.28			21.47±0.34	3.80±0.37		
J095930−003745	21.11±0.05	2.64±0.05			20.41±0.06	2.48±0.06			19.99±0.07	2.44±0.06		
J100439+001653	22.26±0.15	5.05±0.29	19.78±0.13	1.13±0.09	20.64±0.07	3.29±0.09	18.68±0.10	0.75±0.04	21.14±0.15	5.28±0.31	18.56±0.15	1.07±0.10
J100440+001942	21.96±0.08	3.17±0.09			21.41±0.10	3.26±0.11	20.77±0.29	0.56±0.15	21.05±0.15	3.19±0.16	20.27±0.27	0.65±0.17
J100440+002211	22.38±0.19	5.90±0.41	19.17±0.10	1.23±0.08	21.47±0.20	5.65±0.43	18.22±0.11	1.15±0.08	21.04±0.17	5.54±0.35	17.84±0.10	1.15±0.07
J101114+002646	22.08±0.28	3.59±0.31	21.26±0.19	1.20±0.28	21.51±0.16	4.35±0.27	20.10±0.08	1.23±0.12	20.79±0.16	3.85±0.20	19.83±0.13	1.14±0.16
J101117+002632	21.00±0.04	8.33±0.01	19.99±0.49	0.83±0.23	20.39±0.01	8.73±0.16	19.31±0.29	0.86±0.13	20.28±0.01	9.85±0.20	19.24±0.19	1.47±0.15
J101142+003520	20.99±0.06	2.59±0.06			20.23±0.06	2.27±0.05			19.93±0.10	2.34±0.09		
J103135−005624	21.73±0.03	5.43±0.09			21.08±0.04	4.97±0.10			20.70±0.04	4.67±0.09		
J103339−003939	22.47±0.06	5.16±0.16			21.92±0.05	4.78±0.12			21.59±0.04	4.68±0.10		
J103825−000104	22.50±0.13	5.74±0.35	21.70±0.19	1.50±0.25	22.11±0.12	5.94±0.34	21.07±0.15	1.52±0.20	21.85±0.15	5.93±0.42	20.77±0.18	1.46±0.22
J104406−005744	22.24±0.06	5.50±0.26			21.84±0.05	5.61±0.19			21.54±0.04	5.07±0.13		
J104509+000433	22.23±0.11	5.30±0.21	20.33±0.11	1.12±0.10	21.52±0.10	5.31±0.21	19.06±0.08	1.03±0.06	21.18±0.14	4.92±0.35	18.47±0.09	0.98±0.06
J104504+000617	21.08±0.05	7.10±0.23	19.17±0.14	0.96±0.08	20.40±0.05	6.53±0.19	18.14±0.08	0.98±0.05	20.17±0.05	7.05±0.19	17.65±0.09	1.03±0.05
J104614+000300	20.37±0.15	3.49±0.16	19.54±0.16	1.16±0.18	20.50±0.14	3.91±0.19	18.89±0.11	1.15±0.10	20.40±0.15	4.08±0.21	18.58±0.10	1.19±0.09
J104819−000119	21.17±0.06	3.60±0.11	21.27±0.47	0.64±0.24	20.68±0.19	3.80±0.22	20.55±0.36	0.94±0.42	21.15±0.59	5.63±0.75	19.93±0.14	1.59±0.46
J110548−000209	21.64±0.03	75.31±0.50			21.13±0.03	77.55±0.56			20.69±0.03	74.91±0.60		
J110546−000813	21.26±0.05	3.99±0.07			20.59±0.04	3.62±0.07			20.34±0.05	3.60±0.08		
J110535−000946	20.49±0.03	3.50±0.05			19.76±0.02	3.37±0.03			19.39±0.02	3.39±0.04		
J110646+001524	22.11±0.17	4.17±0.19	18.47±0.05	1.01±0.03	20.97±0.10	3.82±0.13	17.36±0.04	0.90±0.02	20.69±0.13	4.12±0.17	16.95±0.04	0.91±0.02
J110655−001845	21.80±0.03	4.70±0.07			21.25±0.04	3.99±0.07			21.12±0.05	4.39±0.10		
J110708+002152	23.12±0.07	3.91±0.14			22.69±0.07	3.55±0.13			22.45±0.19	7.41±0.54		
J110840+001602	20.40±0.05	4.72±0.06	18.82±0.36	0.36±0.09	19.64±0.06	4.61±0.07	18.17±0.28	0.41±0.09	19.31±0.07	4.81±0.07	18.01±0.17	0.52±0.09
J110839+001703	21.14±0.09	3.73±0.10	18.50±0.05	1.03±0.03	20.20±0.08	3.58±0.09	17.52±0.05	0.94±0.03	19.90±0.10	3.72±0.12	17.12±0.06	0.96±0.04
J110841+002331	21.13±0.10	4.61±0.12			20.76±0.22	4.65±0.23			20.56±0.17	4.84±0.19		
J111050+011232	22.60±0.07	5.69±0.13			21.18±0.06	4.90±0.14			21.12±0.04	5.09±0.09		
J111104+010525	21.45±0.10	3.05±0.08	20.54±0.28	0.47±0.13	20.67±0.16	2.97±0.12	19.40±0.17	0.57±0.12	20.24±0.14	2.86±0.10	19.04±0.13	0.60±0.11
J111117+010914	22.96±0.15	4.64±0.22	20.36±0.09	1.17±0.07	21.76±0.13	3.88±0.16	19.25±0.07	0.98±0.05	21.32±0.13	3.69±0.14	18.80±0.07	1.00±0.05
J111612+005935	21.73±0.07	2.62±0.08			20.85±0.09	2.38±0.12			20.49±0.08	2.59±0.09		
J111849+003709	19.63±0.10	2.95±0.08			18.95±0.02	3.03±0.03			18.60±0.02	2.90±0.02		
J111916+003241	21.48±0.12	3.46±0.14	21.13±0.14	1.10±0.19	20.50±0.07	3.22±0.07	19.94±0.09	0.90±0.09	20.27±0.08	3.51±0.09	19.29±0.07	1.01±0.08
J112418+003837	20.57±0.07	4.70±0.12	19.07±0.07	1.04±0.07	20.30±0.06	4.97±0.09	18.64±0.04	1.18±0.05	20.43±0.11	6.78±0.20	18.41±0.06	1.30±0.08
J112409+004201	20.91±0.12	5.64±0.14	20.73±0.17	1.16±0.34	20.31±0.08	5.26±0.09	19.81±0.08	1.17±0.15	20.03±0.13	5.32±0.14	19.38±0.11	1.20±0.22
J112712−005940	21.71±0.03	10.45±0.13			21.43±0.03	10.95±0.14			21.11±0.03	10.75±0.16		
J112829+000838	22.09±0.07	2.94±0.16			21.47±0.05	3.26±0.10			21.12±0.04	3.22±0.09		
J113158−000301	21.79±0.08	5.92±0.12	21.58±0.76	0.45±0.31	21.11±0.04	5.87±0.08	20.09±0.64	0.34±0.14	20.76±0.04	5.60±0.11	20.36±0.41	0.53±0.18
J113256−004024	22.77±0.24	3.36±0.26	21.76±0.16	1.03±0.20	21.57±0.15	3.36±0.17	20.32±0.12	0.93±0.12	21.05±0.13	3.35±0.14	19.83±0.13	0.91±0.11
J113245−004428	22.16±0.36	6.39±0.60			21.66±0.34	5.83±0.49			21.44±0.44	6.28±0.71		
J113457−004514	22.02±0.02	5.69±0.06			21.56±0.02	5.12±0.07			21.31±0.04	5.03±0.11		
J120148−010802	23.47±0.34	5.35±0.73	20.76±0.05	1.50±0.09	22.44±0.14	5.41±0.33	19.51±0.03	1.30±0.04	22.34±0.16	6.38±0.50	19.18±0.03	1.42±0.04
J120140−011213	24.27±0.08	8.87±0.30			23.83±0.10	8.76±0.40			23.61±0.11	8.73±0.50		
J120804+004153	21.02±0.10	3.47±0.08			20.69±0.16	3.54±0.14			20.54±0.13	3.89±0.12		
J121243+005854	24.22±0.06	6.43±0.27			23.64±0.07	5.68±0.27			23.19±0.08	5.23±0.25		
J121203−003621	21.54±0.38	4.55±0.55	19.62±0.24	1.08±0.25	21.07±0.16	4.23±0.21	20.05±0.19	1.06±0.21	20.82±0.19	4.22±0.25	20.15±0.30	1.07±0.35
J121500−005506	22.31±0.11	3.37±0.12	20.41±0.10	0.84±0.07	21.69±0.12	3.75±0.15	19.23±0.09	0.84±0.05	21.01±0.13	3.12±0.14	18.87±0.08	0.82±0.05
J121526−005622	24.08±0.48	6.20±1.14	20.73±0.40	0.63±0.16	23.38±0.17	7.34±0.55	19.66±0.15	0.57±0.05	23.30±0.19	5.65±0.31	19.47±0.09	0.67±0.04
J121502−010212	22.64±0.17	4.50±0.25	22.11±0.41	1.05±0.38	22.09±0.13	4.36±0.28	21.17±0.35	0.85±0.21	21.70±0.12	3.87±0.19	20.96±0.41	0.83±0.23
J121604+011049	19.72±0.02	2.58±0.04			18.99±0.04	2.45±0.06			18.63±0.03	2.51±0.06		
J121925+001244	22.53±0.04	6.06±0.11			22.30±0.04	6.29±0.13			22.15±0.08	6.45±0.24		
J122034+004714	22.31±0.05	10.56±0.15			21.86±0.05	10.82±0.17			21.69±0.11	11.14±0.25		
J122342−001526	23.63±0.04	6.58±0.13			23.16±0.07	6.62±0.23			23.31±0.08	8.95±0.50		
J122427+000910	21.32±0.15	6.80±0.26	19.91±0.12	1.29±0.19	20.55±0.12	6.49±0.21	18.99±0.09	1.28±0.13	20.25±0.15	7.06±0.23	18.52±0.10	1.28±0.15
J122404+011123	20.81±0.11	4.95±0.14	18.73±0.10	0.86±0.07	20.31±0.11	5.18±0.14	18.57±0.08	1.01±0.08	20.16±0.11	5.48±0.16	18.57±0.07	1.21±0.09
J122411+011247	21.48±0.31	5.75±0.40			20.81±0.44	5.38±0.50			20.45±0.32	5.67±0.41		
J122619+010112	21.64±0.03	4.39±0.07			21.44±0.03	4.72±0.07			21.21±0.03	4.64±0.09		
J122654−005239	20.67±0.03	9.55±0.09	18.52±0.03	2.23±0.04	20.00±0.03	9.57±0.09	17.56±0.03	2.03±0.04	19.71±0.03	10.04±0.11	17.03±0.03	1.93±0.04
J122610−010923	23.17±0.34	5.00±0.53			21.62±0.25	3.32±0.18			21.40±0.11	3.69±0.09		
J122704−005421	20.77±0.03	6.45±0.09			20.58±0.02	6.85±0.08			20.52±0.02	7.30±0.08		
J122903+000614	22.92±0.06	9.34±0.20			22.45±0.07	9.85±0.25			22.35±0.07	10.77±0.30		
J122902+001159	22.68±0.40	3.25±0.38	20.26±0.11	1.09±0.11	21.88±0.30	3.39±0.32	19.09±0.09	1.03±0.07	21.93±0.20	4.61±0.35	18.60±0.08	1.06±0.05
J122912+004903	22.47±0.08	7.77±0.26	19.19±0.18	0.71±0.07	21.75±0.08	7.15±0.28	18.47±0.13	0.76±0.05	21.39±0.07	7.05±0.19	18.05±0.11	0.78±0.04
J122921+010324	20.88±0.08	5.63±0.19	19.38±0.20	0.84±0.12	20.39±0.08	5.74±0.15	19.01±0.13	1.03±0.12	20.14±0.11	5.73±0.17	18.86±0.13	1.14±0.15
J122932+010608	22.00±0.25	3.63±0.29	18.68±0.10	0.96±0.06	21.13±0.25	3.72±0.31	17.78±0.11	0.96±0.06	20.89±0.27	3.88±0.35	17.45±0.11	0.99±0.06
J123141+005733	22.23±0.35	2.95±0.28	20.67±0.12	1.09±0.15	22.46±0.27	4.05±0.36	19.88±0.04	1.31±0.06	22.54±0.21	5.39±0.48	19.52±0.04	1.38±0.05
J123309−002231	23.73±0.07	6.11±0.18			23.14±0.07	6.35±0.21			22.82±0.07	6.35±0.20		
J125405−000604	23.53±0.12	11.56±0.50	22.17±0.07	3.36±0.25	22.80±0.12	11.10±0.48	21.95±0.08	3.52±0.35	22.45±0.12	10.85±0.44	21.75±0.01	3.38±0.34
J125700+010142	23.05±0.08	14.35±0.51	22.23±0.18	2.45±0.36	22.48±0.09	12.58±0.42	21.82±0.17	2.46±0.35	22.33±0.09	13.11±0.47	21.48±0.17	2.46±0.34
J130058−000139	20.14±0.02	13.39±0.11	19.58±0.11	2.12±0.20	19.64±0.02	13.96±0.09	19.22±0.09	2.53±0.21	19.31±0.02	13.30±0.09	19.08±0.09	2.57±0.23
J130243+003949	21.38±0.13	5.04±0.23	19.75±0.16	0.98±0.13	20.81±0.10	5.81±0.16	19.13±0.09	1.11±0.10	20.40±0.14	5.36±0.25	18.68±0.12	1.10±0.13
J130931+005125	20.92±0.06	11.75±0.26	17.79±0.07	1.37±0.06	19.56±0.08	10.07±0.18	16.77±0.03	1.11±0.04	19.09±0.13	10.81±0.25	16.28±0.07	1.06±0.07
J131004+005655	22.60±0.03	6.02±0.10			21.97±0.04	5.25±0.13			21.90±0.03	6.47±0.14		
J131201+003532	22.56±0.02	5.29±0.08			22.11±0.04	5.07±0.13			22.22±0.05	6.66±0.16		
J131215+003554	22.20±0.40	4.92±0.45	20.54±0.09	1.44±0.22	21.64±0.18	4.92±0.20	19.88±0.05	1.26±0.10	21.20±0.22	4.76±0.24	19.53±0.08	1.18±0.14
J131244−000223	22.24±0.07	5.13±0.17			21.85±0.29	5.57±0.53	21.73±0.83	0.96±0.90	21.94±0.25	7.21±0.68	21.26±0.17	1.46±0.40
J131305−003540	22.39±0.14	6.65±0.30	22.01±0.32	1.19±0.42	21.79±0.17	5.80±0.29	21.23±0.35	1.13±0.42	21.41±0.21	5.12±0.30	21.06±0.48	1.10±0.57
J131809+001322	21.62±0.08	5.76±0.24	21.11±0.25	1.01±0.24	21.28±0.06	5.72±0.15	20.65±0.10	1.37±0.14	21.08±0.07	5.69±0.16	20.40±0.10	1.43±0.15

Table 3—*Continued*

SDSS name (1)	$\mu_0^d(g^*)$ mag/$\Box''$ (2)	$\alpha^d(g^*)$ $''$ (3)	$\mu_0^b(g^*)$ mag/$\Box''$ (4)	$\alpha^b(g^*)$ $''$ (5)	$\mu_0^d(r^*)$ mag/$\Box''$ (6)	$\alpha^d(r^*)$ $''$ (7)	$\mu_0^b(r^*)$ mag/$\Box''$ (8)	$\alpha^b(r^*)$ $''$ (9)	$\mu_0^d(i^*)$ mag/$\Box''$ (10)	$\alpha^d(i^*)$ $''$ (11)	$\mu_0^b(i^*)$ mag/$\Box''$ (12)	$\alpha^b(i^*)$ $''$ (13)
J131821+002055	21.34±0.04	3.77±0.07			20.72±0.14	3.23±0.14			20.77±0.09	4.09±0.12	19.93±0.11	1.26±0.12
J131821+002440	23.55±0.10	5.66±0.25	21.07±0.08	1.09±0.06	23.23±0.10	5.92±0.28	19.94±0.05	1.02±0.04	22.96±0.13	6.65±0.43	19.47±0.07	1.01±0.04
J132345+010231	22.64±0.34	5.32±0.43	20.49±0.27	0.88±0.21	21.95±0.78	4.75±1.12	19.29±0.31	0.91±0.26	21.91±0.96	5.50±1.21	18.92±0.19	1.06±0.23
J132926+005412	23.03±0.04	12.48±0.33			22.52±0.04	11.67±0.29			22.32±0.03	12.03±0.24		
J133305−010208	21.39±0.28	12.71±1.65	17.28±0.07	1.58±0.07	20.55±0.01	12.24±0.84	16.25±0.05	1.50±0.03	20.39±0.01	12.88±0.93	15.85±0.05	1.56±0.04
J133435−002109	20.50±0.04	3.80±0.05			20.02±0.03	3.74±0.03			19.89±0.02	3.85±0.03		
J135244+000748	21.36±0.14	4.02±0.13			20.94±0.14	3.83±0.13			19.57±0.07	3.23±0.05		
J135230+002504	22.37±0.14	5.44±0.20	20.16±0.06	1.17±0.07	21.43±0.21	4.14±0.21	19.08±0.07	1.11±0.08	21.31±0.10	5.15±0.21	18.59±0.08	1.11±0.05
J135214+003540	22.38±0.32	4.43±0.45	18.35±0.10	0.92±0.05	21.22±0.30	3.72±0.36	17.40±0.10	0.87±0.05	21.23±0.27	5.12±0.45	17.01±0.09	0.91±0.05
J135943−003133	23.26±0.03	5.99±0.13			22.87±0.07	5.83±0.22			22.73±0.09	6.90±0.34		
J135943−003424	23.10±0.14	3.90±0.20	18.72±0.10	0.57±0.03	21.98±0.08	3.60±0.10	18.58±0.07	0.62±0.02	21.92±0.11	4.69±0.21	18.21±0.09	0.68±0.03
J140042−003020	21.04±0.04	4.86±0.09			20.61±0.03	4.68±0.13			20.42±0.02	4.70±0.07		
J140327+004359	21.39±0.51	4.78±0.51	20.34±0.22	0.88±0.44	20.49±0.25	5.38±0.44	19.42±0.42	0.73±0.34	20.46±0.25	5.20±0.29	18.98±0.06	1.01±0.14
J140344+004849	20.08±0.01	3.94±0.03			20.06±0.30	4.57±0.26	19.74±0.14	1.66±0.49	19.53±0.16	4.18±0.14	19.29±0.14	1.32±0.32
J140320−003259	19.82±0.26	4.10±0.21	18.54±0.17	1.02±0.23	19.43±0.40	4.17±0.32	17.97±0.12	1.19±0.26	19.76±0.30	5.09±0.35	17.67±0.07	1.49±0.12
J140403+005347	20.40±0.04	3.11±0.06			19.81±0.06	3.09±0.08			19.55±0.05	3.19±0.04		
J140405+005953	22.06±0.14	5.38±0.18	20.74±0.13	1.30±0.17	21.77±0.18	4.98±0.26	20.37±0.17	1.22±0.21	21.95±0.13	6.56±0.23	20.23±0.10	1.36±0.14
J143327−000708	22.86±0.27	8.85±0.79	21.04±0.17	1.76±0.32	22.57±0.37	8.84±1.03	20.70±0.14	1.96±0.36	22.38±0.42	9.24±1.27	20.41±0.17	1.90±0.40
J143638+000702	22.08±0.07	4.39±0.15			21.52±0.08	4.29±0.16			21.52±0.09	4.96±0.18	21.01±0.41	1.00±0.28
J143907+003030	21.48±0.05	5.03±0.16	22.00±1.05	0.69±0.46	21.24±0.10	5.29±0.24	20.92±0.25	1.30±0.29	21.24±0.15	5.74±0.29	20.60±0.14	1.81±0.31
J144056−001905	21.44±0.02	22.76±0.20	18.75±0.03	3.88±0.07	20.48±0.02	21.42±0.19	17.54±0.03	3.64±0.06	19.95±0.02	20.77±0.19	16.93±0.03	3.60±0.05
J144103+003709	22.82±0.04	7.43±0.14	21.95±0.24	0.70±0.14	22.46±0.05	8.44±0.23	21.80±0.34	0.75±0.22	22.16±0.04	8.19±0.19	21.85±4.47	0.31±0.78
J144245−002103	20.09±0.02	5.54±0.05			19.74±0.02	5.54±0.06			19.61±0.02	5.63±0.05		
J144525+001404	20.83±0.04	3.22±0.09			20.04±0.05	2.93±0.11			19.70±0.04	3.08±0.08		
J144856−004337	22.60±0.11	4.52±0.12	22.17±0.13	1.04±0.20	22.12±0.18	4.50±0.22	21.60±0.21	1.02±0.32	21.85±0.24	4.40±0.27	21.31±0.26	1.04±0.41
J144821−004827	20.45±0.08	3.15±0.08			19.60±0.04	2.88±0.05			19.15±0.04	2.77±0.05		
J144900−003852	22.44±0.16	4.36±0.21	18.99±0.07	1.04±0.04	21.71±0.18	4.65±0.31	18.07±0.07	1.04±0.04	21.15±0.12	4.58±0.18	17.62±0.06	1.01±0.04
J144916−004240	22.28±0.13	4.01±0.17	19.65±0.04	1.15±0.04	21.36±0.14	3.98±0.20	18.74±0.05	1.06±0.04	20.38±0.07	3.12±0.06	18.25±0.03	0.94±0.03
J144909−005410	21.75±0.08	6.04±0.18	21.71±0.52	0.90±0.42	21.33±0.06	6.00±0.13	21.06±0.19	1.17±0.21	20.97±0.07	5.58±0.15	20.94±0.28	1.14±0.33

Table 4

Model-dependent photometric parameters of large-angular-size galaxies with Sérsic profiles identified in the test fields.

SDSS name (1)	$\mu_0(g^*)$ **mag/□″** **(2)**	$\alpha(g^*)$ ″ **(3)**	$n(g^*)$ **(4)**	$\mu_0(r^*)$ **mag/□″** **(5)**	$\alpha(r^*)$ ″ **(6)**	$n(r^*)$ **(7)**	$\mu_0(i^*)$ **mag/□″** **(8)**	$\alpha(i^*)$ ″ **(9)**	$n(i^*)$ **(10)**
J103806−000319	**23.86±0.10**	**8.15±0.69**	**1.55±0.13**	**23.48±0.06**	**7.96±0.40**	**1.54±0.08**	**23.16±0.10**	**8.11±0.70**	**1.60±0.15**
J110440+000329	**23.68±0.06**	**11.19±0.53**	**1.38±0.07**	**23.27±0.06**	**12.25±0.53**	**1.50±0.08**	**22.89±0.07**	**12.06±0.70**	**1.23±0.07**
J111055+010537	**22.07±0.05**	**8.77±0.42**	**1.17±0.04**	**21.86±0.05**	**9.22±0.41**	**1.19±0.04**	**21.71±0.08**	**8.99±0.68**	**1.14±0.06**
J111247−003406	**23.93±0.07**	**11.64±0.54**	**1.74±0.11**	**23.52±0.10**	**10.12±0.70**	**1.63±0.17**	**23.21±0.16**	**9.51±1.12**	**1.51±0.22**
J121257+011348	**24.65±0.09**	**9.63±0.66**	**1.43±0.11**	**23.98±0.11**	**8.43±0.81**	**1.24±0.11**	**23.68±0.13**	**9.90±1.18**	**1.20±0.15**
J122430+000416	**23.73±0.06**	**12.35±0.51**	**1.78±0.11**	**23.44±0.08**	**12.47±0.65**	**1.72±0.13**	**23.24±0.07**	**11.97±0.65**	**1.55±0.11**
J122622−011520	**23.13±0.12**	**12.39±0.78**	**1.62±0.12**	**22.92±0.10**	**11.97±0.61**	**1.62±0.09**	**23.16±0.13**	**14.10±0.88**	**1.92±0.18**
J123116+005939	**24.24±0.08**	**10.72±0.61**	**1.51±0.11**	**24.02±0.09**	**11.23±0.68**	**1.76±0.16**	**23.72±0.08**	**16.43±0.83**	**1.70±0.19**
J123307−003159	**24.08±0.05**	**20.39±0.75**	**1.40±0.05**	**23.63±0.06**	**20.04±0.89**	**1.39±0.06**	**23.47±0.08**	**20.57±1.28**	**1.35±0.09**
J125004−001356	**24.59±0.06**	**14.60±0.53**	**2.21±0.16**	**24.08±0.08**	**14.22±0.76**	**1.83±0.17**	**23.90±0.10**	**15.02±0.93**	**2.02±0.25**
J143960−001110	**23.50±0.04**	**6.50±0.19**	**1.46±0.04**	**22.89±0.07**	**5.37±0.37**	**1.11±0.06**	**22.71±0.20**	**5.27±0.97**	**1.11±0.16**
J143940−001810	**23.34±0.04**	**10.82±0.28**	**1.47±0.04**	**23.03±0.04**	**11.69±0.31**	**1.59±0.05**	**22.81±0.05**	**11.49±0.38**	**1.48±0.05**
J144148+004114	**22.22±0.02**	**16.01±0.40**	**1.50±0.04**	**21.49±0.03**	**12.45±0.41**	**1.21±0.03**	**21.26±0.03**	**12.34±0.41**	**1.20±0.03**
J144300−002259	**22.58±0.07**	**9.27±0.53**	**1.24±0.05**	**22.00±0.05**	**8.21±0.30**	**1.13±0.03**	**21.77±0.06**	**8.16±0.42**	**1.14±0.04**

Table 5

The Photometric Repeatability.

SDSS Name (1)	u^* (2)	g^* (3)	r^* (4)	i^* (5)	z^* (6)
SDSS J113457−004514	16.97±0.06	16.21±0.03	15.90±0.03	15.73±0.03	15.39±0.06
SDSS J113457−004514	17.16±0.06	16.34±0.03	15.99±0.03	15.74±0.03	15.46±0.06
SDSS J135230+002504	17.82±0.08	16.68±0.03	15.95±0.03	15.46±0.02	15.04±0.04
SDSS J135230+002504	17.63±0.08	16.57±0.03	15.99±0.03	15.57±0.03	15.28±0.05
SDSS J144856−004337	17.96±0.08	17.01±0.04	15.92±0.03	16.43±0.04	16.05±0.08
SDSS J144856−004337	17.89±0.08	16.91±0.04	15.94±0.03	16.40±0.05	15.85±0.07

Table 6

Giant LSB spiral galaxies from our sample.

SDSS Name (1)	Impey Name (2)	$M_{disk}(B)$ mag (3)	$\mu_{0,\mathrm{c}}(B)$ mag arcsec^2 (4)	α kpc (5)	Diff.index (6)
SDSS J095939+003227		−18.41	24.46	7.26	28.76
SDSS J104509+000433	1042+0020	−20.46	22.95	9.32	27.80
SDSS J111117+010914		−18.46	24.48	7.52	28.86
SDSS J120148−010802		−19.87	24.10	12.07	29.51
SDSS J121526−005622	1212−0039	−18.67	24.66	9.00	29.43
SDSS J122912+004903	1226+0105	−21.00	22.94	11.88	28.31
SDSS J131821+002440		−18.51	24.69	8.44	29.32
SDSS J132345+010231	1321+0118	−20.54	23.22	10.94	28.41
SDSS J135230+002504	1349+0039	−20.87	22.75	10.25	27.80
SDSS J135943−003424		−20.44	23.59	12.37	29.05
SDSS J140831−000737	1405+0006	−18.18	24.59	6.94	28.80